

# REPORT DOCUMENTATION PAGE

Form Approved  
OMB NO. 0704-0188

Public Reporting burden for this collection of information is estimated to average 1 hour per response, including the time for reviewing instructions, searching existing data sources, gathering and maintaining the data needed, and completing and reviewing the collection of information. Send comment regarding this burden estimates or any other aspect of this collection of information, including suggestions for reducing this burden, to Washington Headquarters Services, Directorate for Information Operations and Reports, 1215 Jefferson Davis Highway, Suite 1204, Arlington, VA 22202-4302, and to the Office of Management and Budget, Paperwork Reduction Project (0704-0188), Washington, DC 20503.

1. REPORT DATE May 19, 2001	2. REPORT TYPE Final Progress Report	3. DATES COVERED (5/1/1997 - 12/31/2000)		
4. TITLE AND SUBTITLE Strained and Unstrained $Bi_{1-x}Sb_x$ Superlattice Thermoelectrics		5a. CONTRACT NUMBERS 5b. GRANT NUMBERS DAAG55-97-1-0130 5c. PROGRAM ELEMENT NUMBERS		
6. AUTHOR(S) Ketterson, John, B., Freeman, Arthur, J., Meyer, Jerry, R., Wong, George, K., and DiVenere, Antonio		5d. PROJECT NUMBERS 5e. TASK NUMBERS 5f. WORK UNIT NUMBERS		
7. PERFORMING ORGANIZATION NAME(S) AND ADDRESS(ES) Northwestern University, Department of Physics and Astronomy, 2145 Sheridan Rd., Evanston, IL 60201; Naval Research Laboratory, Code 5613, Washington, DC 20375-5338		8. PERFORMING ORGANIZATION REPORT NUMBER		
9. SPONSORING / MONITORING AGENCY NAME(S) AND ADDRESS(ES) U. S. Army Research Office P.O. Box 12211 Research Triangle Park, NC 27709-2211		10. SPONSOR / MONITOR'S ACRONYM(S) 11. SPONSORING / MONITORING AGENCY REPORT NUMBER 37310-MS .33		
12. DISTRIBUTION/AVAILABILITY STATEMENT Approved for public release; distribution unlimited.				
13. SUPPLEMENTARY NOTES The views, opinions and/or findings contained in this report are those of the author(s) and should not be construed as an official Department of the Army position, policy or decision, unless so designated by the documentation.				
14. ABSTRACT The electronic band structure of artificially ordered superlattice alloys (SLA) of Bi and Sb, prepared by alternately depositing thin layers of Bi and Sb as a superlattice, could be modified from a semimetal to a semiconductor by changing the period of the superlattice. This new SLA opens a possibility to engineer an alloy material to get more desirable thermoelectric properties, because a thermal conductivity reduction, due to an increase in phonon scattering from the superlattice interfaces, is expected; certain electronic properties are altered at the same time. To check the performance of an in-plane Bi/BiSb cooling device, anisotropy in the films was investigated. Bi showed a strongly anisotropic and field-direction-dependent magneto-Seebeck effect. The magneto-transport properties of $Bi_{1-x}Sb_x$ films and Bi/CdTe superlattices have been determined by applying the Quantitative Mobility Spectrum Analysis and multicarrier fitting to the magnetic-field-dependent resistivities and Hall coefficients, using algorithms which account for the strong anisotropy of the mobilities. Using the local density relativistic full-potential linear muffin-tin orbital method, we found that the internal displacement changes the Bi electronic structure from a metal to a semimetal and that an increase of the trigonal shear angle can lead to a semimetal-semiconductor transition in Bi. Post annealing of Bi films near its melting point improved the magnetoresistance ratios drastically, which can be ascribed to the electron mobility enhancement. The calculation of the electronic structure of $Bi_2Te_3$ suggested that the quasi-two dimensional crystal structure of $Bi_2Te_3$ gives a large, but finite, anisotropy in the effective mass which enhances the thermoelectric figure of merit.				
15. SUBJECT TERMS Bi and BiSb alloy films, thermoelectrics, superlattice alloy, anisotropy				
16. SECURITY CLASSIFICATION OF: a. REPORT UNCLASSIFIED		17. LIMITATION OF ABSTRACT UL	18. NUMBER OF PAGES 10	19a. NAME OF RESPONSIBLE PERSON J. B. Ketterson
b. ABSTRACT UNCLASSIFIED		19b. TELEPHONE NUMBER 847-491-5468		
c. THIS PAGE UNCLASSIFIED				

NSN 7540-01-280-5500

Standard Form 298 (Rev. 8-98)  
Prescribed by ANSI Std. Z39-18

20010608 077

---

**REPORT DOCUMENTATION PAGE (SF298)**  
**(Continuation Sheet)**

---

**List of Publications**

**I. Journal Articles Submitted or Published**

1. "Growth mode modification of Bi on CdTe(111)A using Te monolayer deposition", S. Cho, A. DiVenere, G. K. Wong, J. B. Ketterson, J. R. Meyer and J. I. Hong, Phys. Rev. B **54**, 2324(1998).
2. "Molecular beam epitaxial growth and structural properties of BiSb alloy thin films on CdTe(111) substrates", S. Cho, A. DiVenere, G. K. Wong, J. B. Ketterson, J. R. Meyer, and C. A. Hoffman, J. Vac. Sci. Technol. A **17**, 9 (1999).
3. "Thermoelectric transport properties of n-doped and p-doped  $\text{Bi}_{0.91}\text{Sb}_{0.09}$  alloy thin films", S. Cho, A. DiVenere, G. K. Wong, J. B. Ketterson, and J. R. Meyer, J. Appl. Phys. **85**, 3655 (1999).
4. "Transport properties of Bi and  $\text{Bi}_{1-x}\text{Sb}_x$  alloy thin films grown on CdTe(111)B", S. Cho, A. DiVenere, G. K. Wong, J. B. Ketterson, and J. R. Meyer, Phys. Rev. B **59**, 10691 (1999).
5. "Quantitative mobility spectrum analysis (QMSA) for Hall characterization of electrons and holes in anisotropic bands", I. Vurgaftman, J. R. Meyer, C. A. Hoffman, S. Cho, J. B. Ketterson, L. Faraone, J. Antoszewski, and J. R. Lindemuth, J. Electron. Mater. **28**, 548-552 (1999).
6. "Thermoelectric and magnetotransport properties of  $\text{Bi}_{1-x}\text{Sb}_x$  thin films and Bi/CdTe superlattices", I. Vurgaftman, J. R. Meyer, C. A. Hoffman, S. Cho, A. DiVenere, G. K. Wong, J. B. Ketterson, J. Phys. - Condens. Mat. **11**, 5157-5167 (1999).
7. "Antisite defects of  $\text{Bi}_2\text{Te}_3$  thin films", S. Cho, Y. Kim, A. DiVenere, G. K. Wong, and J. B. Ketterson, Appl. Phys. Lett. **75**, 1401-1403 (1999).
8. "Bi/Sb superlattices grown by molecular beam epitaxy", S. Cho, Y. Kim, A. DiVenere, G. K. Wong, J. B. Ketterson, J.-I. Hong, J. Vac. Sci. Technol. A **17**, 2987 (1999).
9. "Growth habit of rhombohedral Bi thin films on zinc-blende CdTe substrates with various orientations", Y. Kim, S. Cho, A. DiVenere, G. K. Wong, and J. B. Ketterson, J. Vac. Sci. Technol. A **17**, 3473 (1999).
10. "Electronic structure, phase stability, and semimetal-semiconductor transitions in Bi", A. B. Shick, J. B. Ketterson, D. L. Novikov, and A. J. Freeman, Phys. Rev. B **60**, 15484 (1999).
11. "Anisotropic Seebeck and magneto-Seebeck coefficients in Bi and BiSb alloy thin films", S. Cho, Y. Kim, A. DiVenere, G. K. L. Wong, J. B. Ketterson, and J. R. Meyer, J. Appl. Phys. **88**, 808 (2000).
12. "Composition-dependent layered structure and transport properties in BiTe thin films", Y. Kim, S. Cho, A. DiVenere, G. K. L. Wong, and J. B. Ketterson, Phys. Rev. B. **63**, 155306 (2001).
13. "First-principles electronic structure and its relation to thermoelectric properties of  $\text{Bi}_2\text{Te}_3$ ", S. J. Youn, and A. J. Freeman, Phys. Rev. B. **63**, 085112 (2001).

---

**REPORT DOCUMENTATION PAGE (SF298)**  
**(Continuation Sheet)**

---

14. "Large magnetoresistance in post-annealed Bi thin films", by S. Cho, Y. Kim, A. J. Freeman, G. K. Wong, J. B. Ketterson, L. J. Olafsen, I. Vurgaftman, J. R. Meyer, and C. A. Hoffman, submitted to Applied Physics Letters. (4/4/2001)
15. "Bi epitaxy on polar InSb(111)A/B faces", by S. Cho, Y.-H. Um, Y. Kim, G. K. Wong, J. B. Ketterson, and J.-I. Hong, submitted to Journal of Vacuum Science & Technology A. (4/4/2001)
16. "Artificially ordered Bi/Sb superlattice alloys: fabrication and transport properties", by S. Cho, Y. Kim, S. J. Youn, A. DiVenere, G. K. Wong, A. J. Freeman, J. B. Ketterson, L. J. Olafsen, I. Vurgaftman, J. R. Meyer, and C. A. Hoffman, submitted to Physical Review B. (4/4/2001)
17. "Polarity inversion in polar/nonpolar/polar heterostructures", by S. Cho, S.-J. Youn, Y. Kim, A. DiVenere, G. K. L. Wong, A. J. Freeman, and J. B. Ketterson, submitted to Physical Review Letters. (4/4/2001)
18. "Structural and thermoelectric transport properties of  $Sb_2Te_3$  thin films grown by molecular beam epitaxy", by Y. Kim, A. DiVenere, G. K. L. Wong, J. B. Ketterson, S. Cho, J. R. Meyer, submitted to Journal of Applied Physics. (5/7/2001)

## **II. Conference Proceedings**

1. "Thermoelectric power of Bi and  $Bi_{1-x}Sb_x$  alloy thin films and superlattices grown by MBE", S. Cho, A. DiVenere, G. K. Wong, J. B. Ketterson, J. R. Meyer, and C. A. Hoffman, Mat. Res. Soc. Symp. Proc. **478**, 67 (1997).
2. "Observation of a power factor enhancement in MBE-grown  $Bi_{1-x}Sb_x$  alloy thin films", S. Cho, A. DiVenere, G. K. Wong, J. B. Ketterson, J. R. Meyer, and C. A. Hoffman, Proc. of Int. Conf. Thermoelectrics, Dresden, Germany, p188 (1997).
3. "Structural and thermoelectric properties of MBE-grown doped and undoped BiSb alloy thin films", S. Cho, A. DiVenere, G. K. Wong, J. B. Ketterson, J. R. Meyer, and C. A. Hoffman, Proc. of Int. Conf. Thermoelectrics, Nagoya, Japan, p284 (1998).
4. " $Bi_{1-x}Sb_x$  thin film and superlattice thermoelectrics", S. Cho, A. DiVenere, A. B. Shick, Y. Kim, S. J. Youn, A. J. Freeman, G. K. Wong, J. B. Ketterson, J. R. Meyer and C. A. Hoffman, MRS March Meeting, Boston, 1998. (Mat. Res. Soc. Symp. Proc. **545**, 283 (1999))
5. "MBE growth and thermoelectric properties of  $Bi_2Te_3$  thin films", S. Cho, A. DiVenere, G. K. Wong, J. B. Ketterson, and J. R. Meyer, MRS March Meeting, Boston, 1998. (Mat. Res. Soc. Symp. Proc. **545**, 183 (1999))
6. "Thermoelectric and structural properties of  $Bi_{1-x}Te_{1+x}$  thin films on CdTe(111)", Y. Kim, S. Cho, A. DiVenere, G. K. Wong, J. B. Ketterson, and J. R. Meyer, MRS March Meeting, Boston, 1998. (Mat. Res. Soc. Symp. Proc. **545**, 177 (1999))

---

**REPORT DOCUMENTATION PAGE (SF298)**  
**(Continuation Sheet)**

---

7. "Artificially Ordered BiSb Superlattice Alloy: Growth and Thermoelectric Properties", S. Cho, Y. Kim, A. DiVenere, G. K. Wong, J. B. Ketterson, J. R. Meyer, International Conference on Thermoelectrics, Baltimore, USA, Oct. 29-Sep. 2, 1999. "Growth and Thermoelectric Properties of Artificially Layered  $(\text{BiSb})_2\text{Te}_3$ ", S. Cho, Y. Kim, A. DiVenere, G. K. Wong, J. B. Ketterson, J. R. Meyer, International Conference on Thermoelectrics, Baltimore, USA, Oct. 29-Sep. 2, 1999.
8. "Anisotropic Seebeck and Magneto-Seebeck Coefficients of Bi and BiSb Alloy Thin Films", S. Cho, Y. Kim, A. DiVenere, G. K. Wong, J. B. Ketterson, J. R. Meyer, International Conference on Thermoelectrics, Baltimore, USA, Oct. 29-Sep. 2, 1999.
9. "Control of Antisite Defect Effect of  $\text{Sb}_2\text{Te}_3$  Thin Films", Y. Kim, S. Cho, A. DiVenere, G. K. Wong, J. B. Ketterson, J. R. Meyer, International Conference on Thermoelectrics, Baltimore, USA, Oct. 29-Sep. 2, 1999.
10. "Bi Substitution Effects on  $\text{Sb}_2\text{Te}_3$  Thin Films", Y. Kim, S. Cho, A. DiVenere, G. K. Wong, J. B. Ketterson, J. R. Meyer, International Conference on Thermoelectrics, Baltimore, USA, Oct. 29-Sep. 2, 1999.
11. "Artificially Atomic-Scale Ordered Superlattice Alloys for Thermoelectric Applications", S. Cho, Y. Kim, A. DiVenere, G. K. L. Wong, A. J. Freeman, J. B. Ketterson, L. J. Olafsen, I. Vurgaftman, J. R. Meyer, C. A. Hoffman, G. Chen, MRS Spring Meeting, San Francisco, Apr. 24-27, 2000. (Mat. Res. Soc. Symp. Proc. **626**, Z2.4 (2000))
12. "Thermal Conductivity of Bi/Sb Superlattice", D. W. Song, G. Chen, S. Cho, Y. Kim, J. B. Ketterson, MRS Spring Meeting, San Francisco, Apr. 24-27, 2000. (Mat. Res. Soc. Symp. Proc. **626**, Z9.1 (2000))

### **III. Conference Presentations**

1. "Bi and BiSb alloy thin films and superlattices for thermoelectric cooling devices", S. Cho, A. DiVenere, A. B. Shick, S. J. Youn, A. J. Freeman, G.K. Wong, J.B. Ketterson, J. R. Meyer and C.A. Hoffman, DARPA Kick-off Meeting, Pasadena, 1997.
2. "Observation of a power factor enhancement in MBE-grown  $\text{Bi}_{1-x}\text{Sb}_x$  alloy thin films", S. Cho, A. DiVenere, G. K. Wong, J. B. Ketterson, J. R. Meyer, and C. A. Hoffman, Int. Conf. Thermoelectrics, Dresden, Germany, 1997.
3. "Thermoelectric properties of doped BiSb alloy thin films", S. Cho, A. DiVenere, G. K. Wong, J. B. Ketterson, J. R. Meyer and C. A. Hoffman, APS March Meeting, Los Angeles, 1998.
4. "Electron structure and phase stability in Bi and Bi doped with Sb", A.B. Shick, D. L. Novikov, A. J. Freeman, and J. B. Ketterson, APS March Meeting, Los Angeles, 1998.
5. "Structural and thermoelectric properties of MBE-grown doped and undoped BiSb alloy thin films", S. Cho, A. DiVenere, Y. Kim, G. K. Wong, J. B. Ketterson, J. R. Meyer and C. A. Hoffman, International Conference on Thermoelectrics, Nagoya, Japan, May 24-28, 1998.

---

**REPORT DOCUMENTATION PAGE (SF298)**  
**(Continuation Sheet)**

---

6. "Structural and thermoelectric properties of MBE-grown  $\text{Bi}_2\text{Te}_3$  thin films", S. Cho, A. DiVenere, Y. Kim, G. K. Wong, J. B. Ketterson, J. R. Meyer and C. A. Hoffman, Electronic Materials Conference, Charlottesville, Virginia, June 24-26, 1998.
7. " $\text{Bi}_{1-x}\text{Sb}_x$  thin film and superlattice thermoelectrics", J. B. Ketterson, S. Cho, A. DiVenere, A. B. Shick, Y. Kim, S. J. Youn, A. J. Freeman, G. K. Wong, J. B. Ketterson, J. R. Meyer and C. A. Hoffman, MRS Fall Meeting, Boston, 1998.
8. "MBE growth and thermoelectric properties of  $\text{Bi}_2\text{Te}_3$  thin films", S. Cho, A. DiVenere, G. K. Wong, J. B. Ketterson, and J. R. Meyer, MRS Fall Meeting, Boston, 1998.
9. "Thermoelectric and structural properties of  $\text{Bi}_{1-x}\text{Te}_{1+x}$  thin films on CdTe(111)", Y. Kim, S. Cho, A. DiVenere, G. K. Wong, J. B. Ketterson, and J. R. Meyer, MRS Fall Meeting, Boston, 1998.
10. "Polarity conversion in CdTe/Bi(Sb)/CdTe heterostructures", S. Cho, A. DiVenere, Y. Kim, G. K. Wong and J. B. Ketterson, APS March Meeting, Atlanta, 1999.
11. "Artificially layered  $(\text{BiSb})_2(\text{TeSe})_3$  thin films: growth and thermoelectric properties", S. Cho, Y. Kim, A. DiVenere, G. K. Wong and J. B. Ketterson, APS March Meeting, Atlanta, 1999.
12. "Artificially Ordered BiSb Superlattice Alloy: Growth and Thermoelectric Properties", S. Cho, Y. Kim, A. DiVenere, G. K. Wong, J. B. Ketterson, J. R. Meyer, International Conference on Thermoelectrics, Baltimore, USA, Oct. 29-Sep. 2, 1999.
13. "Growth and Thermoelectric Properties of Artificially Layered  $(\text{BiSb})_2\text{Te}_3$ ", S. Cho, Y. Kim, A. DiVenere, G. K. Wong, J. B. Ketterson, J. R. Meyer, International Conference on Thermoelectrics, Baltimore, USA, Oct. 29-Sep. 2, 1999.
14. "Anisotropic Seebeck and Magneto-Seebeck Coefficients of Bi and BiSb Alloy Thin Films", S. Cho, Y. Kim, A. DiVenere, G. K. Wong, J. B. Ketterson, J. R. Meyer, International Conference on Thermoelectrics, Baltimore, USA, Oct. 29-Sep. 2, 1999.
15. "Control of Antisite Defect Effect of  $\text{Sb}_2\text{Te}_3$  Thin Films", Y. Kim, S. Cho, A. DiVenere, G. K. Wong, J. B. Ketterson, J. R. Meyer, International Conference on Thermoelectrics, Baltimore, USA, Oct. 29-Sep. 2, 1999.
16. "Bi Substitution Effects on  $\text{Sb}_2\text{Te}_3$  Thin Films", Y. Kim, S. Cho, A. DiVenere, G. K. Wong, J. B. Ketterson, J. R. Meyer, International Conference on Thermoelectrics, Baltimore, USA, Oct. 29-Sep. 2, 1999.
17. "Large Magnetoresistance and High Mobilities in Annealed Bi Thin Films", Y. Kim, S. Cho, A. DiVenere, G. K. Wong, A. J. Freeman, J. B. Ketterson, D. W. Stokes, I. Vurgaftman, J. R. Meyer, C. A. Hoffman, APS March Meeting, Minneapolis, Mar. 20-24, 2000.

---

**REPORT DOCUMENTATION PAGE (SF298)**  
**(Continuation Sheet)**

---

18. "Artificially Atomic-Scale Ordered Superlattice Alloys for Thermoelectric Applications", Y. Kim, S.Cho, A. DiVenere, G. K. L. Wong, A. J. Freeman, J. B. Ketterson, L. J. Olafsen, I. Vurgaftman, J. R. Meyer, C. A. Hoffman, G. Chen, MRS Spring Meeting, San Francisco, Apr. 24-27, 2000.
19. "A new magnetic semiconductor:  $(Zn,Mn)GeAs_2$  films", Y. Kim, B. Choi, S. Cho, A. DiVenere, G. K. Wong and J. B. Ketterson, APS March Meeting, Seattle, Mar. 12-16, 2001.

---

**REPORT DOCUMENTATION PAGE (SF298)**  
**(Continuation Sheet)**

---

**Scientific Personnel**

**1. Northwestern University**

J. B. Ketterson  
A. J. Freeman  
G. K. Wong  
A. DiVenere  
S. Cho  
Y. Kim  
A. B. Shick  
S. J. Youn

**2. Naval Research Laboratory**

J. R. Meyer  
I. Vurgaftman  
L. J. Olafsen  
D. W. Stokes  
C. A. Hoffman

---

**REPORT DOCUMENTATION PAGE (SF298)**  
**(Continuation Sheet)**

---

**Scientific Progress and Accomplishments**

1. We have grown Bi and BiSb alloy thin films and superlattices on CdTe(111)B over wide range of Sb composition using molecular beam epitaxy (MBE). The structural properties may be summarized as follows:

- (i) Bi and Bi-rich BiSb alloy thin films grow in layer-by-layer mode on CdTe(111)B.
- (ii) The crystallinity of BiSb thin films becomes poorer with increasing Sb concentration and improves with epilayer thickness.
- (iii) The out-of-plane lattice constant is consistently smaller than that of the bulk due to the lattice mismatch.
- (iv) The surface of BiSb films is rougher relative to Bi films.
- (v) By introducing a Te monolayer on the CdTe(111)A (Cd-terminated) face of Bi/CdTe superlattices, the growth mode of Bi was changed from 3D island to layer-by-layer growth.

2. We have studied the transport properties of MBE-grown-1 $\mu$ m-thick Bi<sub>1-x</sub>Sb<sub>x</sub> alloy thin films on CdTe(111)B over a wide range of Sb concentrations (0 < x < 0.183). Compared to the bulk alloy system, there are three important conclusions.

- (i) Semiconducting behavior was observed for the 3.5 and 5.1% Sb alloy thin films.
- (ii) The Sb concentration for the maximum thermoelectric power (TEP) and thermal bandgap shifts toward lower Sb concentrations, from 15 % to 9 %.
- (iii) The effective thermal bandgap and TEPs of the alloy thin films grown on CdTe(111) are larger than for bulk alloys.

The differences between thin film grown on CdTe(111) and the bulk alloys may be due to strain modifying the electronic band structure.

3. Superior superlattice (SL) growth was achieved by introducing a Te monolayer(ML) as a surfactant on the CdTe(111)A (Cd-terminated) face of Bi/CdTe SLs, changing the growth mode of Bi from 3D island to layer-by-layer growth. This result, while similar to the use of surface floating surfactants in its ability to improve the growth, is different in that the Te ML remains at the Bi/CdTe(111)A interface. One important aspect of this method is that the incorporated layer may also act as a dopant source with the appropriate choice of ML species. This technique has also been applied to grow BiSb/CdTe superlattices.

4. Using temperature-dependent resistivity we could derive the thermal bandgap of Bi<sub>1-x</sub>Sb<sub>x</sub> alloy thin films over a wide range of Sb concentration and observed a maximum band gap of 40 meV at x=0.09 (higher than bulk alloy, 18 meV). This large bandgap enhancement can be attributed to strain effects.

5. Measurements of the power factor ( $S^2\sigma$ ) of BiSb alloy thin films grown on CdTe(111)B show peaks at significantly higher temperature (250 K) than for bulk alloy (80 K). These results indicate that band engineering by strain can be used to change the transport properties and the optimum operating temperature can be controlled by band engineering.

6. We have successfully grown n and p-doped Bi and BiSb thin films by using Sn and Te as the dopant sources, respectively.

---

**REPORT DOCUMENTATION PAGE (SF298)**  
**(Continuation Sheet)**

---

7. In order to examine the viability of Bi/Bi<sub>2</sub>Te<sub>3</sub> superlattices, and other stacking sequences, for thermoelectric applications, we have grown high quality Bi<sub>2</sub>Te<sub>3</sub> thin films on CdTe(111)B substrates. Bi<sub>2</sub>Te<sub>3</sub> and its solid solutions are well known for their superior thermoelectric properties for near-room temperature applications. The measured thermopower and electrical conductivity of the undoped Bi<sub>2</sub>Te<sub>3</sub> films were  $\sim 200 \mu\text{V/K}$  and  $10^3 \text{ 1}/\Omega\text{cm}$ , respectively, comparable to the single crystal bulk values. We observed degenerate and nondegenerate behavior in the transport measurements by controlling the stoichiometry.

8. Quantitative Mobility Spectrum Analysis (QMSA), including mobility anisotropy of each L valley, was applied to the magneto-transport data of Bi and BiSb. The values of  $n_L$ ,  $p_L$ ,  $p_T$ , and the relaxation times vs. T were derived. Excellent agreement with the experimental results was obtained. QMSA will allow us to examine and model the thermopower in a much more realistic manner. The initial calculated S values are in good agreement with experimental results.

9. Total energy all-electron relativistic band structure calculations of the phase stability of bulk Bi were performed using the relativistic full-potential linear muffin-tin orbital wave method. It was demonstrated that the internal displacement leads to the stabilization of the observed A7 structure and drives a metal-semiconductor transition in Bi. An analysis of the combined effect of trigonal shear (rhombohedral) angle and internal displacement on the electronic structure of Bi was performed which demonstrated that a decrease of the trigonal shear angle leads to a semiconductor-semimetal transition. The dependence of the electronic structure on the Bi crystal structure provides the means of controlling the electronic structure and thermoelectric properties of Bi films by strains imposed by film/substrate lattice mismatch.

10. By alternately growing thin layers of Bi and Sb in a superlattice, we achieved an artificially ordered superlattice alloy (SLA) of Bi and Sb, where Sb layers replace specific atomic planes of Bi, e.g., Bi-Bi-Bi-Bi-Sb..., along the growth direction. Ordered alloys were achieved at the atomic-scale, as confirmed by x-ray diffraction satellite peaks.

11. We can then engineer the electronic band structure by changing the thicknesses of the Bi and Sb layers. While long-period samples showed semimetallic behavior, short period ones displayed semiconducting behavior. Temperature- and magnetic-field dependent Hall and resistivity measurements on the new alloy systems have been performed; both electron and hole carrier concentrations and mobilities were obtained from quantitative mobility spectrum analysis (QMSA), which confirmed that the alloys showed a semimetal to semiconductor transition as a function of the period of superlattice.

12. The new SLA opens a possibility to engineer the band structure to obtain more desirable thermoelectric and other properties. The power factor is comparable to that of the random alloy. We expect a lower thermal conductivity, due to an increase in phonon scattering from the Sb layers, which may result in a higher ZT over a random alloy. Thermal conductivity measurements are now under way by Gang Chen's group at UCLA.

13. We have grown Bi and BiSb alloy thin films on CdTe substrates with various orientations and measured their thermoelectric properties along the directions both perpendicular and parallel to the trigonal axis in order to test the performance of in-plane as well as the vertical cooling devices. Bi shows a strongly anisotropic and field- direction-dependent magneto-Seebeck effect, the so called "umkehr effect". We propose that for in-plane device application, the tilted structure of Bi or BiSb is preferable.

---

**REPORT DOCUMENTATION PAGE (SF298)**  
**(Continuation Sheet)**

---

14. Artificially-layered  $(\text{SbBi})_2\text{Te}_3$  films were successfully fabricated using layer-by-layer growth.  $\text{Bi}_2\text{Te}_3$  films grown layer-by-layer showed severe antisite defect behavior: Excess Te(Bi) occupies Bi(Te) lattice sites and acts as a dopant. In artificially layered  $\text{Sb}_{1.5}\text{Bi}_{0.5}\text{Te}_3$  and  $\text{Sb}_{1.6}\text{Bi}_{0.4}\text{Te}_3$  thin films, we have observed a reduction in thermopower, possibly caused by a modified electronic structure.

15. To obtain a good p-type thermoelectric material, we have grown  $\text{Sb}_2\text{Te}_3$  films on CdTe (111) substrates. The crystallinity and transport properties are strongly affected by nonstoichiometry via antisite defects. We found the optimum flow rate ratio of Te and Sb, where the films show comparable values with the bulk. At the growth temperature 200 °C, the optimum Te/Sb flow-rate ratio is 3.6, and the carrier concentration and mobilities are  $p=7.48\times10^{18} \text{ cm}^{-3}$ ,  $\mu=279 \text{ cm}^2\text{V}^{-1}\text{s}^{-1}$ , respectively.

16. High quality (00.1) oriented  $(\text{Sb}_{1-x}\text{Bi}_x)_2\text{Te}_3$  films were grown on CdTe (111). We varied the Bi concentration,  $x$ , from 0.15 to 0.3. While in bulk the optimum Bi concentration,  $x$ , is known to be 0.25, the maximum room temperature thermopower of the films occurred at  $x = 0.2$ , where the thermopower, effective carrier concentration, and mobility are  $184 \mu\text{V/K}$ ,  $4.53\times10^{19} \text{ cm}^{-1}$ , and  $64.0 \text{ cm}^2\text{V}^{-1}\text{s}^{-1}$ , respectively.

17. The electronic structure of  $\text{Bi}_2\text{Te}_3$  has been calculated by using the first principles full-potential linearized augmented plane wave (FLAPW) method. From the Fermi surface cross-sections, we found that the energy band structure quickly departs from a quadratic behavior near the band edges, which is different from the usual assumption made in modeling this system or fitting experimental data. A large, but finite, anisotropy in the effective mass shows that the bonding between layers is not completely of the van der Waals type but includes some covalent character. The valence band consists of two nearly degenerate sets of six fold degenerate extrema which merge into a single six fold degenerate set with decreasing energy. The conduction band consists of one set of six fold degenerate extrema and a second set of two fold degenerate extrema at slightly higher energy. These merge into two trident-like surfaces with increasing energy.

18. In order to obtain high quality Bi films, post annealing just below the melting point of Bi was performed. A 10  $\mu\text{m}$  Bi film grown on CdTe by MBE and subsequently annealed showed a large magnetoresistance ratio, 2700 at 5 K and 5 T, compared with 340 for the unannealed sample. An annealed 10  $\mu\text{m}$  Bi film on mica showed a much larger value of 12000 at 5 K and 5 T. This implies that a post annealing process may be one way to improve the quality of films when the highest possible deposition temperature for epitaxial growth is not compatible with the best transport properties. The large magnetoresistance ratio of annealed bismuth films can be ascribed to a higher mobility relative to that in unannealed samples.

## **Final Progress Report**

### **Strained and Unstrained $\text{Bi}_{1-x}\text{Sb}_x$ Superlattice Thermoelectrics**

Grant No: DAAG55-97-1-0130

J. B. Ketterson, A. J. Freeman, G. K. Wong, and A. DiVenere  
Department of Physics and Astronomy, Northwestern University, Evanston,  
IL 60208

J. R. Meyer  
Code 5613, Naval Research Laboratory, Washington, D.C. 20375-5338

## Table of Contents

Executive Summary	3
I. Introduction	4
II. Advantages of Bi-based Thermoelectrics	4
III. Sample Preparation and Thermoelectric Transport Measurements	6
A. Thin Film and Superlattice Growth	6
B. Thermoelectric and Magneto-transport Measurement Techniques	6
IV. Results and Discussion	7
A. Bi and BiSb Thin Films and Superlattices	7
A.1 Structural Properties	7
A.2 Thermoelectric and Transport Properties	10
A.3 Magneto-transport Measurement and QMSA Analysis	16
A.4 Electronic Structure, Phase Stability and Semimetallic Behavior of Bi	17
A.5 Doped BiSb Alloy Thin Films	21
A.6 Magnetoresistance of Bi Films	26
A.7 Anisotropy of Bi and BiSb Alloy Thin Films	32
A.8 Bi/CdTe Superlattices	37
B. Bi/Sb Superlattice Alloys (SLA)	40
B.1 Structural Properties of Bi/Sb Superlattices	40
B.2 Thermal Conductivity of Bi/Sb Superlattices	42
B.3 Structural Properties of Bi/Sb SLA	45
B.4 Thermoelectric and Transport Properties of SLA	47
V. Conclusions	50
VI. References	53
VII. List of Publication	56
VIII. Scientific Personnel	61

## Executive Summary

A program of experimental and theoretical research was proposed and executed in which thin films and artificial superlattices containing Bi-based semimetals and semiconductors as the substitutes were fabricated, characterize and simulated in order to develop thermoelectric device applications from these novel materials. Those thin films and superlattices presented novel electronic band structures which result from bandgap engineering introduced by strain effect, doping concentration, individual layer thicknesses, and growth directions; and thermal conductivity reduction in superlattices was also observed. Specific accomplishments of the program include: (1) Superlattices of Bi/Sb with sub-atomic monolayer thickness of Sb, which have electrical properties comparable to those of BiSb alloy thin films, were successfully fabricated and characterized. (2) Thermal conductivity reduction in Bi/Sb superlattices, compared with the bulk random alloy, was observed. (3) A number of materials, for the barrier layer in the quantum well superlattice structure, was screened with the result that CdTe is still the best candidate. (4) Using a novel Te surfactant growth technique, superlattices with superior structural qualities (as probed by TEM and XRD) can be synthesized on CdTe(111)A substrate. (5) Strained Bi thin films with thicknesses approaching 1  $\mu\text{m}$  were grown on CdTe. (6) We have observed a modest enhancement of the thermoelectric power in Bi/CdTe superlattices due to quantum confinement (as proposed). (7) An enhanced thermopower and bandgap were observed in BiSb alloy thin film as a result of coherency strain effects; this enhancement results, in turn, in a power factor enhancement suggesting strain-induced band engineering can be used to control thermoelectric properties. (8) Te and Sn doping experiments were performed to enhance n-type response and produce p-type behavior. (9) The QMSA technique was applied from which the temperature dependence of the carrier concentrations and scattering lifetimes was deduced. (10) Anisotropy in the magneto-electric properties of Bi and BiSb alloy thin films were investigated in a magnetic field. (11) Large enhancement in magnetoresistance of Bi thin films (largest in the film form) after post annealing was observed and studied; ascribed to the result of enhancement of the electron mobility.

## I. Introduction

Scientific, political, and social concerns over depletion of the ozone layer have resulted in an increase effort within DoD and elsewhere to replace chlorofluorocarbon (freon) based refrigerants with more environmentally-sound cooling materials. While some hydrocarbons and hydrofluorocarbons may provide short-term relief from the adverse effects of chlorofluorocarbons, all of those tested thus far have significant disadvantages. Thermoelectric cooling represents an attractive alternative technology, which completely eliminates liquids/gases as well as all moving parts from the cooling cycle. Additional commercial and military impetus toward thermoelectric technology is provided by other critical applications, such as the small-volume cooling of computer processor chips and motherboards, high  $T_c$  superconducting devices, infrared detector arrays, and space-based electronic and detector systems (for which cooling requirements often represent a primary factor limiting payload and lifetime). The development of improved thermoelectric materials is therefore urgently needed, and would have broad impact if successful.

The accepted figure of merit for thermoelectric materials is  $ZT$ , where  $T$  is the absolute temperature and  $ZT = S^2\sigma / \kappa$  (where  $S$  is the thermoelectric power (TEP) or Seebeck coefficient,  $\sigma$  is the electrical conductivity, and  $\kappa$  is the thermal conductivity). Since  $\text{Bi}_2\text{Te}_3$  and related alloys have yielded the largest  $ZT$  to date (in the absence of a magnetic fields), they have historically tended to be the materials of choice for thermoelectric devices.

In this report, we employed a new scheme of superlattice alloy and band structure engineering in conjunction with MBE to grow artificial material systems which have the potential to significantly advance the state-of-art in thermoelectrics. We examined the structural, magneto-transport, and thermoelectric properties of Bi and BiSb thin films and superlattices.

## II. Advantages of Bi-Based Thermoelectrics

Bi is a semimetal with a rhombohedral crystal structure which has an energy overlap (~38 meV) between the conduction and valence bands, high carrier mobilities, and small effective masses. Because of these properties, Bi was used in early studies of quantum transport and the quantum size effect, as well as in more recent investigations of quantum confinement in thin films and superlattices such as Bi/PbTe<sup>1,2</sup>, Bi/CdTe<sup>3-5</sup> and Bi<sub>1-x</sub>Sb<sub>x</sub>/Bi.<sup>6</sup>

In semimetallic bulk Bi, the thermoelectric figure of merit is suppressed by competing electron and hole contributions. However, Gallo *et al.*<sup>7</sup> pointed out quite early that Bi, which has a low bulk  $ZT$  of 0.4 at 300 K, would have the largest ambient-temperature figure of merit of any known material ( $ZT \sim 1.8$ ) if one could somehow eliminate the hole population from the system. More recently, Hicks and coworkers<sup>8,9</sup> proposed that  $ZT$  can be enhanced considerably in Bi-based superlattices due in part to the semimetal to semiconductor transition which occurs when the Bi well thickness is decreased to less than ~300 Å. These reports have attracted considerable interest in the thermoelectric community because  $ZT \sim 1$  has been the technological limit for the past few decades. Although several subsequent investigators<sup>10-14</sup> have pointed out that the projection by Hicks *et al.* of a 2D  $ZT$  larger than 8 for a 10 Å well thickness is unrealistic, there is general agreement that  $ZT > 1$  may be attainable in semiconducting

Bi-based superlattices. It is therefore significant that a recent magneto-transport investigation of Bi thin films grown on CdTe substrates<sup>4,5</sup> found experimental evidence for a confinement-induced semimetal to semiconductor transition in a 200 Å Bi thin film, with a 40 meV positive energy gap reported.

The  $\text{Bi}_{1-x}\text{Sb}_x$  alloy system can be either a semiconductor or semimetal depending on the Sb concentration,<sup>15-31</sup> as may be seen from the band structure in Fig. 1. The addition of Sb to Bi causes the  $L_s$  and T bands to move down with respect to the  $L_a$  band. At  $x = 0.04$  the L bands invert<sup>16,17</sup> and at  $x = 0.07$  the overlap between the hole T and  $L_a$  bands disappears,<sup>18</sup> resulting in an indirect bandgap semiconductor for  $x < 0.09$ . For  $0.09 < x < 0.15$ ,  $\text{Bi}_{1-x}\text{Sb}_x$  is a direct gap semiconductor with a maximum bandgap in the range 18-20 meV for 12~15% Sb concentration.<sup>15,20,21</sup> For  $x > 0.15$ , the hole H band lies above  $L_s$  and we again have an indirect semiconductor. Finally at  $x = 0.22$ , H crosses  $L_a$ , and the alloys are again semimetallic up to  $x = 1$  (pure Sb). In addition, the BiSb band structure depends on temperature, external pressure,<sup>25-29</sup> and magnetic field.<sup>24</sup> With properties such as a small bandgap, high mobility and a reduced lattice thermal conductivity, semiconducting Bi-rich  $\text{Bi}_{1-x}\text{Sb}_x$  alloys may potentially be used as an n-type thermoelement operating around 80 K. The thermoelectric figure of merit, ZT, is 0.88 at 80 K in a magnetic field of 0.13 T.<sup>20</sup>

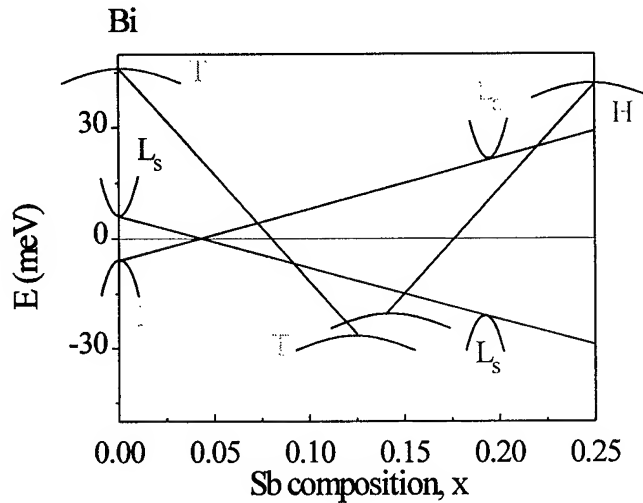


FIG. 1. Variation of energy bands near Fermi level of bulk  $\text{Bi}_{1-x}\text{Sb}_x$  alloys as a function of Sb composition,  $x$ , in the interval  $0 \leq x < 0.25$ .

### III. Sample Preparation and Thermoelectric Transport Measurements

#### A. Thin Film and Superlattice Growth

Bi and BiSb thin films and superlattices were grown on semi-insulating CdTe(111)B substrates by molecular beam epitaxy (MBE). The base pressure of the growth chamber was in the  $10^{-10}$  Torr range. The growth direction of the Bi and BiSb alloy films on CdTe(111)B is parallel to the trigonal axis. The substrates used in this experiments are In-doped CdTe(111) purchased from II-VI Inc. The substrates are mechanochemically polished on both sides. The crystal polarities are predetermined by the manufacturer and marked by a small dot on the A face edge. The dimensions of the substrates are 1cm $\times$ 1cm $\times$ 0.5mm. Before growing films, the substrate is treated to obtain a clean and smooth surface. The CdTe substrates were rinsed in Methanol with the help of an ultrasonic generator for 5 minutes, etched in a 1% Br-Methanol solution for 20 seconds to remove surface contaminates, and finally rinsed in Methanol using an ultrasonic generator to remove any possible residue of Br.

A 3000 Å CdTe buffer is then grown on the CdTe substrate at a growth temperature of 250 °C at a growth rate of  $\sim$ 0.45 Å/sec; the corresponding CdTe cell temperature is  $\sim$ 520 °C. After the buffer layer is grown, a RHEED study is performed again. The surface condition of the substrate is then significantly improved: the RHEED pattern is streaky, the reconstruction pattern is clearer, and Kikuchi lines appear indicating a good surface crystalline quality. The substrate temperature is then set to the desired growth temperature. The composition of Bi and Sb was controlled by a quartz thickness monitor. The accuracy of this technique has been examined and confirmed by inductively coupled plasma spectroscopy analysis. The lattice constants of Bi and Sb are 4.546 and 4.308 Å, respectively. Consequently the lattice mismatch of  $\text{Bi}_{1-x}\text{Sb}_x$  with CdTe(111)B (4.58 Å) increases from 0.7 % to 1.6 % between  $x = 0$  and  $x = 0.16$ .

#### B. Thermoelectric and Magneto-transport Measurement Techniques

To measure the TEP, we used the differential method, in which a small temperature difference is maintained across the sample to produce the thermoelectric voltage:  $\Delta V = S\sqrt{T} + b(\sqrt{T})^2 + \dots$ , where  $b$  is a constant. In this experiment, the temperature difference was restricted to the range of 0.1-1 °C, in order to assure that terms higher than second-order in  $\sqrt{T}$  may be ignored. To eliminate the spurious thermal voltage within the circuit, we measured the thermoelectric voltage (in the steady state) for small incremental changes in the temperature differences. The thermoelectric voltage ( $\Delta V$ ) vs. temperature difference values ( $\sqrt{T}$ ) were plotted and from the slope of the linear region, we could determine the TEP. To measure the temperature difference across the sample, we used a differential copper-constantan thermocouple. The thermoelectric voltage was measured by using thin copper leads and was later corrected for the TEP of the leads to obtain the final results. The accuracy of this procedure was tested by measuring the TEP of a high  $T_c$  superconducting  $\text{YBa}_2\text{Cu}_3\text{O}_{7.8}$  thin film; below the critical temperature of 80 K the measured thermoelectric voltage corresponded to the TEP of the copper leads ( $S = 0$  for the superconductor). The measured values as a function of temperature were in agreement with literature values for Cu. The thermoelectric voltage and the thermocouple voltages were measured to an accuracy of a nanovolt using a Keithley 181 nanovoltmeter.

The magnetotransport results were analyzed using a Quantitative Mobility Spectrum Analysis (QMSA) procedure<sup>32,33</sup> which derives carrier densities and mobilities for all of the species present. A number of important improvements<sup>34</sup> were recently incorporated into QMSA, which now offers a better overall extraction of information from experimental data sets than any previous technique.

#### IV. Results and Discussion

##### A. BiSb Thin Films and Superlattices

###### A.1. Structural Properties of BiSb Thin Films

In the zinc-blende structure, the two (111) faces, designated by A and B, are different and polar. In CdTe(111), the A face is terminated by triply bonded Cd atoms, while triply bonded Te atoms terminate the B face as shown in Fig. 2. Based on RHEED and TEM studies, we observed that the growth properties of Bi depend on whether the growth is started on the A-face or B-face. The RHEED patterns during Bi growth on (111)B showed no reconstruction. The Bi layer on CdTe(111)B grows in a layer-by-layer mode, while on CdTe(111)A it grows in a 3D-island mode during the first  $\sim 50$  Å of growth, and coalesces thereafter. Therefore we used the CdTe(111)B surface as a substrate for the growth of Bi and BiSb alloy thin films. Figure 3 shows the RHEED patterns of 1- $\mu\text{m}$ -thick Bi thin film grown on CdTe(111)B. The RHEED patterns of the Bi film show streaks and Kikuchi lines, implying high crystallinity and a smooth surface of the Bi layer. However, the  $\text{Bi}_{0.91}\text{Sb}_{0.09}$  RHEED pattern shows some spots along the (1 $\bar{1}$ 0) azimuth. These spots are observed even after several thousand Å of BiSb film growth. The observed spotty patterns of  $\text{Bi}_{0.91}\text{Sb}_{0.09}$  films indicate that the surface morphology of BiSb is rougher than that of Bi.

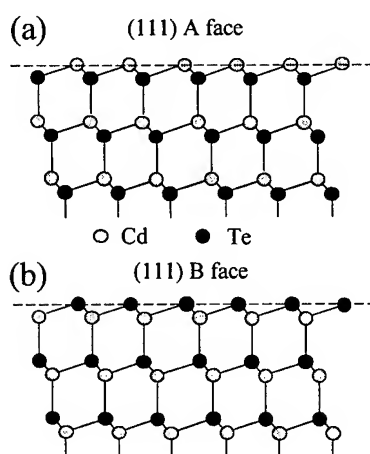


FIG. 2. The crystal structure of CdTe(111) near a surface.

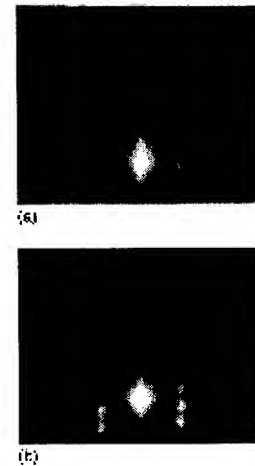


FIG. 3. RHEED patterns of 1  $\mu\text{m}$  thick (a) Bi and (b)  $\text{Bi}_{0.91}\text{Sb}_{0.09}$  alloy films.

Figure 4 shows the  $\theta$ - $2\theta$  XRD pattern of a 1- $\mu\text{m}$ -thick Bi film on CdTe(111)B, displayed on a logarithmic intensity scale. It is observed that only sharp (00*l*) peaks are present, which implies *c*-axis growth of Bi, with the trigonal axis perpendicular to the substrate. As discussed above, the growth direction of Bi on CdTe(111) is of interest in

connection with quantum transport studies. The rhombohedral crystal structure can be described with a hexagonal unit cell containing six atoms at  $(000; \frac{2}{3}, \frac{1}{3}, \frac{1}{3}; \frac{1}{3}, \frac{2}{3}, \frac{2}{3}) \pm 00u$ .

Figure 5 shows a plot of the out-of-plane (c-axis) lattice constants in the hexagonal unit cell representation for  $\text{Bi}_{1-x}\text{Sb}_x$  alloy films versus the Sb concentration; also plotted is the predicted bulk lattice constant from Vegard's law (using  $c = 11.862$  and  $11.274$  Å as parameters of bulk Bi and Sb, respectively) and that reported for epitaxial thin films grown on  $\text{BaF}_2(111)$  substrates. Adding Sb to Bi decreases the out-of-plane lattice constant and, for a given Sb concentration, the lattice constants for our films are consistently smaller than those of the bulk, which is consistent with the presence of tensile strain given that Poisson's ratio for BiSb is positive. The out-of-plane lattice constants of  $\text{Bi}_{1-x}\text{Sb}_x$  alloy thin films grown on  $\text{CdTe}(111)$  satisfy the following relation,  $c = (11.858 - 0.646 x)$  (Å) at 298 K, where  $x$  is the fraction of Sb. The lattice constant contraction arises from tensile strain in the film caused by the lattice mismatch between the epilayer and the substrate, which varies from 0.7 % for Bi to 1.6 % for  $\text{Bi}_{0.84}\text{Sb}_{0.16}$ . On the other hand, an expansion of the out-of-plane lattice constants for 1-μm alloy thin films on  $\text{BaF}_2$  were reported by Morelli *et al.*,<sup>30</sup> due to the compressive strain and larger lattice mismatch associated with  $\text{BaF}_2$  substrates. The strain in the BiSb films caused by the lattice mismatch may affect the band structure of BiSb thin films, inducing a possible bandgap enhancement for BiSb alloy films grown on  $\text{CdTe}(111)$  relative to a bulk BiSb alloy. From a simple analysis of the temperature dependence of the electrical conductivity,<sup>35,36</sup> the effective bandgap for a 9% Sb BiSb thin film is 40 meV, while that for the bulk is 20 meV. The Sb concentration for the maximum bandgap changes from 15% to 9%. The transport properties for these films will be discussed in the next section (IV.A.2).

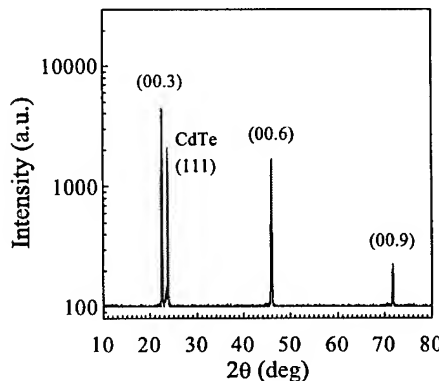


FIG. 4.  $\theta$ - $2\theta$  XRD pattern of Bi thin film.

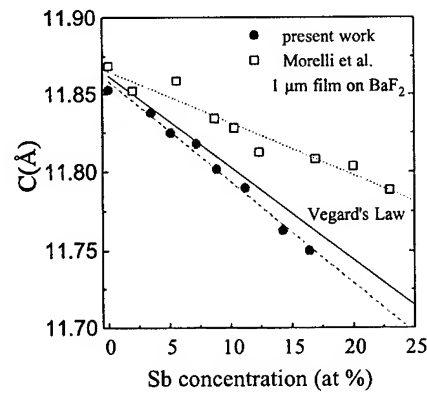


FIG. 5.  $c$ -axis lattice constant in a hexagonal unit cell of  $\text{Bi}_{1-x}\text{Sb}_x$  alloy thin films as a function of Sb concentration. The full line gives results for bulk alloys.

We have determined the x-ray rocking curve full width at half maximum (FWHM) for  $\text{Bi}_{1-x}\text{Sb}_x$  alloy thin films for the (00.3) peak. The results for 1 μm thick BiSb alloy thin films are shown in Fig. 6. The FWHM of the pure Bi film is  $0.06^\circ$ . As the Sb concentration increases, the FWHM increases linearly, implying poorer crystallinity of

BiSb thin films with increasing Sb composition. This is typical alloying behavior, caused by the difference in the lattice constants of Bi and Sb and associated inhomogeneities, etc. The FWHM of BiSb with 16.4% Sb is  $0.3^\circ$ . It should be noted that the FWHM of commercial CdTe(111) substrates is slightly larger ( $0.054^\circ$ ) compared to typical III-V substrates ( $<0.01^\circ$ ). Higher quality CdTe substrates could enhance the crystallinity of the pure Bi films.

In order to investigate the thickness-dependent crystallinity of BiSb thin films, we have examined  $\text{Bi}_{0.91}\text{Sb}_{0.09}$  thin films with different thicknesses from 0.1 to 12  $\mu\text{m}$ . It is noted that for the 9 % Sb composition of BiSb alloy, the lattice mismatch is 1.1%. As the film thicknesses increases the FWHM decreases rapidly, indicating better crystallinity in thicker films, as shown in Fig. 7. Above 3  $\mu\text{m}$  thickness, the FWHM saturates. The thickness dependent FWHM study suggests that the crystallinity improves in thick films. The thickness dependent x-ray FWHM may be due to a thickness dependent compositional inhomogeneity of the film or a strain relaxation through misfit dislocations at large thicknesses.

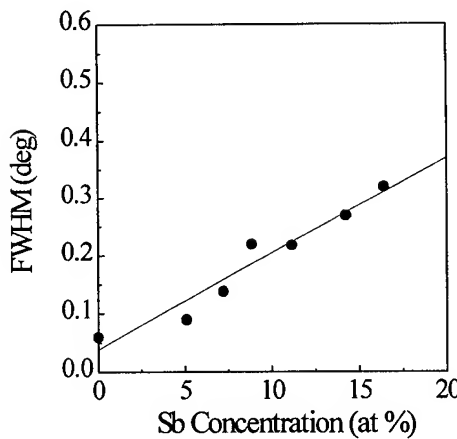


FIG. 6. FWHM vs. Sb concentration determined for the (00.3) peak.

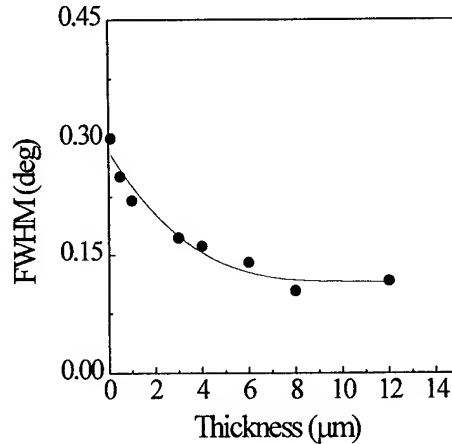


FIG. 7. XRD FWHM vs. epilayer thickness determined for the (00.3) peak.

Figures 8(a) and (b) show AFM images of the 1  $\mu\text{m}$  thick Bi and  $\text{Bi}_{0.86}\text{Sb}_{0.14}$  alloy thin films, respectively. The triangular, regular patterns were dominant in the pure Bi film, which may indicate the presence of relatively large, untwinned single crystals of Bi on CdTe(111)B. However, the 14.5% Sb alloy film shows a combination of regular and irregular triangular shaped surfaces: some triangles point upward and others downward, which may indicate the presence of twins in the BiSb alloy thin films. The surface of the BiSb film is rougher than that of the Bi film, which was already expected on the basis of the spotty RHEED patterns in the BiSb alloy thin films.<sup>37</sup>

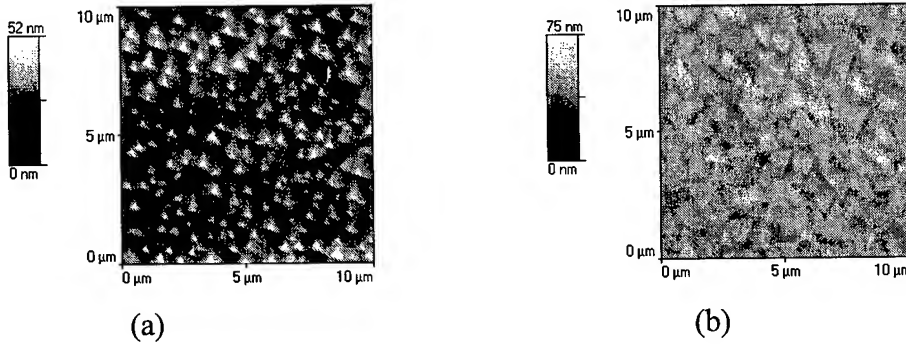


FIG. 8. Surface AFM pictures of (a) Bi and (b)  $\text{Bi}_{0.86}\text{Sb}_{0.14}$  thin films.

### A.2. Thermoelectric and Transport Properties of BiSb Thin Films

We have prepared  $\text{Bi}_{1-x}\text{Sb}_x$  alloy thin films with  $x = 0, 0.019, 0.035, 0.051, 0.072, 0.088, 0.112, 0.143, 0.164$ , and  $0.183$ . The temperature-dependent electrical resistivities of the  $\text{Bi}_{1-x}\text{Sb}_x$  alloy thin films with various Sb compositions are shown in Fig. 9(a) and (b). At room temperature, the resistivity differences between the various compositions is small. However, as the temperature decreases the behavior changes significantly. The 1.9% Sb concentration sample shows a slightly increased resistivity at low temperature. As the Sb concentration increases, the resistivity increases rapidly up to 8.8% Sb concentration as shown in Fig. 9(a). It should be noted that the 8.8% Sb alloy has the highest resistivity at low temperature. With the further addition of Sb, the resistivity decreases as shown in Fig. 9(b). The 18.3% Sb alloy shows a slightly increased resistivity at low temperature. Note that at low temperatures the resistivity saturates.

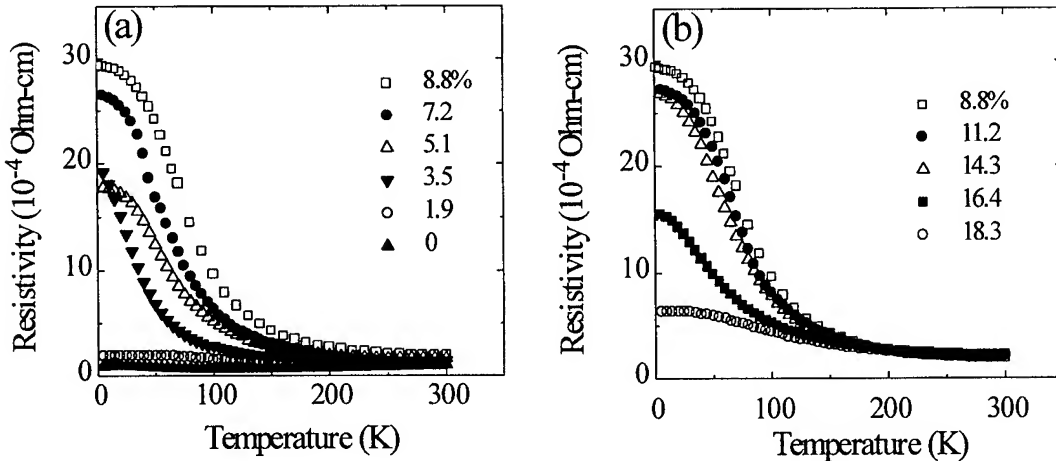


FIG. 9. The temperature dependence of the electrical resistivities of  $\text{Bi}_{1-x}\text{Sb}_x$  alloy thin films grown on  $\text{CdTe}(111)\text{B}$  with various Sb concentrations. The 8.8% Sb alloy was graphed twice for comparison.

The saturation of the resistivity at low temperature may indicate the existence of an impurity band.<sup>21</sup> In n-type semiconductors, Wannier<sup>38</sup> treated an impurity as a quasi-hydrogenic atom in a continuous dielectric material with the extra electron bound to a

spherically symmetric positive charge embedded in a solid dielectric material. The binding energy of the electron to the impurity atom is then

$$E_n = -\frac{e^4 m^*}{2n^2 \hbar^2 \epsilon^2} \approx -\frac{13.6}{n^2 \epsilon^2} \left( \frac{m^*}{m_0} \right) \text{ eV}, \quad (1)$$

and the orbital radius of the electron is

$$r_n = \frac{n^2 \hbar^2 \epsilon}{e^2 m} \left( \frac{m_0}{m^*} \right) \approx 0.53 \frac{m_0}{m^*} n^2 \epsilon \text{ \AA}, \quad (2)$$

where  $m_0$  is the electron rest mass,  $m^*$  is the effective mass, and  $\epsilon$  is the dielectric constant. The work necessary to separate the electron from the atom is given by

$$\Delta E = E_\infty - E_1 \approx \frac{13.6}{\epsilon^2} \left( \frac{m^*}{m_0} \right) \text{ eV}. \quad (3)$$

BiSb alloys have a high dielectric constant<sup>39</sup> ( $\sim 100$ ) and low effective masses ( $\sim 0.01 m_0$ ). Using Eq.'s (2) and (3) yields  $\Delta E \sim 1.4 \times 10^{-5}$  eV and  $r_I \sim 5.3 \times 10^3$  \AA. In comparison, Si has a  $\Delta E \sim (1.0-4.9) \times 10^{-2}$  eV and  $r_I \sim (1.9-3.7) \times 10^1$  \AA for  $\epsilon = 11.8$  and  $m^*/m = 0.33$ . Furthermore, free carriers are expected to screen out the bound state of high doping levels since the screening length is much less than the orbital radius. These values are dependent on the type of impurity.<sup>40</sup> The impurity levels are localized discrete levels for low impurity concentrations. Above some critical concentration,  $n_i$ , the wavefunctions of neighboring impurities overlap and the impurity levels evolve into impurity bands. A rough estimate for the critical concentration for Bi-rich BiSb is  $n_i \approx 1/(2r_I)^3 \approx 10^{12} \text{ cm}^{-3}$ , which is rather low compared to a concentration  $\sim 10^{19} \text{ cm}^{-3}$  required for Si. Thus this low critical impurity concentration estimate supports the possible presence of impurity bands in Bi-rich BiSb alloy thin films since the impurity concentrations are of the order  $10^{16} \text{ cm}^{-3}$  for highest purities available (99.9999%).

In Figs. 10(a) and (b), the TEP values for the  $\text{Bi}_{1-x}\text{Sb}_x$  alloy thin films are plotted as a function of temperature between 20 and 300 K. The TEP of a pure Bi film is seen to be in good agreement with the previous single crystal values for conduction perpendicular to the trigonal axis as reported by Gallo *et al.*<sup>7</sup> and Korenblit *et al.*<sup>41</sup> The addition of Sb into Bi affects the TEP values. The 1.9% Sb alloy shows a slightly enhanced TEP. As the Sb concentration increases, the magnitude of the alloy TEP increases. The maximum TEP was obtained at 8.8% Sb alloy and thereafter decreases with a further increase in Sb composition, as shown in Fig. 10(b). The TEP values for the alloy thin films are seen to be larger than those for the pure Bi film. At low temperatures, the magnitude of the TEP increases linearly with increasing temperature as in bulk. For alloys with Sb concentrations between 3.5% and 16.4% it reaches a peak at some intermediate temperature and then decreases at high temperature. However, the TEP of the 1.9% and 18.3% Sb alloy thin films shows a temperature dependence similar to that of pure Bi, in which no distinct peak is observed. For a thermoelectric material containing both electrons and holes, the total TEP may be modeled by the relation:  $S = (\sigma_e S_e + \sigma_p S_p) / (\sigma_e + \sigma_p)$ , where  $\sigma_e$  and  $\sigma_p$  are the electrical conductivities and  $S_e$  and  $S_p$  are the TEPs for electrons and holes, respectively. The observed negative TEP implies a higher mobility for electrons than for holes (assuming  $n = p$ ). The magnitude of the TEP increases with decreasing temperature above a certain temperature. This increase is due to the freeze-out of electrons and holes and an increase of the electron-to-hole mobility

ratio with decreasing temperature, which depends on the Sb concentration. At low temperature, the magnitude of the TEP decreases linearly with decreasing temperature as in bulk, which is due to the greater degeneracy of the carrier populations.

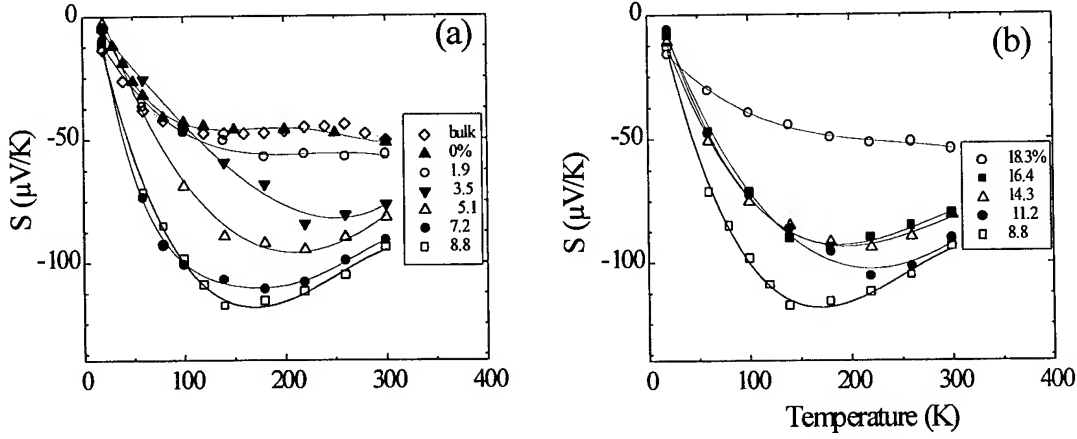


FIG. 10. TEPs of  $\text{Bi}_{1-x}\text{Sb}_x$  alloy thin films as a function of temperature perpendicular to the trigonal axis. The 8.8% Sb alloy was graphed twice for comparison.

For a nondegenerate intrinsic semiconductor, assuming the contributing bands are parabolic with the same density of states and that the carriers are scattered primarily by acoustic phonons, the electrical resistivity and TEP can be written as<sup>40</sup>:

$$\rho = \rho_0 \exp\left(\frac{E_C - E_F}{k_B T}\right), \quad (4)$$

and

$$S = \frac{k_B}{e} \left( \frac{E_C - E_F}{k_B T} + B \right), \quad (5)$$

where  $\rho_0$  is a constant and  $E_c$ ,  $E_F$ , and  $B$  are the conduction band edge, Fermi energy, and scattering parameter, respectively. The term  $E_c - E_F$  can be expressed as

$$E_C - E_F = \frac{1}{2}(E_{g0} - AT) \quad (6)$$

where  $E_{g0}$  is the bandgap at 0 K and  $A$  is a constant. Using Eq.'s (4)-(6), the bandgap can be extrapolated to 0 K. Equation (1) has been used to derive the thermal effective bandgap in the semiconducting BiSb alloy system. Strictly speaking, it is hard to apply the above formula directly to BiSb because acoustic phonon scattering does not dominate in the thin films at low temperatures and because there are multiple hole bands (at L, H and T). The band which makes the dominant contribution to the temperature dependence of the resistivity depends on a complex interplay between the bandgap, density of states, mobility and temperature. However, for a simple and qualitative understanding of the BiSb alloy system we used the above simple model to interpret our results and to compare our results with the reported literature values for bulk material and thin films.

The fitted thermal bandgaps using Eq. (4) are shown in Fig. 11, compared with similarly calculated literature values for bulk<sup>15,20-22</sup> and 1  $\mu\text{m}$ -thick-epitaxial thin films

grown on  $\text{BaF}_2(111)$ .<sup>30</sup> As mentioned in Section II, the semiconducting behavior in bulk occurs at alloys compositions between 7 and 22% Sb with a maximum bandgap (18–20 meV) at  $x = 0.15$ . However, we have observed several differences relative to the bulk system. The 3.5 and 5.1% Sb alloys (corresponding to semimetals in bulk) show semiconducting behavior. The Sb concentration for the maximum bandgap shifts to a lower Sb concentration, from 15% in bulk to 9%. It is seen that the effective bandgaps of thin films grown on  $\text{CdTe}(111)$  are larger than the bulk values, with a maximum gap of 40 meV.

Figure 12 shows a comparison of the TEP between our thin films and bulk values as a function of Sb concentration at several temperatures. Three important points are evident: (i) The magnitude of the TEP of the alloys with Sb concentrations of 3.5 and 5.1% increases with decreasing temperature above 220K, indicative of semiconducting behavior. (ii) The Sb concentration for the maximum TEP has shifted to lower Sb concentrations, from 15% to 9%. (iii) The TEPs of the alloy thin films grown on  $\text{CdTe}(111)$  are larger than for bulk alloys, which is consistent with an enhanced gap (see Eq. (5)). All these differences observed in TEP measurements are consistent with the electrical resistivity results. In both transport measurements (electrical resistivity and TEP), the 8.8% Sb alloy has highest effective gap and the highest TEP. Using Eq. (5), we have fitted our TEP data to obtain effective bandgaps. The overall behavior of the bandgap with Sb concentration is quite similar to that determined by the temperature dependent resistivity. The maximum bandgap is  $E_{g0} = 35$  meV at 8.8% Sb as compared to  $E_{g0} = 40$  meV determined from the temperature-dependent electrical resistivity.

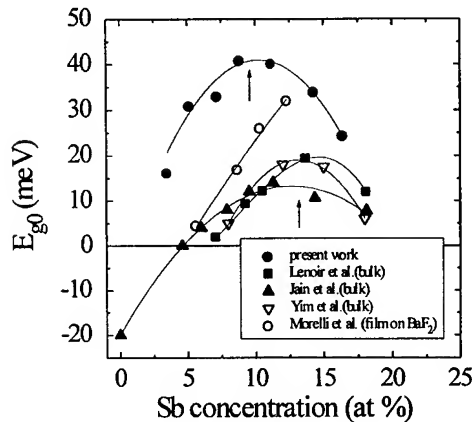


FIG. 11. Effective thermal bandgap  $E_{g0}$  at 0 K as determined from temperature dependent electrical resistivity measurement versus Sb concentration.

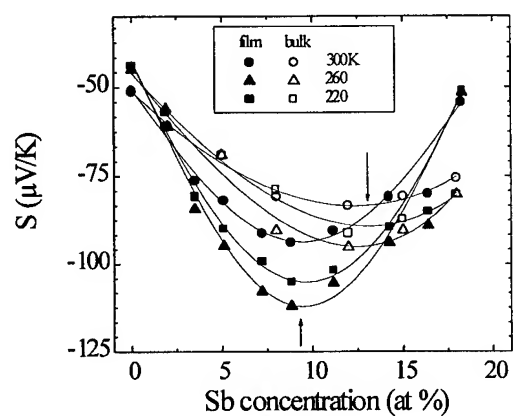


FIG. 12. TEPs of  $\text{Bi}_{1-x}\text{Sb}_x$  alloy thin films and bulk crystal as a function of Sb concentration at several temperatures: 220K, 260K, and 300K.

A possible explanation for the appearance of semiconducting behavior in the 3.5 and 5.1% Sb alloys, a shift in Sb concentration with maximum bandgap, and an enhanced effective bandgap over bulk  $\text{BiSb}$  alloy, may be the strain effect, which modifies the electronic band structure, resulting in a shift of the relative position of the electron and hole bands. The semimetallic behavior of Bi and Sb is related to their rhombohedral A7

crystal structure. The A7 structure has two atoms per unit cell located at  $(u, u, u)$  and  $(-u, -u, -u)$  and a rhombohedral angle  $\alpha$  (for Bi,  $u = 0.237$  and  $\alpha = 57^\circ 14.2'$ ; for Sb,  $u = 0.233$  and  $\alpha = 57^\circ 6.5'$ ). Recently, total energy all-electron relativistic band structure calculations of the phase stability of bulk Bi were performed using the full-potential, linear, muffin-tin-orbital method.<sup>42</sup> It was demonstrated that the internal displacement leads to a stabilization of the observed A7 structure and drives a metal-semimetal transition in Bi. (Bi is a metallic for  $u = 0.25$ ). In addition, the increase in the trigonal shear angle with internal displacement (to  $u = 0.237$ ) leads to a semimetal-to-semiconductor transition.<sup>42</sup> For  $\alpha = 60^\circ$  (cubic), Bi becomes a direct bandgap semiconductor with the calculated gap of 30 meV at the T points. This calculation, which will be presented in a later section (IV.A.4), suggests that the dependence of the electronic structure on the Bi crystal structure provide a way of controlling the electronic structure. The presence of tensile strain in our films grown on CdTe(111) leads to an increase in the rhombohedral angle, which drives the electronic band structure of BiSb toward semiconducting behavior as mentioned above. The appearance of semiconducting behavior in the 3.5 and 5.1% Sb alloys, the shift of the Sb concentration for the maximum bandgap, and the enhanced bandgap over bulk BiSb alloys are all consistent with strain-altered band structure. On the other hand, Morelli *et al.*<sup>30</sup> observed the slightly enhanced gap in BiSb alloy thin films grown on BaF<sub>2</sub>(111) substrates. They attributed their enhanced bandgap to a compressive strain caused by the smaller lattice constant of the substrate (4.38 Å). As shown in Fig. 5, the lattice constant for their films is consistently larger than that of the bulk. This is in contradiction with results of Shick *et al.*'s band calculations. On the other hand, the large effect of hydrostatic pressure on the band structure of bulk Bi and BiSb alloys has been reported over a wide range of Sb concentrations. Both the L and T bands move up and down, depending on pressure and Sb concentration.<sup>24</sup>

To evaluate the suitability of BiSb alloy thin films for a thermoelectric module, we have plotted the power factor ( $S^2/\rho$ ) as a function of temperature in Fig. 13. The temperature-dependent power factor for a 7.2% BiSb alloy thin film is compared to bulk Bi and Bi<sub>0.88</sub>Sb<sub>0.12</sub> alloy crystals. Only the largest literature values are graphed in Fig. 13. These results show that power factors for the BiSb thin films peak at a significantly higher temperature (250K) than for previous results for the bulk alloy (80K). The peak temperature mainly depends on the electrical resistivity behavior. With a small bandgap of 20 meV in bulk, the electrical resistivities of the alloys decreases with decreasing temperature below room temperature until a certain temperature, related to the thermal energy (e.g. at 300 K,  $k_B T \sim 25$  meV). We observe that the 1.9, 3.5, 16.4 and 18.3% alloys have a minimum in the resistivity below room temperature. However, for other films, e.g. 7.2% Sb alloy (having maximum power factor), the electrical resistivity increases with decreasing temperature. Therefore the peak occurs at a higher temperature. These results imply that thermoelectric properties such as the optimum operating temperature and the magnitude of the figure of merit Z, depend on the magnitude of the bandgap of the material and can be controlled by band engineering.

Figure 14 shows the temperature dependence of the TEP for Bi thin films with different thicknesses. The TEP of a 10,000 Å film (filled diamonds) is seen to be in good agreement with the previous single crystal values perpendicular to the trigonal axis reported by Gallo *et al.*<sup>7</sup> and Korenblit *et al.*<sup>41</sup> (open boxes). As the thickness of the Bi

film decreases, the TEP decreases. In the 600 Å and 200 Å thick films, the TEP changes sign from negative to positive at temperatures of 50 K and 200 K, respectively. In the 100 Å thick film, the TEP shows a positive value for the entire temperature range from 20 K to 300 K, which indicates a TEP dominated by holes. All films shown in Fig. 14 (closed symbol) have a 100 Å CdTe cap layer to prevent Bi oxidation. In order to confirm that the cap layer did not contribute appreciably to the observed TEP values, we measured the TEP of another 100 Å Bi film which did not have a cap layer. The cap-free film (open up-triangle) also shows hole-dominant behavior in the temperature range 20–300 K, with only a slightly lower absolute magnitude of the TEP above 200 K. The small difference in TEP is attributed to the presence of the second CdTe interface. The effect of CdTe interfaces on p-type doping and scattering is discussed later. We conclude that the p-type behavior of the thinner films is not directly related to the CdTe cap layers.

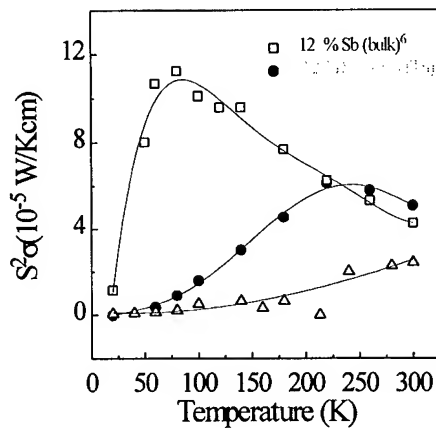


FIG. 13. Temperature dependence of the power factor ( $S^2/\rho$ ).

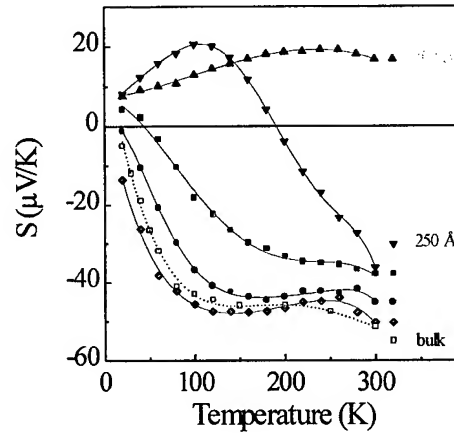


FIG. 14. The variation of the TEP as a function of temperature for Bi thin films of different thicknesses.

The thickness dependence of the TEPs of Bi thin films shown in Fig. 14 can be explained qualitatively as follows. For films of thickness comparable to or smaller than the de Broglie wavelength of the carriers, the quantum size effect dominates and the energy spectrum of the carriers breaks up into subbands which influences the transport properties. In Bi with its small effective mass ( $\sim 0.064 m_e$ ) the de Broglie wavelength is  $\sim 1000$  Å. The theoretical calculations in the form of thin films in the quantum size regime predict an enhanced value of the TEP as the film thickness decreases.<sup>6-12</sup>

Additionally, for a thermoelectric material containing both electrons and holes, the total TEP may be described with the relation given earlier:  $S = (\sigma_e S_e + \sigma_p S_p) / (\sigma_e + \sigma_p)$ . Chandrasekhar<sup>43</sup> and Gallo *et al.*<sup>7</sup> calculated the partial TEPs of Bi:  $S_e = -125.3 \mu\text{V/K}$  and  $S_p = 105.1 \mu\text{V/K}$  at 300 K, which for their model are independent of direction. In intrinsic bulk Bi, the density of electrons ( $n$ ) is the same as that of holes ( $p$ ), so the total TEP depends only on the mobilities of the carriers and partial TEPs. But in ultrathin films, the electron and hole densities tend to be different because of unintentional doping related to the heterostructure interfaces. As we discussed earlier,<sup>3-5</sup> magneto-transport measurements

on a series of ultrathin Bi films grown on CdTe substrates indicated heavy p-type doping: the low temperature hole concentrations varied as  $p = p_i + p_s/d$  where  $d$  is the film thickness,  $p_s = 8 \times 10^{12} \text{ cm}^{-2}$  and  $p_i \propto T^{3/2}$ , and the electron concentrations followed  $n \propto T^{3/2} \exp(-E_g/k_B T)$  where  $E_g = 0$  for  $d \geq 300 \text{ \AA}$  and  $E_g > 0$  for  $d \leq 300 \text{ \AA}$ . Therefore, the heavily p-type carrier concentration dominates, and the total TEP polarity becomes increasingly positive with decreasing film thickness and/or decreasing temperature. Possible causes of the p-type doping include: (i) acceptor like defects at the interface between the Bi and CdTe layer; (ii) Te vacancies in the CdTe buffer layer due to either the diffusion of Te vacancies from the substrate or non-stoichiometric growth of the buffer layer (resulting in p-type modulation doping of the Bi); (iii) the diffusion of Cd atoms into Bi from the CdTe as suggested by Tu.<sup>44</sup>

### A.3 Magneto-transport Measurement and QMSA Analysis

We first consider the Bi thin film, which is taken to be semimetallic with a 38 meV overlap between the conduction band minima at the L valleys and the valence band maximum at the T valley. In QMSA, the holes are therefore assumed to be isotropic, whereas a large mobility ratio of  $\mu_{i2} / \mu_{i1} = 60$  is employed for the anisotropic electrons residing in the L valleys.<sup>45,46</sup> QMSA results for the carrier densities and mobilities as a function of temperature are shown in Figs. 15 and 16, respectively. The concentration results are in good agreement with those of previous investigations of bulk Bi samples<sup>47</sup> and with the densities predicted by carrier-statistical calculations described elsewhere. At  $T = 6.3 \text{ K}$ , the electron mobility is found to be  $6.4 \times 10^4 \text{ cm}^2/\text{Vs}$  and the hole mobility is  $6600 \text{ cm}^2/\text{Vs}$ , whereas nearly equal electron and hole mobilities are obtained if the electrons are taken to be isotropic.<sup>48</sup>

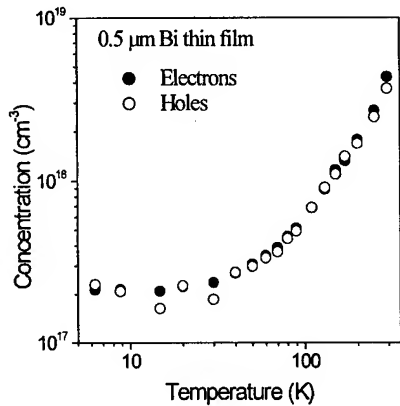


FIG. 15. Electron and hole densities as a function of temperature, as determined from analysis of the Hall data with the anisotropic QMSA procedure.

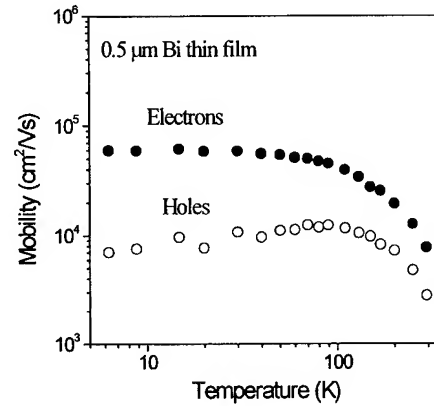


FIG. 16. Electron and hole mobilities as a function of temperature derived from the anisotropic QMSA of the Hall data.

In analyzing the transport data for the two  $\text{Bi}_{1-x}\text{Sb}_x$  samples ( $x = 0.09$  and  $0.16$ ), a larger mobility ratio of 250 was assumed.<sup>49</sup> The data were insufficiently sensitive for the QMSA procedure to be used with no constraining conditions. Therefore, we performed a standard multicarrier fit including anisotropy and assuming the presence of three carrier species: electrons in the  $L_a$  valley, holes in the T valley, and holes in the  $L_s$  valley. Results for the electron concentration (filled circles) and net hole concentration (both L and T

valleys, open circles) in this film are shown in Fig. 17. Corresponding fits for the electron mobility (filled circles), average hole mobility when the values for both hole species are allowed to float (open circles) and average hole mobility when  $\mu_{pT}$  is fixed at the value for Bi (open boxes) are given in Fig. 18. The two hole mobilities are seen to differ by a factor of 2-3. The curve in Fig. 17 is from a statistical calculation of the electron density, in which the electron and hole effective masses near the band edges have been adjusted from their literature values by a constant multiplicative factor of 1.2. This is done in order to fit the experimental room-temperature electron density of  $n = 1.7 \times 10^{18} \text{ cm}^{-3}$ , which is in good agreement with previous determinations. Note that the model then reproduces the experimental dependence  $n(T)$  quite well. For the temperature range of 60-100 K, in which thermally excited intrinsic carriers begin to appear, the agreement is slightly better by using a gap smaller than 12 meV, and somewhat worse when a larger indirect gap (e.g., 35 meV) is assumed.

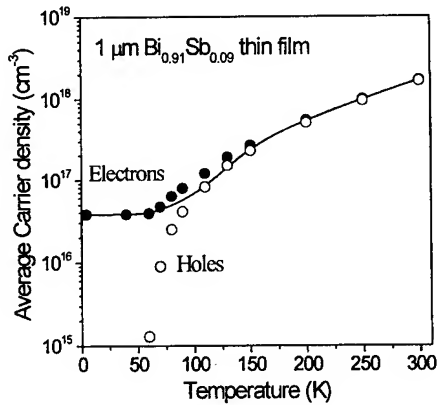


FIG. 17. Electron concentration (averaged over the total thickness) and net hole concentration from the multicarrier fit to the magnetotransport data. Also shown is the carrier-statistical calculation of the electron density obtained assuming a gap of 12 meV (curve).

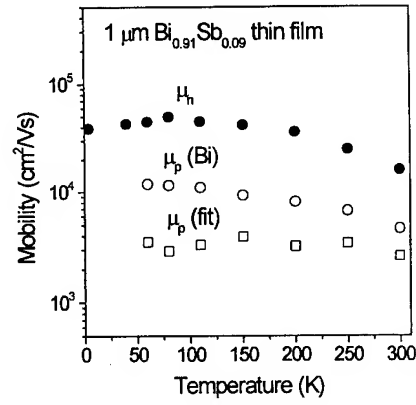


FIG. 18. Electron mobility (filled circles) and hole mobility, averaged over L and T-valley contributions, with floating mobilities for both species (open circles), and average hole mobility when the T-valley mobility is fixed at its value for Bi (open boxes) as a function of temperature.

#### A.4 Electronic Structure, Phase Stability and Semimetallic Behavior of Bi

The relativistic version of the FLMTO - plane wave method<sup>50</sup> is used to obtain self-consistent solutions of the Kohn-Sham-Dirac equations and the total energy. A 65 k-point mesh with the tetrahedron method in the irreducible part of the A7 Brillouin zone was used for the k-space integration. A three- $\kappa$  basis set (including 5d, 6s, 6p and 6d electron states) is used to construct the band Hamiltonian. An  $l_{max} = 6$  is used for the tail-decomposition and charge density calculations. Convergence to better than  $10^{-4} \text{ e/(a.u.)}^3$  for the charge density and  $10^{-5} \text{ Ry}$  for the total energy is achieved.

Bi belongs to the group-V elements with the  $\alpha$ -arsenic, A7, crystal structure. The A7 structure may be obtained from a simple cubic (SC) structure under two separate distortions: (i) an internal displacement of the two inter-penetrating fcc lattices (into which a SC structure can be resolved) along a (111) cube diagonal, and (ii) a trigonal shear. The electronic band structure of bulk Bi obtained with the experimental lattice

parameters<sup>51</sup> is shown in Fig. 19. (In a hexagonal basis  $a = 8.5678$  a.u., and  $c = 22.2958$  a.u., the trigonal shear angle  $\alpha = 57^\circ 19'$ , and the internal displacement  $u = 0.234$  (in units of the  $c$ -axis).)

The main features of the band structure consist of a hole pocket at the T-point and an electron pocket at the L-point, and are in agreement with both previous first-principles pseudopotential<sup>52</sup> and a variety of semi-empirical calculations.<sup>53</sup> As follows from Fig. 19, bulk Bi is a semimetal with a small conduction-valence band overlap involving the T and L points. The electron binding energies at  $\Gamma$  and T are compared with the data of XPS measurements and previous semi-empirical calculations. There is a reasonable agreement (rather qualitative) between our results and experiment. The lower energy of the valence band bottom obtained in most semi-empirical tight-binding calculations is due to the use of older experimental data for the parametrization of the Hamiltonian matrix elements. As follows from the results of our calculations and recent experiments,<sup>54</sup> the position of the valence band bottom measured in the earlier experiments is too low, and hence the semi-empirical results must be revised.

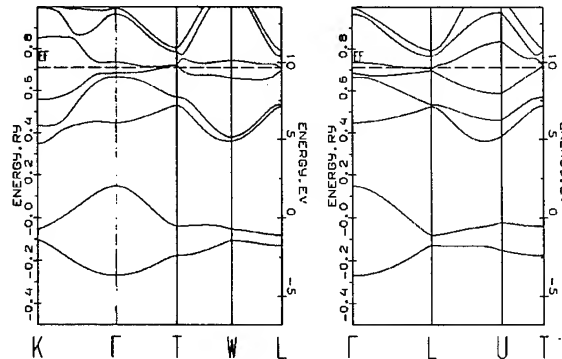


Fig. 19. Band structure of A7 - Bi for the experimental volume, internal displacement and trigonal shear.

The total energy as a function of the internal displacement ( $\delta = 0.25 - u$ ) for different volumes, but with the trigonal shear angle fixed at the experimental value, is shown in Fig. 20(a). The total energy clearly has a double-well character. A similar total energy dependence on the internal displacement was obtained previously for P and Sb within the framework of first-principles pseudopotential calculations.<sup>55</sup> The equilibrium value of the internal displacement decreases with decreasing volume and for  $V = 0.85 V_{exp}$  the dependence becomes practically flat. This shows that at high pressure an A7 to SC phase transition is expected, in agreement with experiment.<sup>56</sup> It should be mentioned that, as in the case of P and Sb, the dependence of the total energy on the internal displacement describes a second-order phase transition from A7 to SC in disagreement with the first-order phase transition observed experimentally. Therefore the mechanical work has to be added to the total energy to obtain a free energy at zero temperature and the first-order phase transition observed experimentally.

Using a Landau-type expansion of the total energy,  $\delta E = A\delta^2 + B\delta^4$ , we obtain an equilibrium internal displacement parameter  $\delta = 0.016$  which is in fairly good agreement with the experimental volume. The density of states at the Fermi-level as a function of

the internal displacement parameter is shown in Fig. 20(b). A decrease of the DOS with increasing  $\delta$  demonstrates the role of the internal displacement in the metal-semimetal transition. At some value of  $\delta$  larger than the equilibrium value an energy gap appears.

The total energy vs. unit cell volume dependence for the experimental value of the trigonal angle is shown in Fig. 21. There is an excellent agreement between the LDA and experiment. We also varied the angle around the experimental value and obtained  $E(60^\circ) - E(57^\circ 19') = 0.53$  meV and  $E(54^\circ) - E(57^\circ 19') = 39.44$  meV. Thus, we can conclude that the LDA provides the correct minimum of all three parameters for trigonal Bi: volume, trigonal angle, and internal displacement. To analyze the character of the metal-semimetal transition we performed calculations of Bi with the experimental Bi volume and (a) internal displacement  $u = 0.25$  and trigonal angle =  $60^\circ$  (which is an equivalent to the SC -structure); (b) an internal displacement  $u = 0.234$  and a trigonal angle =  $60^\circ$  (no trigonal shear); and (c) the actual trigonal structure of Bi.

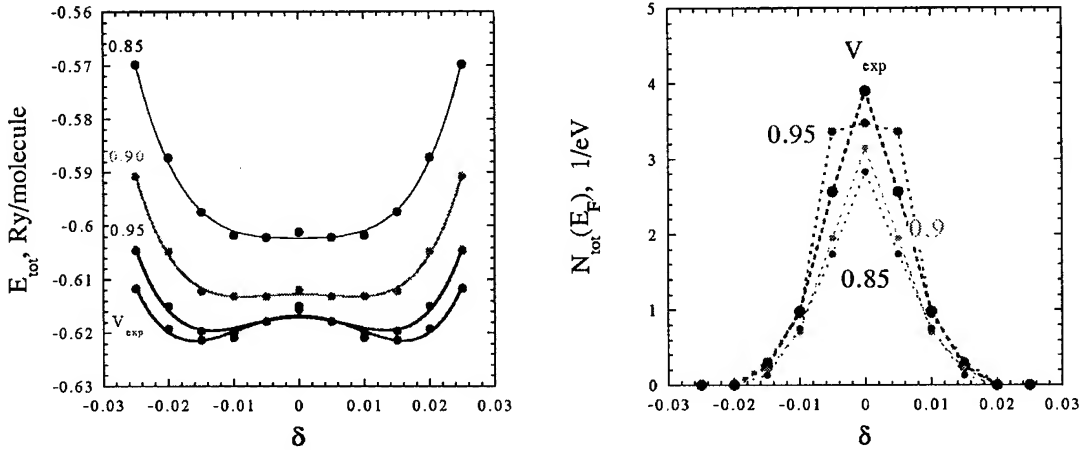


FIG. 20. (a) Total energy vs. internal displacement for different volumes. (b) Total DOS at  $E_F$  vs. internal displacement for different volumes (for experimental trigonal shear).

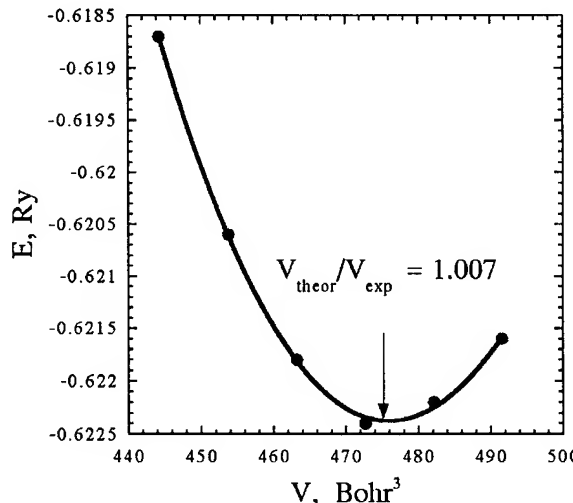


FIG. 21. Total energy vs. unit cell volume.

An "artificial" SC Bi (a) has a metallic ground state (Fig. 22(a)). The shift of one of the fcc sublattices along the (111) diagonal (Fig. 22(b)) (trigonal distortion) leads to the opening of a gap at L and T and is consistent with a splitting of the degenerate states near  $E_F$  for SC - Bi. Thus, Bi becomes a very narrow band gap semiconductor (a direct gap at T of 30 meV). The energy gain of this transition ( $E_B - E_A$ ) is calculated to be -66.4 meV; i.e., this transition lowers the total energy. Then, introducing a change in the trigonal angle from SC value of  $60^\circ$  to the experimental value, with the same volume and internal displacement as in the case (b) (cf. Fig. 22(c)), leads to a semimetal with a very small negative energy gain ( $E_C - E_B$ ) -0.53 meV. Thus, an internal displacement leads to a metal - insulator transition, which is qualitatively similar to a Jones-Peirels transition. The trigonal shear, however, drives a semiconductor-semimetal transition.

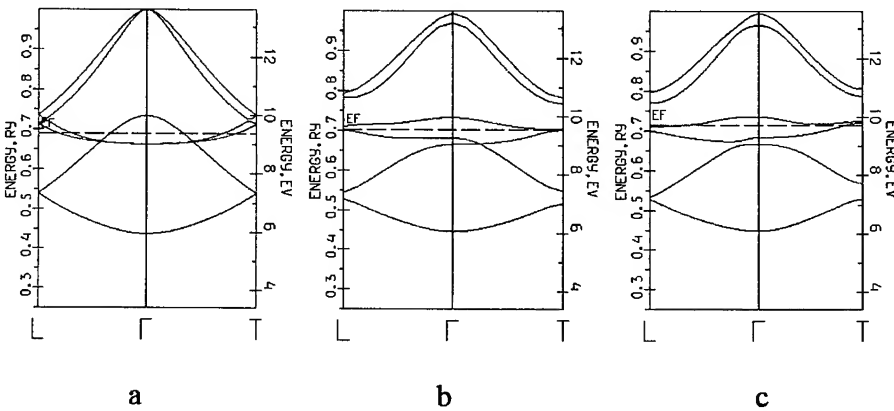


FIG. 22. The band structure along various symmetry lines: (a) for  $u = 0.25$  and  $\alpha = 60^\circ$  (note L and T are equivalent in this case); (b) for  $u = 0.234$  and  $\alpha = 60^\circ$ ; (c) for  $u = 0.234$  and  $\alpha = 57^\circ 19'$ .

As a model to analyze qualitatively the effect of a strain in the plane perpendicular to the c-axis on the electronic structure of Bi-films, we assume the following model of a strained film: we chose the lattice parameter  $a$  to be the same as for the assumed substrate (CdTe) and determine the  $c/a$  ratio in accordance with the experimental volume of Bi. We also choose the experimental value for the internal displacement. There is a decrease of the  $E_{Fe}$  and  $E_{Fh}$  overlaps with an increase of the "in-plane" lattice constant and trigonal angle. Finally, at  $\alpha = 60^\circ$ , Bi becomes a narrow-band semiconductor. This calculation suggests that the presence of tensile strain in our films grown on CdTe(111) leads to an increase in the rhombohedral angle, which drives the electronic band structure of BiSb toward semiconducting behavior as mentioned above. The appearance of semiconducting behavior in the 3.5 and 5.1% Sb alloys, the shift of the Sb concentration for the maximum bandgap, and the enhanced bandgap over bulk BiSb alloys are all consistent with a strain-altered band structure.

### A.5. Doped BiSb Alloy Thin Films

It has been reported that the electronic and transport properties of Bi and BiSb alloys are very sensitive to the presence of impurities. Group IV elements such as Pb and Sn were used as p-type dopants and the group VI element Te as an n-type dopant. Noothoven van Goor<sup>57</sup> reported that Te is a monovalent n-type dopant for Bi, based on the Hall effect. Heremans *et al.*<sup>58</sup> studied the Te-doping effect on Bi thin films grown on BaF<sub>2</sub> by molecular beam epitaxy (MBE). They demonstrated that Bi thin films could be n-type-doped with Te as a monovalent donor below a critical electron concentration of about  $5 \times 10^{19}$  cm<sup>-3</sup>. Brown *et al.*<sup>22</sup> reported the effect of Sn and Te doping on the bulk Bi<sub>0.88</sub>Sb<sub>0.12</sub> alloy for 20 ppm Te and 100 ppm Sn. They observed that for Sn-doped Bi<sub>0.88</sub>Sb<sub>0.12</sub>, the TEP changes from negative to positive around 30K with 100 ppm Sn. The thermogalvanomagnetic coefficients for Sn- and Te-doped semimetallic Bi<sub>0.95</sub>Sb<sub>0.05</sub> bulk crystals was reported by Jandl *et al.*<sup>59</sup> and Thomas *et al.*<sup>60</sup>, respectively. It is known that Sn and Te are monovalent dopants in the Bi, resulting in either lowering or raising the Fermi level.

We have performed systematic doping studies on Bi<sub>0.91</sub>Sb<sub>0.09</sub> alloy thin films by changing the Te and Sn dopant concentrations. The purpose of this study was to understand the doping behavior of extremely narrow bandgap Bi<sub>0.91</sub>Sb<sub>0.09</sub> alloys and to optimize the characteristics for use in a thermoelectric module.

#### (i) Te-doped Bi<sub>0.91</sub>Sb<sub>0.09</sub> Thin Films

Figure 23 shows the electrical resistivity of Te-doped Bi<sub>0.91</sub>Sb<sub>0.09</sub> thin films as a function of temperature with different doping amounts. The expression for the resistivity of an isotropic material with two types of carriers at zero magnetic field is  $\rho = (ne\mu + pev)^{-1}$ , where n and p are the densities of electrons and holes and  $\mu$  and v are their mobilities, respectively. We note that since Bi and BiSb alloys are highly anisotropic, the relevant mobilities represent an average over the angular orientation of the multiple valleys of the band extrema. The undoped sample shows typical semiconducting behavior in the electrical resistivity versus temperature. The 9% Sb concentration was chosen since that alloy shows the highest resistivity vs. temperature, arising from a maximal effective thermal bandgap of  $E_{g0} = 40$  meV determined by the temperature dependent electrical resistivity. For the undoped (intrinsic) sample the electron contribution to the conduction is dominant since the mobility of the electrons is an order of magnitude higher than that of the holes. The addition of the group VI Te donor to the semiconducting BiSb increases the Fermi level, effectively resulting in a one-carrier material. The electrical resistivity of the 480 ppm Te-doped sample increases from room temperature to 100 K. This behavior is caused by a freeze-out of mobile electrons. At 100 K the resistivity reaches a maximum of  $4 \times 10^{-4}$  Ohm-cm and thereafter decreases. Below 100 K, the resistivity decreases with decreasing temperature due to the enhanced mobility of the electrons. Highly Te-doped samples show a linear temperature dependence of the electrical conductivity, which is characteristic of a degenerate system.

We have measured the Hall coefficient ( $R_H$ ) and determined the effective number of carriers using the (isotropic) expression:  $R_H = (pv^2 - n\mu^2) / e(pv + n\mu)^2$ , which is appropriate in the limit of low magnetic fields. Figure 24 shows the effective carrier density of Te-doped BiSb thin films as a function of temperature. For the undoped (intrinsic) sample, the number of holes and electrons is equal ( $n = p$ ). The Hall

coefficient is dominated by the electrons due to their higher mobility. The behavior is typical of that for a semiconductor, satisfying  $n \propto T^{3/2} \exp(-E_g/k_B T)$ . The impurity concentration of the undoped sample is  $10^{17} \text{ cm}^{-3}$ . In the 480 ppm sample the number of electrons ( $8 \times 10^{19} \text{ cm}^{-3}$  at 300K) decreases with temperature until 150 K and thereafter saturates, representing a doping concentration ( $\sim 2 \times 10^{19} \text{ cm}^{-3}$ ). For the most heavily doped sample the number of electrons is constant with temperature, characteristic of degenerate behavior, at a value of  $\sim 5 \times 10^{20} \text{ cm}^{-3}$ . Table 1 shows the carrier concentration of Te-doped  $\text{Bi}_{0.91}\text{Sb}_{0.09}$  alloy thin films at 5K.

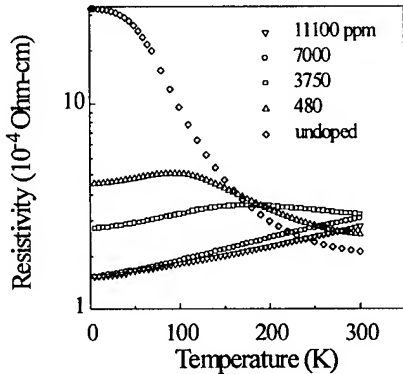


FIG. 23. Electrical resistivity of Te-doped 1  $\mu\text{m}$  thick  $\text{Bi}_{0.91}\text{Sb}_{0.09}$  thin films as a function of temperature.

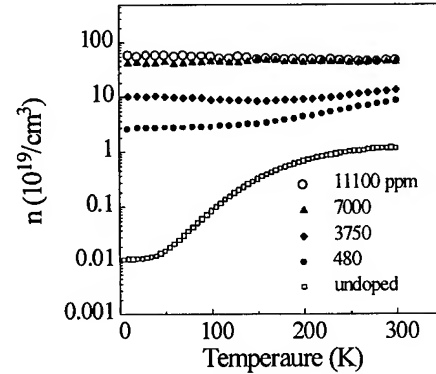


FIG. 24. The effective carrier density of Te-doped BiSb thin films as a function of temperature.

Figure 25 shows the TEP of Te-doped  $\text{Bi}_{0.91}\text{Sb}_{0.09}$  thin films as a function of temperature for different doping concentrations. As mentioned above, the undoped Bi-rich BiSb alloys show n-type behavior even for  $n = p$ , since the ratio of the mobility of electrons to holes is greater than one. The Fermi energy at 300 K is very close to the electronic band edge. In the high temperature regime, above some characteristic temperature, the magnitude of the TEP increases with decreasing temperature. This increase is due to the freeze-out of electrons and holes and an increase of the electron-to-hole mobility ratio with decreasing temperature. Below this characteristic temperature, the magnitude of the TEP decreases linearly with decreasing temperature as in bulk, due to the greater degeneracy of the carrier populations. Since the addition of donors into semiconducting BiSb alloys introduces additional n-type carriers, the TEP decreases due to an increased Fermi level. Highly Te-doped samples show a degenerate, linear temperature dependence of the TEP for all temperature up to 300K. Mott's expression<sup>29</sup> for the diffusion TEP in the degenerate free-electron approximation is

$$S = -\frac{\pi^2}{3} \frac{k_B^2 T}{e} \left[ \frac{d \ln \sigma(\varepsilon)}{d \varepsilon} \right]_{\varepsilon_F}, \quad (7)$$

where  $\varepsilon_F$  is the Fermi energy. In a pure metal, at temperatures for which electron-phonon scattering is dominant, the diffusion TEP is

$$S = \frac{\pi^2 k_B^2 T}{e \varepsilon_F}. \quad (8)$$

We can approximately calculate the electron Fermi energy using the above equation for the degenerate regime. We can determine the Fermi energy relative to the conduction band edge from the slope of the linear region of the TEP vs. temperature for the doped samples. The Fermi energy increases with increasing Te concentration. The calculated Fermi energies for the 7000 ppm and 11000 ppm-doped samples are 0.41 eV and 0.67 eV, respectively.

Figure 26 shows the TEP and electrical resistivity of Te-doped  $\text{Bi}_{0.91}\text{Sb}_{0.09}$  thin films as a function of the Te concentration at 300 K. Light n-doping increases the electrical resistivity, which is likely due to the decreased mobilities of electrons and holes. The magnitude of the TEP decreases with increasing Te concentration. Above 3750 ppm the electrical resistivity decreases and then saturates as the Te concentration increases. The decrease in the electrical resistivity for the heavily doped samples may arise because the increase in the electron density dominates the decrease in the electron mobility. In this regime the decrease in the magnitude of TEP is due to the increase in the Fermi energy.

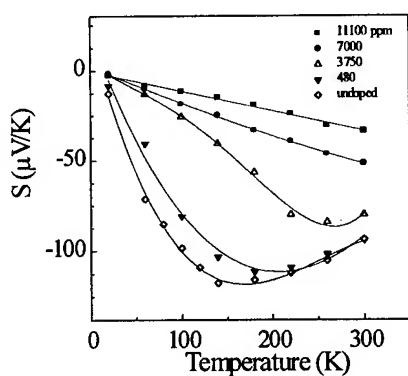


FIG. 25. TEP of Te-doped 1  $\mu\text{m}$  thick  $\text{Bi}_{0.91}\text{Sb}_{0.09}$  thin films as a function of temperature.

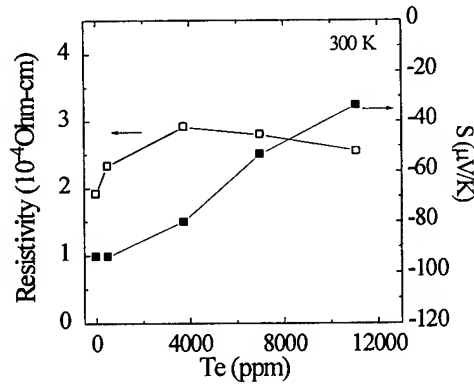


FIG. 26. TEPs and electrical resistivities of Te-doped 1  $\mu\text{m}$  thick  $\text{Bi}_{0.91}\text{Sb}_{0.09}$  thin films as a function of Te doping at 300 K.

## (ii) Sn-doped $\text{Bi}_{0.91}\text{Sb}_{0.09}$ Thin Films

Figure 27 shows the electrical resistivity of Sn-doped  $\text{Bi}_{0.91}\text{Sb}_{0.09}$  thin films as a function of temperature for different doping concentrations along with the undoped data. The group IV element Sn acts as an acceptor in the semiconducting BiSb alloys and lowers the Fermi level, effectively resulting in a one-carrier material. The electrical resistivity of the 720 ppm Sn-doped sample increases from room temperature down to 200 K, due to the freeze-out of mobile electrons. At 200 K the resistivity reaches a maximum of  $5 \times 10^{-4}$  Ohm-cm and thereafter the conduction is mainly due to holes. Below 200 K, the resistivity decreases with decreasing temperature because of the enhanced mobility of the holes. Highly Sn-doped samples show a linear temperature dependence of the electrical resistivity.

We have also measured the Hall coefficient ( $R_H$ ) and determined the effective number of carriers. The effective carrier density of Sn-doped BiSb films as a function of

temperature is shown in Fig. 28. In the 720 ppm sample the dominant carriers are electrons at room temperature but changes to holes at 230 K, which was also observed in the TEP results discussed in next section. It should be noted that Sn is a monovalent dopant in Bi and BiSb alloys. However, for our simple analysis of the Hall data, the number of holes is overestimated near the crossover to p-type because the mobility of the electrons is much higher.

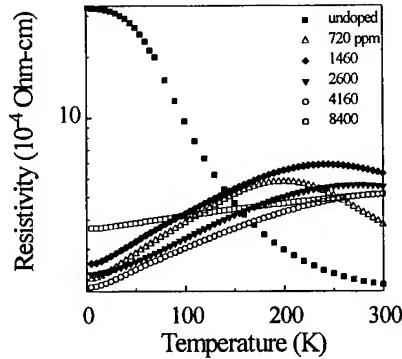


FIG. 27. Electrical resistivity of Sn-doped 1  $\mu$ m thick  $\text{Bi}_{0.91}\text{Sb}_{0.09}$  thin films as a function of temperature.

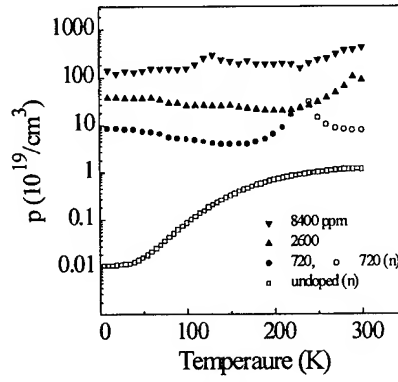


FIG. 28. The effective number of carriers of Sn-doped BiSb thin films as a function of temperature. In the 720 ppm Sn-doped sample, the carrier type changes from n to p type around 230 K.

The TEP of Sn-doped  $\text{Bi}_{0.91}\text{Sb}_{0.09}$  thin films as a function of temperature for different doping concentrations is shown in Fig. 29. Whereas the TEP of the undoped sample is negative at all temperature, the addition of acceptors changes the magnitude or sign of the TEP. For example, in the 720 ppm Sn-doped sample, the TEP is negative at room temperature due to intrinsic electrons, changes to positive at 230 K, peaks at 150 K, and thereafter decreases. With further Sn doping, the TEP becomes positive even at room temperature and the peak moves to higher temperature. The most heavily Sn-doped samples show a linear temperature dependence, which is also characteristic of degenerate behavior and is consistent with the electrical resistivity observations.

We determined the Fermi energy relative to the valence band edge using the same Mott expression (Eq. (8)) for the diffusion TEP in the degenerate limit. The Fermi energy decreases with increasing Sn concentration. The derived Fermi energies for the 4100 ppm and 8400 ppm-doped samples were -0.26 eV and -0.54 eV, respectively, where the minus sign signifies that the Fermi energy is below the valence band edge.

Figure 30 shows the TEP and electrical resistivity of the Sn-doped  $\text{Bi}_{0.91}\text{Sb}_{0.09}$  films as a function of Sn concentration at 300 K. Light p-doping increases the electrical resistivity, which is primarily due to the reduced density of high-mobility electrons. It can be seen that in this region the TEP changes polarity from negative to positive with increasing Sn concentration. The increase in the electrical resistivity continues until the conduction is governed by the low mobility holes. Above 1480 ppm the electrical resistivity decreases (due to the increase in the hole density dominating the decrease in the mobility) and then saturates as the Sn concentration increases. The polarity of the TEP at 300 K changes from positive to negative above 2600 ppm. At the highest doping levels the TEP decreases due to the decrease in the Fermi energy.

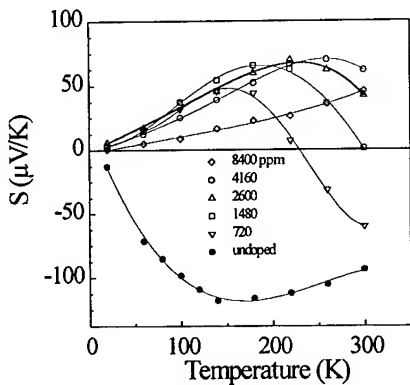


FIG. 29. TEP of Sn-doped 1  $\mu\text{m}$  thick  $\text{Bi}_{0.91}\text{Sb}_{0.09}$  thin films as a function of temperature.

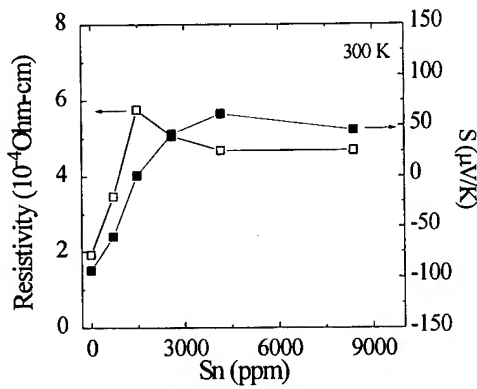


FIG. 30. TEPs and electrical resistivities of Sn-doped 1  $\mu\text{m}$  thick  $\text{Bi}_{0.91}\text{Sb}_{0.09}$  thin films as a function of Sn doping at 300 K.

Figure 31 shows the power factors ( $S^2\sigma$ ) as a function of temperature for p-type and undoped films, compared to the reported bulk value<sup>23</sup>. In 1  $\mu\text{m}$  thick  $\text{Bi}_{1-x}\text{Sb}_x$  alloy thin films on  $\text{CdTe}(111)\text{B}$ , we have observed several differences relative to the bulk system. The 3.5 and 5.1% Sb alloys (corresponding to semimetals in bulk) show semiconducting behavior. (As mentioned in Section II, the semiconducting behavior in bulk occurs at alloys compositions between 7 and 22% Sb with a maximum bandgap (18-20 meV) at  $x = 0.12\text{-}0.15$ .) The Sb concentration for the maximum bandgap shifts to a lower Sb concentration, from 12-15% in bulk to 9%. It is seen that the effective bandgaps of thin films grown on  $\text{CdTe}(111)$  are larger than the bulk values, with a maximum gap of 40 meV. Differences between thin films grown on  $\text{CdTe}(111)$  and bulk alloy may arise from the effects of strain. In addition, in BiSb alloy thin films grown on  $\text{CdTe}(111)$ , the Sb concentration with the largest power factor has also shifted to lower Sb concentration (7-9% Sb) and the power factor peaks at a significantly higher temperature (250K) than previously reported for the bulk alloy (80K). In Fig. 31, the largest bulk literature values (12 % Sb) are compared. For the Sn-doped p-type BiSb alloy films the absolute value of the power factor is an order of magnitude lower than for the n-type intrinsic material. This is due to the much lower mobility of the holes, relative to the electrons. In highly doped films the magnitude of the power factor decreases, due to the reduced mobility and reduced TEP caused by the higher degeneracy.

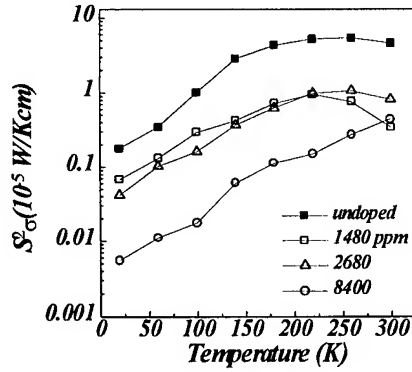


FIG. 31. Power factor ( $S^2\sigma$ ) of Sn-doped p-type and undoped n-type films.

## A.6. Magnetoresistance of Bi Films

Bismuth is well known for its small effective mass, small Fermi wavevector, and high mobility, which suggests that bismuth is a good material to study quantum size effects. Recently, a large magnetoresistance ratio, 1530, at 5 T and 5 K was reported for 10  $\mu\text{m}$  films prepared by electrodeposition.<sup>61,62</sup> However, the reported value for a bulk single crystal is much larger,  $4 \times 10^6$  at 5 T and liquid helium temperature.<sup>63</sup> This large magnetoresistance at low temperature is understood to be due to the curving of the carrier trajectories in a magnetic field by the Lorentz force. This so-called “ordinary” magnetoresistance is related to the quantity  $\omega_c\tau$  ( $= (eB/m^*c)\tau$ ), where  $\omega_c$  is cyclotron frequency and  $\tau$  is the relaxation time. In bismuth,  $\omega_c$  is large because of the small effective masses of the electrons. For this reason, bismuth has a large magnetoresistance.

### (i) Magnetoresistance of Bi Films Grown on CdTe

We grew 10  $\mu\text{m}$  thick Bi films on CdTe(111)B substrates by MBE. The growth rate was 1~2  $\text{\AA/s}$  as determined by a quartz thickness monitor. The observed temperature range for epitaxial growth of Bi on CdTe(111) was 80–210 °C; above and below this range of temperature, Bi grows polycrystalline. The growth temperature used was 150 °C. After the deposition, we annealed the sample at 268 °C for 6 hours in Ar. Note that the annealing temperature is 3° below the Bi melting point of 271 °C.

XRD studies have been performed on the as-deposited and annealed samples. In the  $\theta$ - $2\theta$  scan, only (00.l) peaks are observed (along with the substrate peaks), as shown in Fig. 32, which implies that Bi films grow in the trigonal axis normal to the CdTe(111) substrate. From the XRD rocking curve measurement, the full width at half maximum (FWHM) was determined to be 0.0647, which is near the instrument limit of our diffractometer, showing that the film is of high quality. After the annealing, the XRD pattern does not change much. This may be because the film was already highly crystalline before the annealing process and further improvement is limited by the instrument resolution.

The measured magnetoresistance of a 10  $\mu\text{m}$  thick Bi film is shown in Fig. 33. The film annealed for 6 hours at 268 °C shows a large magnetoresistance ratio, 2700 at 5 K and 5 T, and 3.9 at 300 K and 5 T. This is a large increase compared with that for an unannealed film, which was 340 at 5 K and 5 T. The magnetic field dependence of the magnetoresistance shows a linear behavior, except in the low magnetic field region.

The temperature dependence of the magnetoresistance of the annealed Bi is shown in Fig. 34 on a linear scale and in Fig. 35 on a logarithmic scale. The magnetoresistance increases with decreasing temperature while the zero-field resistance decreases linearly with decreasing temperature. The magnetoresistance at 5 T increased about 2 orders of magnitude from 300 K to 5 K and the zero-field resistance decreased about 1 order of magnitude with the same temperature decrease.

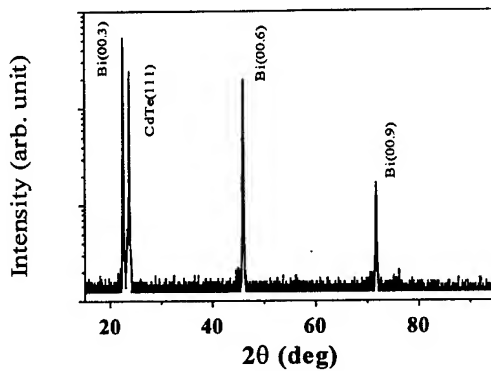


FIG. 32. XRD  $\theta$ - $2\theta$  scan of a 10  $\mu\text{m}$  Bi film on CdTe (111)B.

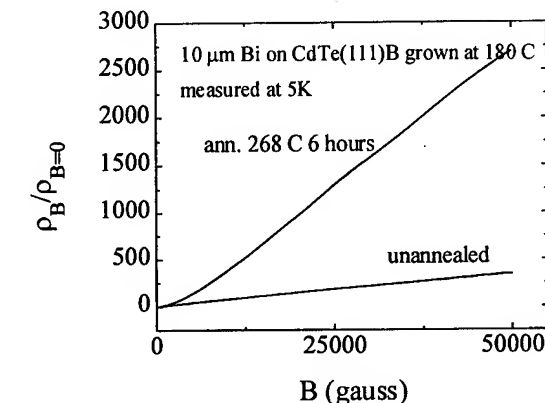


FIG. 33. Magnetoresistance ratio of a Bi film as-deposited and after annealing.

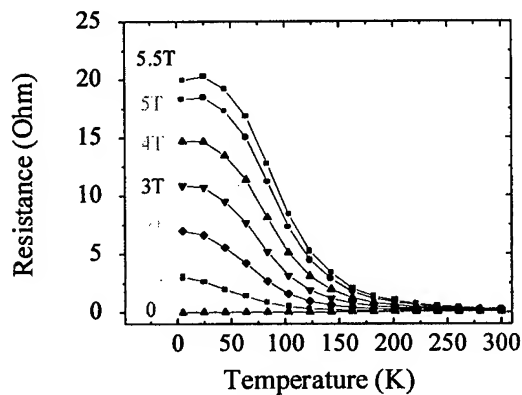


FIG. 34. Temperature dependent magnetoresistance of the annealed Bi film on a linear scale.

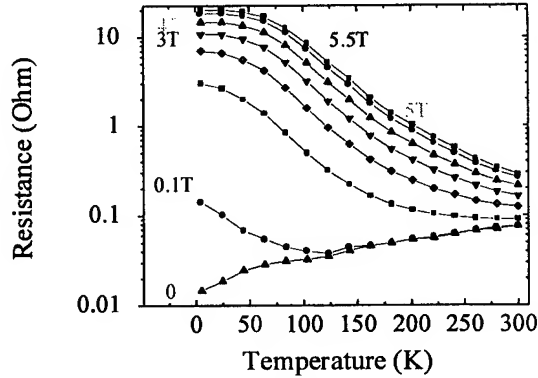


FIG. 35. Temperature dependent magnetoresistance of the annealed Bi film on a logarithmic scale.

The annealed Bi film showed Shubnikov-de Hass oscillations, as shown in Fig. 36, indicating that it is of high quality; we did not find oscillations in unannealed films. The period of the oscillation was  $\sim 0.18 \text{ T}^{-1}$ , which is in a good agreement with the bulk value with the magnetic field applied along the trigonal axis.<sup>64</sup>

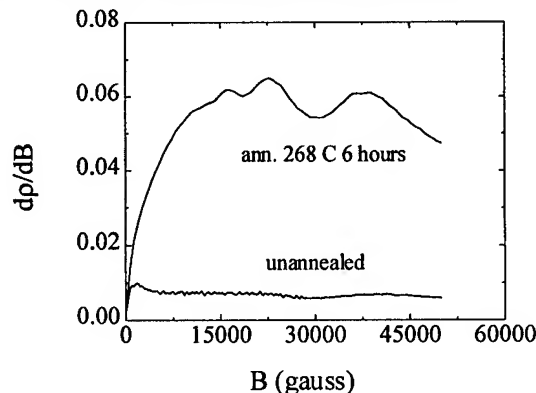


FIG. 36 Shubnikov-de Hass oscillations observed in the annealed Bi film.

In order to explain this large change in the magnetoresistance produced by annealing, we performed a field-dependent Hall analysis, which can yield information on all carrier species present. The mobilities and carrier concentrations of the annealed sample are plotted in Fig. 37. The electron mobility is  $\sim 1 \times 10^6 \text{ cm}^2/\text{Vs}$  at 4 K, and the hole mobility is  $\sim 3 \times 10^5 \text{ cm}^2/\text{Vs}$  at 4 K. The carrier concentrations for electrons and holes are almost the same,  $3 \times 10^{17} \text{ cm}^{-3}$ . The mobilities for the unannealed samples are more than 1 order of magnitude lower, as shown in Fig. 38. At 4 K, the electron mobility is  $\sim 7 \times 10^4 \text{ cm}^2/\text{Vs}$  and the hole mobility is  $\sim 7 \times 10^3 \text{ cm}^2/\text{Vs}$ , respectively.

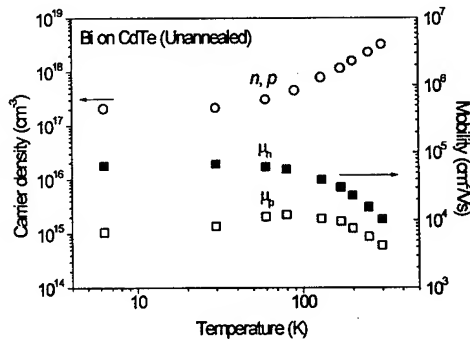


FIG. 37 Electron and hole mobilities and carrier concentrations of the annealed Bi thin film.

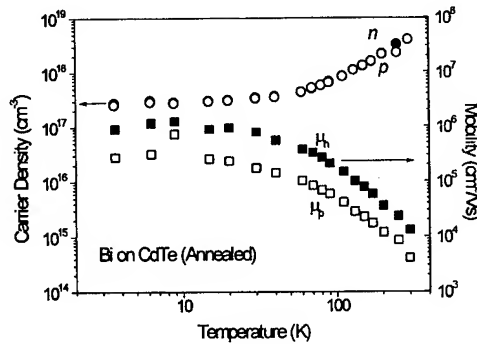


FIG. 38 Electron and hole mobilities and carrier concentrations of the unannealed Bi thin film.

In summary, post-annealing of 10  $\mu\text{m}$  thick Bi films grown by MBE results in a large increase in the magnetoresistance ratio from 34,000 % to 270,000 % at 5 K and 4 T. This implies that post annealing may be one strategy to improve the quality of films when limitations on the deposition temperature required for epitaxial growth do not result in a high quality of film. The large magnetoresistance ratio of annealed bismuth films can be ascribed to higher mobility relative to that in an unannealed film.

### (ii) Magnetoresistance of Bi Films Grown on PbTe/CdTe

In order to investigate the influence of a buffer layer on the properties of Bi films which were subsequently annealed, 200  $\text{\AA}$  PbTe buffer layers were grown on CdTe(111) using MBE, followed by the growth of 10  $\mu\text{m}$  of Bi. The in-plane lattice mismatch between PbTe and CdTe(111) is 0.7 %, and that between Bi and PbTe is less than 0.1%, respectively. The growth temperature was 180  $^{\circ}\text{C}$ . After the deposition, we annealed the samples at 268  $^{\circ}\text{C}$  for 1, 4, and 12 hours in Ar. The 12 hour annealed sample seemed to melt at the sample edge.

XRD studies were performed on the as-deposited and annealed samples. In the  $\theta$ - $2\theta$  scan, only  $(00.l)$  peaks of Bi are seen, which implies that the Bi films grow with the trigonal axis normal to the PbTe/CdTe(111). After the annealing, the XRD pattern does not change significantly, as observed for growth on CdTe. The measured magnetoresistance is shown in Fig. 39. The magnetoresistance ratio for the 1 hour annealed sample increased to 260 at 5 K and 5 T, compared with 175 for the as-deposited sample. However, after that point, as the annealing time increases, the magnetoresistance ratio decreases. This may be due to diffusion from the buffer. As the annealing

proceeds, the crystallinity of the sample is improved, but after it reaches a certain point, diffusion from the buffer overcomes any further improvement from annealing and eventually degrades the electrical properties of the sample. From the fact that Bi on PbTe/CdTe seems to melt at the annealing temperature, 258 °C, whereas Bi on CdTe does not, we conclude that there is larger reaction between Bi and PbTe than between Bi than CdTe.

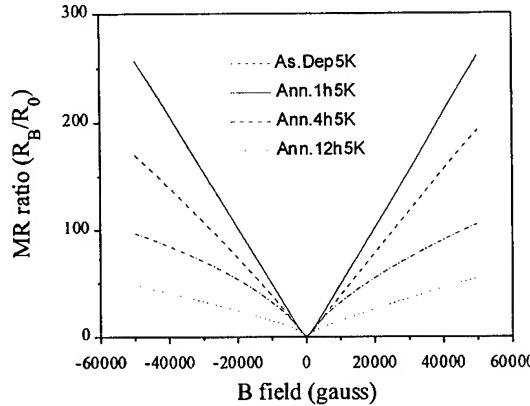


FIG. 39 Magnetoresistance ratio of as-deposited and 1, 4, 12 hours annealed Bi films on PbTe/CdTe(111).

### (iii) Magnetoresistance of Bi Films Grown on Mica

Mica has been used to grow Bi films for a long time.<sup>1,65</sup> It is not quite a perfect single crystal, but it is well known that Bi films grow epitaxially on mica with the film normal to the trigonal axis after several hundred angstrom.<sup>66</sup> In this experiment, commercially cleaved mica substrates were used. MBE was used to grow 10 μm thick Bi films. The growth temperature was 130-200 °C. After the deposition, we annealed the sample at 268 °C for 1, 4, 8, 16 hours in Ar.

XRD studies were performed on the as-deposited and annealed film samples. In a θ-2θ scan of a film deposited at 130 °C, the (01.2) peak and its harmonics as well as the (00.l) peaks are seen, as shown in Fig. 40, which implies that both (00.1) oriented and (01.2) oriented Bi grains have grown on the mica substrate. After one hour annealing at 268 °C, the XRD pattern changes significantly. The intensity of the (00.l) peaks increased and that of the (01.2) peaks decreased. The rocking curve for the (01.2) peak became broader for the annealed sample, while the curve for the (00.3) peak changed from broad to sharp (FWHM: ~0.18° for the annealed sample). Because the substrate is not rigid, the FWHM is not accurately determined but the trend that the intensity of the (00.l) peaks get larger with the annealing time is clear.

The measured magnetoresistance of 10 μm thick Bi films on mica is shown in Fig. 41. The 268 °C 8 hours annealed Bi film shows a drastic increase in the magnetoresistance ratio, 3300 at 5 K and 5 T compared with the ratio 400 for the unannealed one. The SdH oscillation is apparent, without any background manipulation, from the plot of the magnetic field dependent magnetoresistance curve for the annealed film.

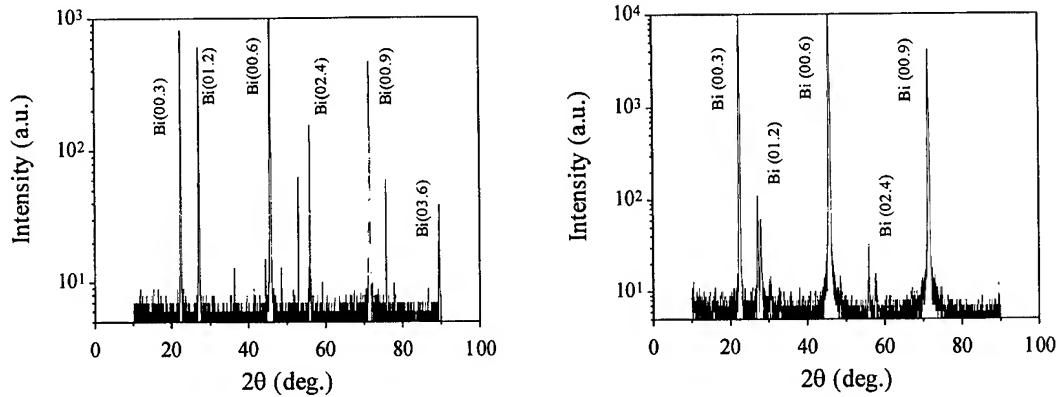


FIG. 40 XRD  $\theta$ - $2\theta$  scans of a  $10 \mu\text{m}$  Bi film on mica (a) as-deposited and (b) after 1 hour annealing.

In order to obtain more complete transport data, the 4, 8, 16 hours annealed samples were processed into bar patterns using the photolithography and lift-off techniques. The magnetoresistance of the samples is shown in Fig.'s 42(a) and (b). The SdH oscillation is apparent for the patterned 8 hours annealed sample, as shown in Fig. 42. The magnetoresistance ratio increases to 12000 for the patterned 8 hours annealed sample from 5000 for the patterned 4 hours annealed sample. Then, the ratio decreases down to 3000 for the patterned 16 hours annealed sample. This may be due to diffusion from the substrate, as in the case of Bi films on CdTe or PbTe/CdTe. The patterned 8 hours annealed sample shows the highest value of the magnetoresistance ratio, 12000. This is a quite strange result because, before the patterning, the same sample showed a lower value (3300). This may be due to a contribution from the “geometric” magnetoresistance as well as the “physical” magnetoresistance. (There has been a report on enhanced geometric magnetoresistance produced by Au inhomogeneities in the InSb system, even at room temperature.<sup>67</sup>) Or, the quality of the film may be different depending on the position in the sample. (The edge of mica substrate is not clean and the substrate is easy to be bent.) Magnetoresistance curves for the patterned samples are plotted on a logarithmic scale in Fig. 42(b). At 300 K, the curves do not show a large difference with respect to the annealing time.

The zero-field resistivity of the unpatterned (but scaled with a known bulk value at room temperature) as-deposited and 8 hours annealed  $10 \mu\text{m}$  Bi films, and the patterned 4, 8, 16 hour annealed films on mica is shown in Fig. 43. It is clear that the annealed samples show a linear, monotonically decreasing, resistivity behavior with decreasing temperature but that the as-deposited sample does not show much change in the zero-field resistivity with temperature. In the patterned 8 hour annealed sample, the resistivity decreases with temperature, by one order from 300K to 5 K.

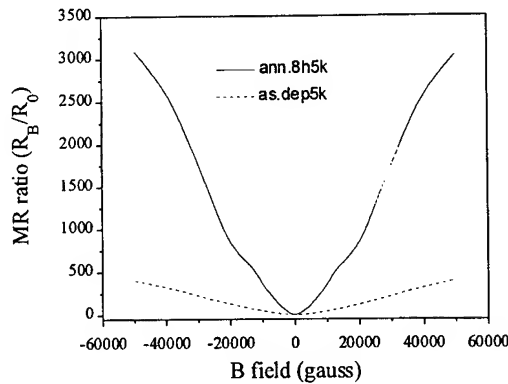


FIG. 41 Magnetoresistance curves of a 10  $\mu\text{m}$  Bi film on mica as-deposited and after 8 hours annealing.

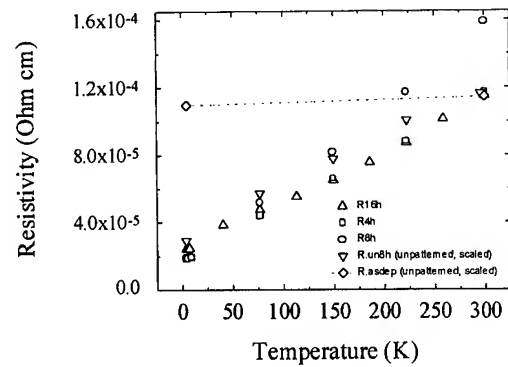


FIG. 43 Zero field resistivity of the unpatterned as-deposited and 8 hour annealed 10  $\mu\text{m}$  Bi films and the patterned 4, 8, 16 hour annealed films on mica.

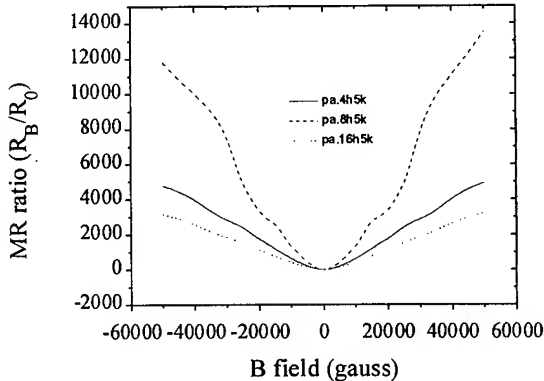


FIG. 42 Magnetoresistance curves of the patterned 4, 8, 16 hour annealed 10  $\mu\text{m}$  Bi films on mica.

The 8 hours annealed Bi films showed very apparent Shubnikov-de Hass oscillations, even without any background subtraction from the data, indicating that the film is of high quality. The electron and hole mobilities of the sample are  $2\sim3\times10^6$   $\text{cm}^2/\text{Vs}$  at low temperature, and  $3\sim4\times10^5$   $\text{cm}^2/\text{Vs}$ , respectively, from the field dependent Hall analysis. The electron mobility of this sample is the largest among all our samples.

In summary, post-annealing of 10  $\mu\text{m}$  thick Bi films on mica makes a large increase in magnetoresistance ratio to  $\sim 12000$  at 5 K and 4 T for a patterned sample. This implies that Bi may be less reactive with mica than CdTe or PbTe during the annealing process. The combination of the largest mobility and largest magnetoresistance ratio for this sample confirms that the mobility is the key parameter for achieving large magnetoresistance ratios.

### A.7. Anisotropy of Bi and BiSb Alloy Thin Films

The rhombohedral crystal structure of Bi, BiSb, and  $\text{Bi}_2\text{Te}_3$  leads to anisotropic electronic properties. A consequence is that the thermoelectric performance is optimal for heat flow along specific crystal directions. For example,  $\text{Bi}_2\text{Te}_3$  has a higher  $Z$  value in the plane perpendicular to the trigonal axis, while Bi and BiSb have higher  $Z$  values along the trigonal axis. However, the preferred growth direction for all three materials is along the trigonal axes,<sup>68,69</sup> which for Bi and BiSb alloys favors vertical cooling while for  $\text{Bi}_2\text{Te}_3$  it favors in-plane cooling. For in-plane Bi and BiSb as well as out-of-plane  $\text{Bi}_2\text{Te}_3$  devices, it would be preferable to reorient the films for optimum performance according to their anisotropies. In this section, anisotropy in Bi and BiSb alloy films is examined in order to enhance the performance by changing the crystal orientation. In particular, we describe approaches to reorient films for optimum performance according to their anisotropies for the cases of both in-plane and vertical cooling devices.

In order to investigate the influence of substrate orientation on the thermoelectric properties, we grew Bi and BiSb films on CdTe(211) substrates where the (00.1) axis is tilted 19° from the substrate normal. The in-plane Seebeck coefficient for these films is found to be anisotropic. Magneto-Seebeck studies employing fields of up to 0.7 T show a strong dependence of the Seebeck coefficient on both crystal-axis and magnetic field direction.

Bi and  $\text{Bi}_{0.92}\text{Sb}_{0.08}$  alloy thin films were grown by molecular beam epitaxy (MBE) on semi-insulating CdTe(211) substrates. All epilayers were grown to a nominal thickness of 1  $\mu\text{m}$ . The magneto-Seebeck effect was studied for magnetic fields of  $B = 0 - 0.7$  T aligned perpendicular to the (in-plane) thermal gradient.

Figure 44(a) shows a schematic of the Bi or BiSb grown on (211)CdTe, where the growth along (00.1) is tilted by 19° from the substrate normal. For the Seebeck coefficient measurements, we cut the sample along the two directions shown in Fig. 44(b): (1) the CdTe[ $\bar{1}11$ ] substrate direction, which contains a trigonal component of the film, and (2) the CdTe[ $01\bar{1}$ ] substrate direction, which does not. The width of the samples was 1 mm.

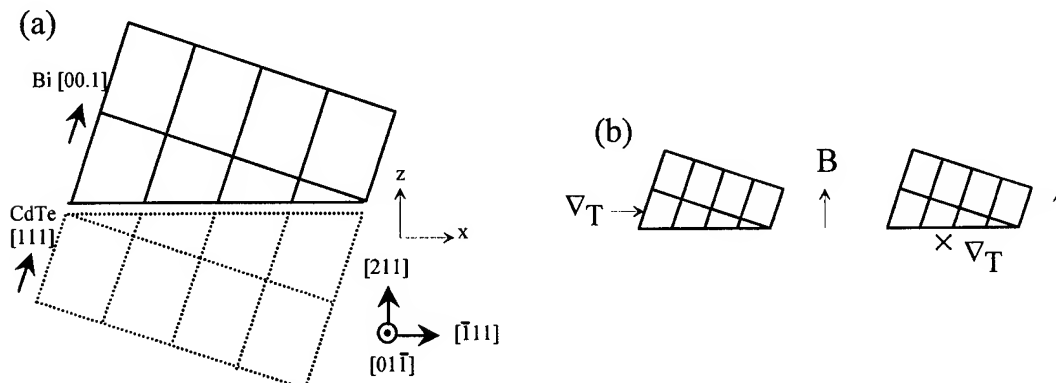


FIG. 44 (a) Schematic side-view of Bi or BiSb film growth on (211)CdTe. (b) Configurations for the Seebeck and magneto-Seebeck measurements.

#### (i) Seebeck and Magneto-Seebeck Coefficients for Bi

Figure 45 shows the Seebeck coefficients for Bi thin films along the  $[\bar{1}11]$ CdTe substrate direction and along the  $[01\bar{1}]$  direction in zero magnetic field. For both directions, the Seebeck coefficients are negative because the electron mobilities are higher than the hole mobilities. The anisotropy of the Seebeck coefficient is apparent, since the magnitude is somewhat higher for the thermal gradient  $\vec{\nabla}T$  parallel to the  $[\bar{1}11]$  direction than when it is parallel to the  $[01\bar{1}]$  direction.

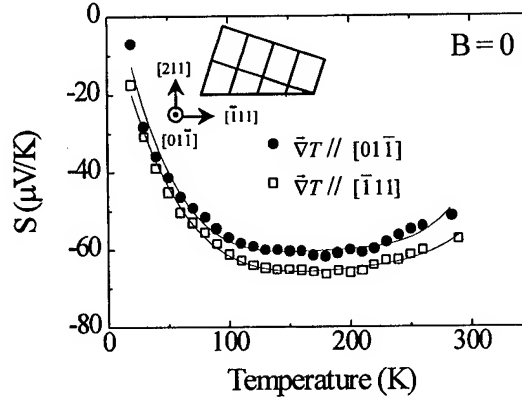


FIG. 45 Temperature-dependent Seebeck coefficients for Bi thin films with  $\vec{\nabla}T$  along the  $[\bar{1}11]$  and  $[01\bar{1}]$  directions in zero magnetic field.

The thermoelectric voltage due to the Seebeck effect is given by  $\vec{V} = \vec{S}\vec{\nabla}T$ , where  $\vec{S}$  is the Seebeck tensor. With the coordinate system defined as in Fig. 44 (*i.e.*,  $x$  is along the CdTe $[\bar{1}11]$  direction and  $y$  is along the CdTe $[01\bar{1}]$  direction), and with  $\vec{\nabla}T$  parallel to  $[\bar{1}11]$ , the Seebeck tensor has the form<sup>70</sup>

$$S = \begin{pmatrix} S_{11} & 0 & S_{13} \\ 0 & S_{22} & 0 \\ S_{31} & 0 & S_{33} \end{pmatrix}. \quad (9)$$

Here

$$\begin{aligned} S_{11} &= S_{ab}\cos^2\alpha + S_c\sin^2\alpha \\ S_{22} &= S_{ab} \\ S_{33} &= S_{ab}\sin^2\alpha + S_c\cos^2\alpha \\ S_{13} &= S_{31} = \frac{1}{2}(\sin 2\alpha)(S_{ab} - S_c), \end{aligned}$$

and  $\alpha$  is the tilt angle between the crystal c-axis (trigonal) and the substrate normal. In this notation,  $S_{11}$  and  $S_{22}$  are the Seebeck coefficients for the thermal gradient  $\vec{\nabla}T$  parallel to the  $[\bar{1}11]$  and  $[01\bar{1}]$  directions, respectively.  $S_c$  and  $S_{ab}$  are the coefficients along the crystal c-axis (the trigonal axis) and within the ab-plane, respectively. In bulk Bi at room temperature,  $S_c = -102 \mu\text{V/K}$  and  $S_{ab} = -51.4 \mu\text{V/K}$ .<sup>71</sup> Thus, for  $\alpha = 19^\circ$ , the above equation gives  $S_{11} = -56.8 \mu\text{V/K}$ , which is close to our measured value of  $-57.4 \mu\text{V/K}$ . Our measured value of  $S_{22}$  is  $-51.4 \mu\text{V/K}$ , which is in good agreement with the known bulk value  $S_{22} = S_{ab} = -51.4 \mu\text{V/K}$ .

Figure 46(a) shows the temperature dependence of the magneto-Seebeck coefficients for Bi films measured for  $\vec{\nabla}T \parallel [\bar{1}11]$  direction, for both positive and negative magnetic fields oriented along the CdTe[211] axis normal to the substrate (see Fig. 44(b)). The Seebeck coefficients as a function of magnetic field  $B$  at the constant temperatures of 160 and 290 K are shown in Fig. 46(b). At those temperatures, the magneto-Seebeck coefficients for both negative and positive fields are seen to increase monotonically with  $B$  up to our highest field of 0.7 T. The data also show that the Seebeck coefficient depends strongly on field direction, with the magnitudes for positive  $B$  being higher than those for negative  $B$  over the entire temperature range from 20 to 300 K. The largest increase in the field-dependent Seebeck coefficient occurs around 160 K.

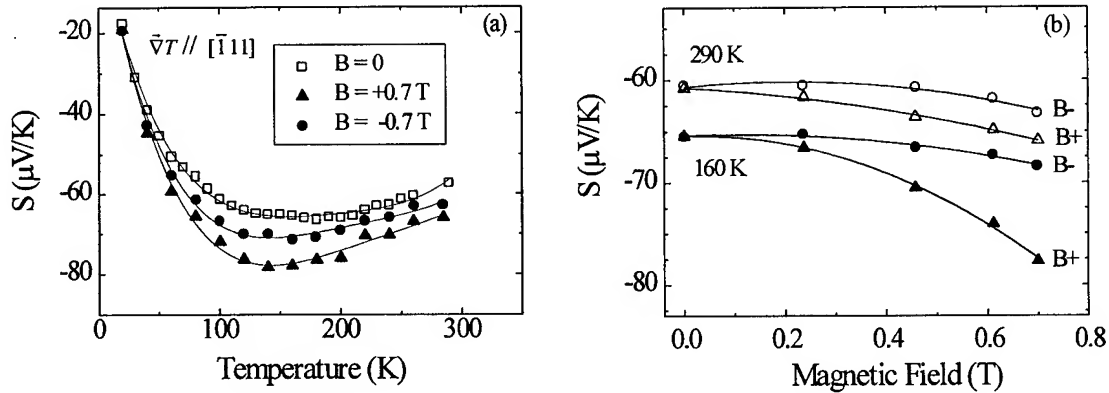


FIG. 46 (a) Magneto-Seebeck coefficients along  $[\bar{1}11]$  for Bi thin films, in a positive and negative 0.7 T magnetic field oriented along [211] (normal to the substrate). (b) Magnetic field-dependent Seebeck coefficients at 160 and 290 K.

Similar results are shown in Fig.'s 47(a) and (b) for the sample cut with  $\vec{\nabla}T \parallel [01\bar{1}]$ . The primary difference between these results and those for  $[\bar{1}11]$  is that the data in Fig. 46 for  $[\bar{1}11]$ , which contains a Bi [00.1] component, show a higher slope than the  $[01\bar{1}]$  data in Fig. 47.

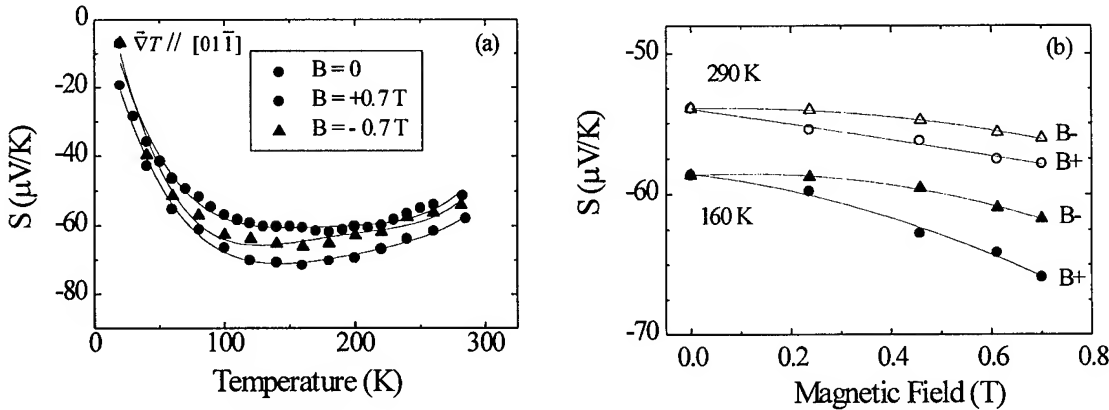


FIG. 47 (a) Magneto-Seebeck coefficients along  $[01\bar{1}]$  for Bi thin films with the same field geometry as in Fig. 46. (b) Magnetic field-dependent Seebeck coefficients at 160 and 290 K.

The large magneto-Seebeck coefficients are caused by the strong thermomagnetic (Nernst and Ettingshausen) effect in the Bi system, *i.e.* they result from the substantial transverse currents induced by equal numbers of high-mobility electrons and holes in the plane normal to the magnetic field.<sup>72</sup> The electrical resistivity also showed a slight anisotropy for directions between the  $[\bar{1}11]$  and  $[01\bar{1}]$  axes:  $(1.28 \text{ vs. } 1.14) \times 10^{-4} \Omega\text{-cm}$ , respectively, at room temperature in zero magnetic field.

### (ii) Seebeck and Magneto-Seebeck Coefficients for $\text{Bi}_{0.92}\text{Sb}_{0.08}$

We performed similar experiments on  $\text{Bi}_{0.92}\text{Sb}_{0.08}$  alloy samples, which have the same rhombohedral crystal structure. Figure 48 shows the Seebeck coefficients along the  $[\bar{1}11]$  and  $[01\bar{1}]$  directions in zero magnetic field, which are again negative due to the higher electron mobility. The anisotropy is also apparent, and is stronger than in the pure Bi (Fig. 45). In bulk  $\text{Bi}_{0.92}\text{Sb}_{0.08}$  at room temperature,  $S_c = -102 \mu\text{V/K}$  and  $S_{ab} = -85 \mu\text{V/K}$ .<sup>72</sup> Thus, for  $\alpha = 19^\circ$ , Eq. (9) gives  $S_{11} = -86.8 \mu\text{V/K}$ , which compares with our measured value of  $-89.9 \mu\text{V/K}$ . For the  $[01\bar{1}]$  direction,  $S_{22} = S_{ab} = -85 \mu\text{V/K}$  is predicted vs. the measured value of  $-79 \mu\text{V/K}$ .

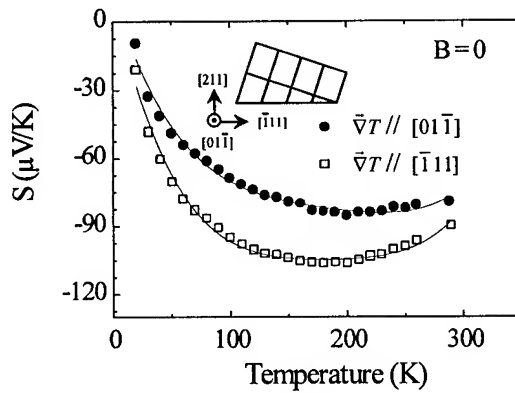


FIG. 48 Temperature-dependent Seebeck coefficients for  $\text{Bi}_{0.92}\text{Sb}_{0.08}$  thin films with  $\vec{\nabla}T$  along the  $[\bar{1}11]$  and  $[01\bar{1}]$  directions in zero magnetic field.

Figure 49(a) shows the temperature-dependent magneto-Seebeck coefficients for BiSb films measured along the  $[\bar{1}11]$  direction at  $B = \pm 0.7 \text{ T}$ . The dependences of the Seebeck coefficients on magnetic field at  $T = 160$  and  $290 \text{ K}$  are shown in Fig. 49(b). The enhancement with magnetic field is seen to be tiny up to  $0.7 \text{ T}$ , and the dependence on field direction is small at both  $160\text{K}$  and  $290\text{K}$ . For the sample cut along  $[01\bar{1}]$ , the results are shown in Fig. 50(a) and (b). Again, there is a slight increase of the Seebeck coefficient with magnetic field and a small dependence on field direction. In contrast to the Bi case, the rate of increase is higher along  $[01\bar{1}]$  than along  $[\bar{1}11]$ . Compared to Bi, BiSb showed a small magneto-Seebeck effect and a still smaller dependence on the field direction.

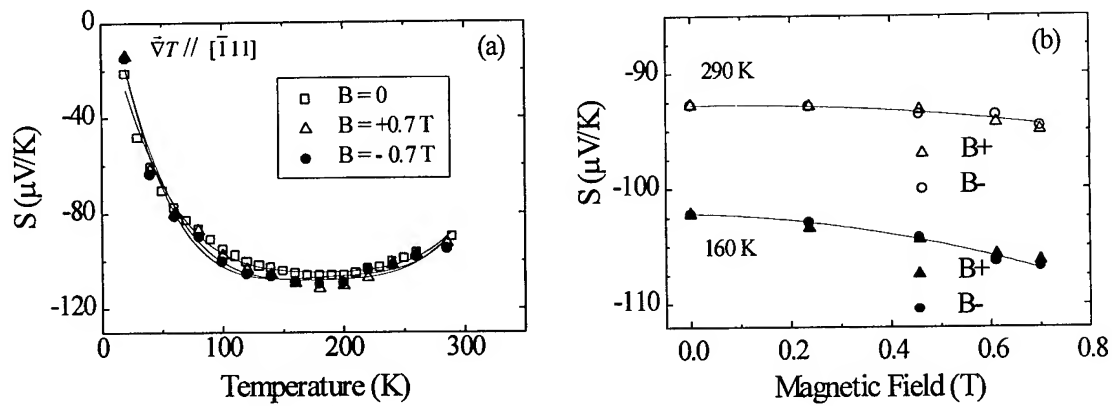


FIG. 49 (a) Magneto-Seebeck coefficients along  $[\bar{1}11]$  for BiSb thin films for positive and negative magnetic fields of  $0.7\text{ T}$ . (b) Magnetic field-dependent Seebeck coefficients at  $160$  and  $290\text{ K}$ .

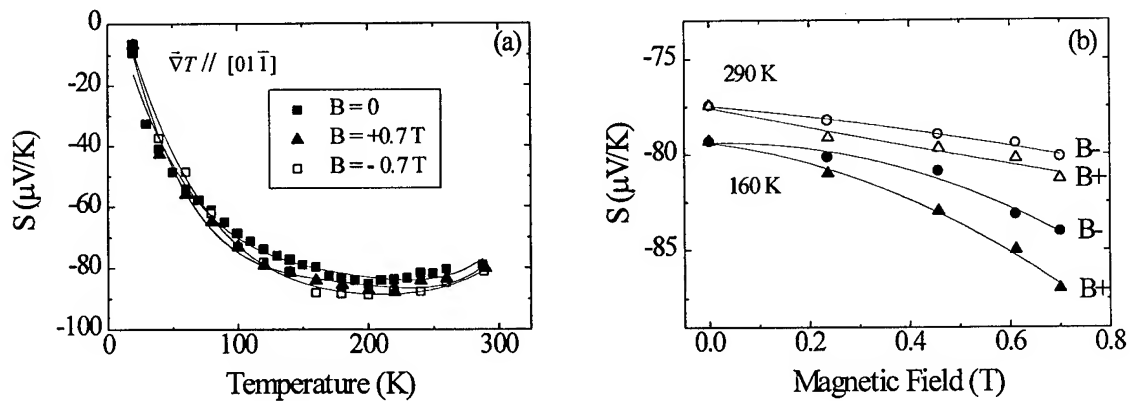


FIG. 50 (a) Magneto-Seebeck coefficients along  $[01\bar{1}]$  for BiSb thin films for positive and negative magnetic fields of  $0.7\text{ T}$ . (b) Magnetic field-dependent Seebeck coefficients at  $160$  and  $290\text{ K}$ .

Variation of the transport properties with magnetic field direction are a relatively unusual phenomenon, which here are related to the incline of the constant energy surfaces with respect to the field axis. Such a dependence of the Seebeck coefficient on magnetic field is known as the “umkehr” effect,<sup>73</sup> which arises from the strong thermomagnetic effects in Bi and BiSb. The Umkehr effect, as well as the large magneto-Seebeck coefficients, result from the large transverse currents that are induced by the equal numbers of high-mobility electrons and holes.<sup>72,73</sup> If the principal axes of the various constant energy surfaces are inclined with respect to the field axis, these transverse currents do not strictly reverse their direction when the magnetic field is reversed. On the other hand, when the magnetic field is along the trigonal axis the contributions cancel, as we observed in  $(00.1)$  films grown on CdTe(111) substrates.

While the electrical and thermal conductivities of Bi and BiSb are reduced by a magnetic field, the magnitude of the Seebeck coefficient increases. As a result, the

effective thermoelectric figure of merit  $Z$  can increase in a field.<sup>18</sup> Our results confirm that for in-plane Bi and BiSb on-chip cooling applications, oblique films grown with their (00.1) tilted from the substrate normal are more favorable than (00.1) films.

### A.8 Bi/CdTe Superlattices

In order to grow Bi-based superlattices we tried several barriers as summarized in Table 1. Among them the Bi/CdTe system is a good combination from the viewpoint of growth mode properties. Our Te-interface-mediated-growth was then used in the growth of Bi/CdTe SLs. Bi/CdTe SL growth was initiated with a Bi layer on the CdTe(111)B buffer layer, resulting in layer-by-layer growth. However, based on the results of RHEED patterns and wet-etching experiments on Bi/CdTe, it has been reported that CdTe growth on Bi starts with a Te layer and ends with Cd.<sup>3</sup> The next Bi layer then exhibits 3D island growth during the first 50 Å of growth. In Fig. 51(a), a schematic of the Bi/CdTe SL structure with terminating atomic species is shown. The polarity inversion of the first CdTe layer and subsequent CdTe layers on Bi is evident in this schematic. In Fig. 51(b) a schematic of the structure of a Bi/CdTe SL with a Te ML between each Cd-terminated face of CdTe and the subsequent Bi layer is shown. In order to verify the role of the Te ML, two different 30 Å Bi /100 Å CdTe SLs, with and without the Te ML, were grown. A thickness of 30 Å Bi was chosen since previous results showed that 3D island growth of Bi becomes layer-by-layer on Cd-terminated faces after 50 Å.

Table 1. The summarized growth modes for various combinations.

<i>top layer/embedded layer</i>	<i>Growth Mode</i>
Bi/CdTe(111)A	3D island <50 Å <layer-by-layer
Bi/CdTe(111)B	Layer-by-layer
CdTe(111)A/Bi, Sb	Layer-by-layer
Bi/PbTe(111)	Layer-by-layer
PbTe(111)/Bi	3D island
$\alpha$ -Sn/CdTe	3D island <50 Å <layer-by-layer
PbTe/CdTe	3D island
CdTe/PbTe	Layer-by-layer

The X-ray diffraction (XRD) patterns of 50 period 30 Å Bi/100 Å CdTe SL's with and without the Te ML are shown in Fig. 52. It should be noted that without the Te ML the streaky RHEED patterns disappeared after several periods, implying that the SL does not grow layer-by-layer. The absence of SL satellites in the XRD scans is indicative of mixed layers. However, the introduction of a Te ML results in smooth Bi/CdTe SL's as shown in Fig. 52. In addition to SL harmonics a strong CdTe (111) Bragg peak from the substrate was observed. Four orders of satellite reflections can be seen, attesting to the

quality of the structure. These results imply that the introduction of Te may allow growth of SLs with very small Bi well thicknesses.

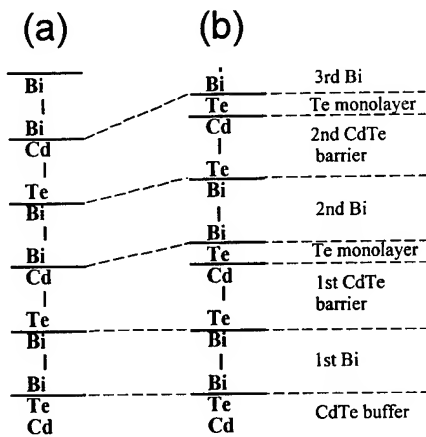


FIG. 51. (a) Bi/CdTe SL structure and (b) the suggested SL structure with Te ML.

Figure 53 shows cross-sectional TEM images of the 30 Å Bi/100 Å CdTe SLs with and without the Te ML deposition. Without the Te ML it is difficult to discern the interface after several periods. The growth of large grains along with severe intermixing is observed. However, for the Te atomic layer epitaxy case, a sharp interface was observed over many periods, in agreement with the XRD results. There was no evidence that 3D islands were present when Te MLs were incorporated.

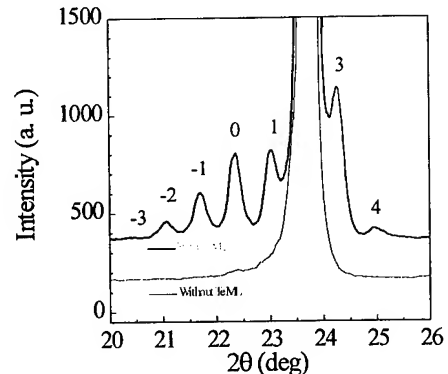


FIG. 52. X-ray diffraction pattern of 50 periods of 30 Å Bi/100 Å CdTe SLs with and without Te ML.

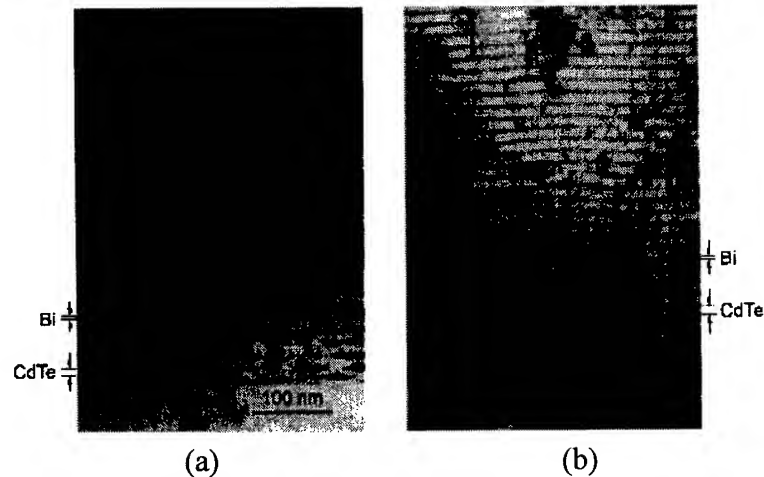


FIG. 53. TEM pictures of 50 periods of 30 Å Bi/100 Å CdTe SLs (a) without Te ML and (b) with Te ML.

$\text{\AA}/100 \text{\AA}$ )<sub>5</sub> superlattices are  $57.7 \mu\text{V/K}$  and  $56.8 \mu\text{V/K}$ , respectively, compared to the bulk value (perpendicular to the trigonal axis) of  $51.4 \mu\text{V/K}$ . As the Bi well thickness decreases, the TEP decreases. However, while the  $100 \text{\AA}$  single well showed p-type behavior for the entire temperature range  $20\text{--}300 \text{ K}$ , superlattices with Bi-layer thicknesses of  $80 \text{\AA}$  and  $100 \text{\AA}$  were p-type only at the lowest temperatures.

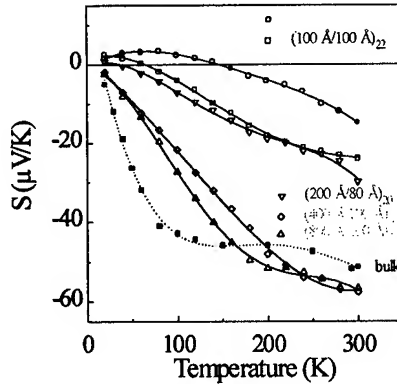


FIG. 54. TEPs of Bi/CdTe superlattices as a function of temperature. The subscript represents the number of Bi layers and the numbers in the parenthesis represent the Bi and CdTe barrier thicknesses, respectively. Bulk Bi single crystal (perpendicular to the trigonal axis) values were denoted by  $\square$  for comparison.

The modest enhancement of the TEP at temperatures above  $200 \text{ K}$  in the two thickest-well superlattice samples over both the  $10,000 \text{\AA}$  film data and previous results for bulk Bi may in fact reflect the effects of quantum confinement. It should be first pointed out that while the enhancement is small, it is nonetheless larger than the measurement errors in the present experiment, since the TEP determinations do not require any knowledge of active-layer thickness or other quantities that are not precisely calibrated. This quantum confinement may produce a small decrease of the semimetallic overlap between the electron and hole bands, which would decrease the thermally-generated intrinsic densities and increase the TEP at a given temperature as long as the p-type doping is not too great. However, the electrical conductivity ( $\sigma$ ) results were approximately a factor of two below the bulk Bi value of  $9100 (\Omega\text{-cm})^{-1}$  at  $300 \text{ K}$ :  $4800 (\Omega\text{-cm})^{-1}$  for  $(800 \text{\AA}/100 \text{\AA})_5$  and  $3400 (\Omega\text{-cm})^{-1}$  for  $(400 \text{\AA}/100 \text{\AA})_9$  at  $300 \text{ K}$ . As the Bi well thickness decreased, the electrical conductivity decreased. The calculated  $S^2\sigma$  at  $300 \text{ K}$  was  $1.46 \times 10^{-5} \text{ W/cm\cdot K}^2$  for  $(800 \text{\AA}/100 \text{\AA})_5$  and  $1.23 \times 10^{-5} \text{ W/cm\cdot K}^2$  for  $(400 \text{\AA}/100 \text{\AA})_9$ , which compares to about  $2.41 \times 10^{-5} \text{ W/cm\cdot K}^2$  in bulk Bi (perpendicular to the trigonal axis). In spite of the slight enhancement of TEP, the decreased  $S^2\sigma$  mainly comes from reduced carrier mobilities due to scattering at the CdTe interfaces (typically in the order of  $10^2 \text{ cm}^2/\text{V\cdot s}$  for the superlattices). For the thermoelectric cooling device application of Bi superlattices, one needs to improve the carrier mobility to increase the electrical conductivity and also prevent the unintentional p-type doping to optimize the TEP.

## B. Bi/Sb Superlattice Alloys (SLA)

### B.1. Structural Properties of Bi/Sb Superlattices

Bi/Sb superlattices were grown on semi-insulating CdTe(111)B substrates in the custom-built molecular beam epitaxy (MBE) system described earlier. A 3000 Å CdTe buffer layer was deposited on the CdTe substrate at 250 °C, followed by deposition of the Bi and Sb layers at a rate of about 0.4 Å/s and at a growth temperature of 100 °C. Growth was initiated with Bi on CdTe, followed by Sb and repeated to form a superlattice. The observed growth direction of the Bi and Sb layers on CdTe(111)B is parallel to the trigonal axis. RHEED was used to examine the specific surface reconstruction of the deposited layers. The in-plane lattice constants of Bi and Sb in the hexagonal representation are 4.546 and 4.308 Å, respectively. Consequently, the lattice mismatch of Bi and Sb with CdTe(111)B (4.58 Å) is 0.7 % and 6%, respectively.

The CdTe(111)B (Te-terminated) surface was used as a substrate for the growth of Bi/Sb superlattices because Bi grows in a layer-by-layer mode on CdTe(111)B, as opposed to a 3-dimensional (3D) island mode on CdTe(111)A.<sup>3,34</sup> 3D nucleation is regarded as undesirable because it may introduce height variations and a number of defects where the 3D islands coalesce. This is particularly undesirable for various planar devices such as quantum wells and superlattices which require uniform thickness and low defect densities (as well as sharp interfaces). The first Bi layer on CdTe shows a streaky RHEED pattern with Kikuchi lines, representing a smooth surface or 2D layer-by-layer growth and high crystallinity. The RHEED patterns of Bi(Sb) on Sb(Bi) also show streaks, representing the layer-by-layer growth of Bi on Sb or Sb on Bi with a good epitaxial quality. It should be noted that there are no surface reconstructions of Bi on Sb or Sb on Bi.

Figure 55 shows a typical  $\theta$ - $2\theta$  XRD pattern from various superlattices with periods of 20Å, 100Å, and 200Å. The scan consists of the CdTe(111) Bragg peak from the substrate surrounded by the Bi/Sb superlattice harmonics. A pattern of asymmetric satellite peaks is observed. Beside the zero-order superlattice reflection, the first-, second-, and third-order reflections can be seen, attesting to the high quality of the structure. As the modulation period increased, a large number of more closely spaced satellite peaks was observed. For the 200Å multilayer, the intensity of the central peak decreased and the satellite peaks near the Bi and Sb peak positions became stronger ( $2\theta = 22.49^\circ$  for Bi;  $2\theta = 23.69^\circ$  for Sb). The calculated modulation periods,  $\lambda$ 's, are consistent with the values determined by the quartz crystal balance. (See Table 2.) In addition, we could determine the full width at half maximum (FWHM) from the rocking curve. (See Table 2.) The 1<sup>st</sup> and 0<sup>th</sup> order superlattice peaks have the same FWHM, which indicates that there is no significant fluctuation with respect to the superlattice period.<sup>74</sup> The FWHM of a (10Å/10Å)<sub>300</sub> superlattice (300 periods of 10Å Bi and 10Å Sb) was 0.704°, indicating sharp superlattice interfaces and low dislocation density. The reason for the relatively high FWHM for the large modulation wavelengths can be attributed to strain relaxation in the thick layers and a smaller number of periods.

The microstructure of the superlattices was examined by cross-sectional TEM studies. A 30 period 100Å Bi/100Å Sb superlattice was prepared for TEM studies using standard methods. Since both the superlattice film and the substrate are relatively soft, care must be taken during mechanical thinning and Ar ion milling. High-resolution electron microscopy images were obtained with a *Hitachi-HF2000* electron microscope

operated at 200 kV. Figure 56(a) shows a low magnification electron micrograph of a Bi/Sb superlattice on CdTe(111)B as viewed from the (1̄10) crystal direction of the substrate. The Bi layers appear darker than the Sb layers due to the higher atomic number of Bi: the Bi atoms scatter electrons more strongly than Sb. A well-defined Bi/Sb superlattice was observed over many periods, in agreement with the XRD results. However, it is hard to discern the interfaces due to the atomic similarities. From the micrograph, the Bi/Sb superlattice has a modulation period of about 200 Å, which is consistent with the thickness calculated from the quartz crystal monitor and XRD patterns discussed above. Figures 56(b)-(d) show high-resolution lattice images of a Bi/Sb superlattice, the interface between Bi and the CdTe buffer, and the CdTe buffer layer, respectively. A sharp interface was observed between the 1<sup>st</sup> Bi layer and the CdTe. (Fig. 56(c)) Even though there is 5.2 % lattice mismatch between Bi and Sb, no interfacial misfit dislocations were observed in the HRTEM images of Bi and Sb layers over an area of 0.1 μm<sup>2</sup>. (Fig. 56(b)) It is concluded that the interfaces between the superlattice film and the CdTe substrate and between Bi and Sb layers are sharp, flat, and relatively dislocation free, representing layer-by-layer growth of Bi on CdTe and Bi on Sb (or Sb on Bi), as implied in the RHEED experiments. It should be noted that twin boundaries were observed in the CdTe(111) buffer layer. (See Fig. 56(a) and (d).) The stacking order changes as twin boundaries are passed so that the structures on both side of twin boundary are mirror images of each other. Although the stacking sequence may change with twin boundaries, they all stack along (111) direction.

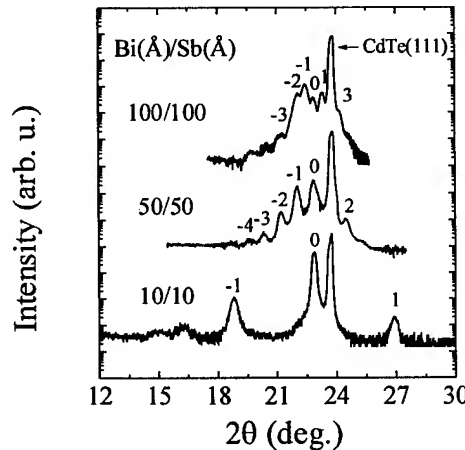


Fig. 55.  $\theta$ - $2\theta$  XRD pattern of Bi/Sb superlattices with three different modulation periods of 20 Å, 100 Å, and 200 Å. The CdTe(111) Bragg peak and Bi/Sb superlattice satellite reflections are shown in the plot.

Table 2. Summary of specimen characteristics;  $\lambda$  and  $\lambda_{XRD}$  are the modulation periods determined by the quartz crystal balance and XRD, respectively.

No.	Bi(Å)	Sb(Å)	$\lambda$ (Å)	No. of Periods	$\lambda_{XRD}$ (Å)	FWHM (°)	
						-1	0
1	10	10	20	300	22	0.7	0.7
2	50	50	100	60	110	2.0	1.9
3	100	100	200	30	207	1.9	1.8



Fig. 56. Cross-sectional TEM images of a Bi/Sb superlattice consisting (30 layers of 100 Å Bi/100 Å Sb) on CdTe(111)B: (a) low magnification electron micrograph of Bi/Sb superlattice on CdTe(111)B as viewed from (1 $\bar{1}$ 0) projection; (b) high-resolution lattice image of Bi/Sb superlattice (arrows represent interface between Bi and Sb); (c) vicinity of the 1<sup>st</sup> Bi layer and the CdTe(111)B buffer (arrow represents interface) and; (d) CdTe(111)B buffer layer (arrow represents twin boundaries in the CdTe(111) buffer).

### B.2. Thermal Conductivity of Bi/Sb Superlattices

The thermal conductivity of a 50 Å/50 Å Bi/Sb superlattice was measured using the 3- $\omega$  method in collaboration with Prof. G. Chen's group at UCLA. A detailed description will be found elsewhere.<sup>75</sup> A 1- $\mu$ m thick Bi/Sb superlattice film consisting of alternating layers of 50 Å Bi and 50 Å Sb was grown by molecular beam epitaxy on a CdTe(111)B substrate. On the top of the Bi/Sb superlattice film, an 800 Å layer of ZnTe was deposited, also by MBE, to electrically insulate the Bi/Sb superlattice. However, the ZnTe film appeared to be too conductive for the required measurements. Therefore, to achieve electrical insulation, an additional 1100 Å layer of Si<sub>x</sub>N<sub>y</sub> was deposited on the ZnTe surface by plasma-enhanced chemical vapor deposition. A 10  $\mu$ m wide, 2 mm long heater was then deposited and patterned on the Si<sub>x</sub>N<sub>y</sub> surface by the conventional microfabrication technology. In addition to this "superlattice" sample, a "reference" sample was also fabricated, which consisted of the same collection of films as the former except for the Bi/Sb superlattice layer. The films common to the "superlattice" and

“reference” samples were deposited in the same steps to ensure identical deposition conditions.

To measure the cross-plane thermal conductivity of the Bi/Sb superlattice, the differential 3- $\omega$  technique was used, which uses the measured temperature differences between the sample and the reference to obtain the thermal conductivity of the film. The temperature rise of the heater is deduced from the third harmonic of the voltage drop across the heater which is driven by a sinusoidal current at the angular frequency  $\omega$ . The resistance of a metal heater depends linearly on temperature and the current variation at the frequency  $\omega$  causes a  $2\omega$  modulation in the temperature. These two effects combine to produce a voltage at  $3\omega$  that is proportional to the temperature rise. The measurements were done at temperatures from 80 K to 300 K inside a cryostat using liquid nitrogen flow. Both the “superlattice” sample and the “reference” sample were measured. The thermal conductivity of the CdTe substrate was obtained by using Cahill’s “slope method”.<sup>76</sup>

In a typical differential 3- $\omega$  measurement, the cross-plane thermal conductivity of a thin film,  $k_F$ , of thickness  $d_F$  on a substrate is calculated using a simple one-dimensional approximation from Fourier’s Law:

$$k_F = qd_F / (T_F - T_{REF}), \quad (10)$$

where  $q$  is the cross-plane heat flux at the metal wire, and  $T_F$  and  $T_{REF}$  are the temperature rise amplitude of the wires on the “thin film” sample and on the “reference” sample, respectively. This approximation, however, is valid only when two conditions are satisfied: (1) The film thermal conductivity must be much smaller than the substrate thermal conductivity, and (2) the heater width is much larger than the film thickness. The CdTe substrate has a very low lattice thermal conductivity, especially at higher temperatures. The literature values for the thermal conductivity of bulk single-crystal CdTe, ranging from 7.6 W/mK at 150 K to 3.5 at 300 K, are lower than those of bulk Bi and bulk Sb.<sup>77</sup> Therefore the thermal conductivity of the CdTe substrate is comparable to or lower than that of the Bi/Sb superlattice film, and Eq. (10) can no longer be used for data analysis. Indeed, the experimental temperature rise of the sample and the reference at 280 K, as shown in Fig. 57, are very close to each other. Therefore, a new strategy has been developed for analyzing the experimental data.<sup>78</sup> Beginning with the two-dimensional heat conduction solution for a film with an anisotropic thermal conductivity on a substrate, the temperature difference between the film and the substrate can be expressed as

$$\Delta T = T_F - T_S = \frac{qd_F}{k_F} CF, \quad (11)$$

where  $C$  is a constant that compensates for the contrast between the in-plane and cross-plane film thermal conductivities,  $k_{F,x}$  and  $k_{F,y}$ , and the substrate thermal conductivity,  $k_S$ :

$$C = \left( 1 - \frac{k_{F,x} k_{F,y}}{k_S^2} \right). \quad (12)$$

The constant  $F$  in Eq. (11) compensates for the effect of lateral heat spreading in the film:

$$F = \frac{2}{\pi} \int_0^\infty \frac{\sin^2 x}{x^3} \frac{\tanh(x)}{1 + (k_{F,y}/k_s) \tanh(x)} dx. \quad (13)$$

From the modified approximation in Eq. (11),  $k_{F,y}$ , the cross-plane thermal conductivity of a thin film on a substrate can be calculated for any given value of cross-plane temperature drop in the thin film, even vanishingly small or negative.

Using these approximations, the frequency-dependent temperature rise has been simulated to fit the experimental data for the "superlattice" and the "reference" samples. The lines in Fig. 57 show the calculated temperature rise for the "superlattice" and the "reference" samples at 80 K and 280 K. While the fit is very accurate for the "reference" sample, the simulated result slightly underpredicts the experimental temperature rise for the "superlattice" sample. This may be because Eq. (11) describes the case where there is only one film on a substrate, so that it works better for the two-film "reference" sample than for the three-film "superlattice" sample.

The experimental cross-plane thermal conductivity of the Bi/Sb superlattice as a function of temperature is plotted in Fig. 58. Clearly, the thermal conductivity of the superlattice is not only *much smaller* than that of the bulk 50 % Bi / 50 % Sb multilayer calculated using the published values of the two bulk elements,<sup>77</sup> but is also much smaller than the published value for bulk Bi<sub>0.5</sub>Sb<sub>0.5</sub> alloy,<sup>77</sup> by a factor of 2.

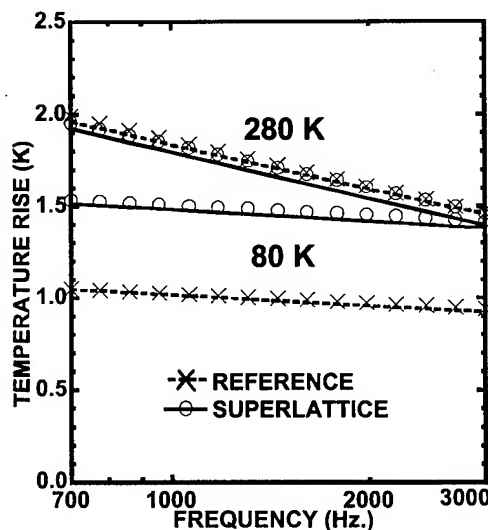


Fig. 57. Fitted temperature rise for the "superlattice" sample at 80 K and 280 K and for the "reference" sample at 80 K. The lines are simulated results, and the o and x are the experimental data.

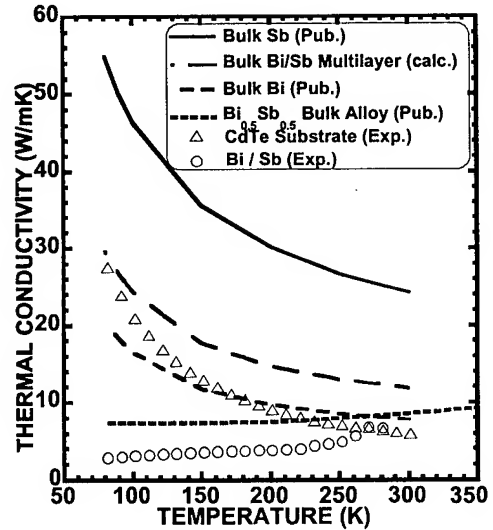


Fig. 58. Experimental thermal conductivity of a Bi/Sb superlattice and the CdTe substrate. Shown also are the published values for bulk Bi, bulk Sb, and bulk Bi<sub>0.5</sub>Sb<sub>0.5</sub> alloy,<sup>77</sup> and the calculated value for a 50 % Bi / 50 % Sb multilayer assuming the bulk values.

### B.3. Structural Properties of Bi/Sb SLA

Transport in a semimetal/semimetal Bi/Sb superlattice with a long period might be modeled as parallel transport in the two semimetals. On the other hand, when the superlattice modulation period approaches atomic spacings, we would expect to see random alloy characteristics. Between these limits, the electronic properties of the superlattice should show intermediate behavior at the least. When combined with the conductivity reduction (arising from an increase in phonon scattering from the superlattice interfaces), the short period superlattice may show more desirable thermoelectric properties.

In this section, the structural and transport properties of Bi/Sb superlattices with very short (down to sub unit cell) modulation periods are described. The average Sb composition has been maintained in the 0.09-0.17 range. The signature of superlattice formation (artificial ordering in the growth direction), x-ray superlattice satellites, has been observed even when the individual layers are less than one monolayer thick. Transport measurements to be described show that the electronic band structure can be engineered from a semimetal to a semiconductor by changing the modulation period of the superlattices.

The crystal structure of Bi or Sb and the atomic arrangements of both a random alloy and an atomic-scale ordered superlattice are shown in Fig. 59. Along the trigonal growth axis, there are six planes making up the 11.86 Å (Bi) or 11.274 Å (Sb) unit cell, which corresponds to about 2 Å for each plane. MBE has been used to form atomic scale ordered  $\text{Bi}_m\text{Sb}_n$  superlattice structures consisting of  $m$  planes of Bi alternating with  $n$  planes of Sb along the trigonal axis, where  $m$  and  $n$  are not necessarily integers.

The Bi/Sb superlattices with the modulation period from 55 Å to 7.7 Å were grown on semi-insulating CdTe(111)B ( $E_g = 1.5$  eV) substrates. A two-second interruption time was introduced between the deposition of Bi and Sb layers to enhance surface migration of the absorbed atoms during the growth. Eight Bi/Sb superlattices samples with different modulation periods were prepared; 7.7 Å (7 Å Bi/0.7 Å Sb), 11 (10/1), 12 (10/2), 16.5 (15/1.5), 18 (15/3), 27 (24/3), 40 (35/5), and 55 (48/7). Each superlattice had a total thickness of 1.2 μm.

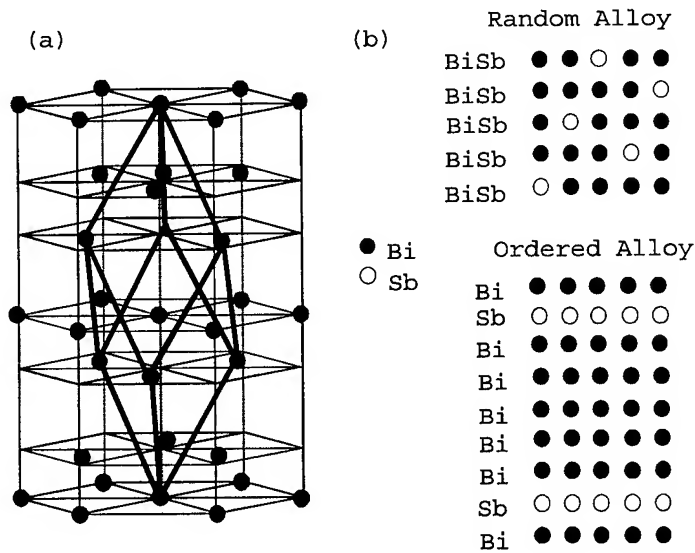


Fig. 59. (a) The crystal structure of rhombohedral Bi or Sb. (b) The schematic atomic arrangement of a random alloy and an artificially ordered alloy. Whereas the Sb atoms are randomly positioned in the random alloy, they are confined to specific planes in the ordered alloy.

In growing superlattices with sharp interfaces, two-dimensional (2D) nucleation is preferred over 3D nucleation, since the latter may introduce height variations and other defects where the 3D islands coalesce. The *in-situ* RHEED experiments showed a streaky pattern with Kikuchi lines for the Bi layer grown on CdTe(111)B, and also for the growth of Bi(Sb) on Sb(Bi), regardless of the Bi and Sb layer thicknesses. These observations confirm 2D layer-by-layer growth for both Bi on Sb and Sb on Bi. The RHEED patterns repeat every 60-degrees, implying growth along the trigonal axis.

In order to verify the presence of ordering in the growth direction, we performed standard  $\theta$ -2 $\theta$  x-ray diffraction studies for various superlattices. Well-resolved patterns involving satellite peaks are observed, as shown in Fig. 60. Besides the fundamental Bragg diffraction peak, the first-, second-, third-, and fourth-order SL reflections can be seen for larger modulation periods, indicating relatively abrupt interfaces between the layers. As the modulation period decreases, the angular separation between the satellites increases. Remarkably, we see distinct satellites in superlattices with monolayer and even submonolayer Sb layers: (10 Å Bi/1 Å Sb), (10/2), and (15/1.5). While some atomic interdiffusion is clearly unavoidable, the observation of superlattice satellites for structures containing monolayer and submonolayer Sb layers confirms the formation of an ordered structure with well-defined layers. Clearly, the growth temperature of only 100 °C helps to minimize the interlayer mixing.<sup>6</sup> The angular position of the x-ray satellite peaks yields a superlattice modulation period that is consistent with the value determined by the quartz crystal thickness monitor.

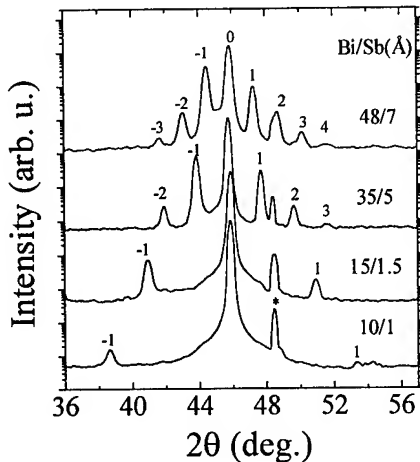


Fig. 60.  $\theta$ - $2\theta$  X-ray scans around the (00.4) reflection for ordered Bi/Sb superlattice alloys with different modulation periods. (\*: substrate CdTe(222) peak.)

#### B.4. Thermoelectric and Transport Properties of SLA

Figure 61 shows the temperature-dependent electrical resistivities for all of the Bi/Sb superlattices prepared. The samples with a long period show semimetallic behavior, as expected. However, as the modulation period decreases, the electrical resistivity rapidly increases at low temperatures. This indicates that a semimetal-semiconductor transition occurs as the modulation period decreases. We have determined an effective thermal gap ( $E_g$ ) for the semiconducting alloys using the relation  $\rho = \rho_0 \exp(E_g / 2k_B T)$ , in order to qualitatively interpret our results and compare them with the values reported for random alloys. The effective thermal energy gaps derived in this manner were 29, 29, 25, 24, and 22 meV for the samples with modulation periods of 7.7, 11, 12, 16.5, and 18 Å, respectively. Note that the thermal energy gaps of the superlattices decrease with modulation period, and are smaller than the 35-40 meV values<sup>34</sup> of random alloy films, which were also grown on CdTe(111)B, with the same average composition.

Similar qualitative behavior is observed in the temperature-dependent thermopower data shown in Fig. 62. All samples exhibit negative thermopowers because they are either *n*-type or intrinsic, and the electrons have higher mobilities than the holes (see below). The ordered alloys with 7.7, 11, 12, 16.5, and 18 Å modulation periods show a slight thermopower increase above 200 K, which is characteristic of an intrinsic semiconductor.<sup>34</sup> The magnitude of the negative thermopower increases with decreasing period, which also indicates an enhanced semiconducting energy gap. Other samples with longer modulation periods show semimetallic behavior, which is consistent with the electrical resistivity data. These resistivity and thermopower results provide strong evidence that the electronic structure of a short modulation period Bi/Sb superlattice is comparable to but differs from that of a random alloy film with the same average composition. Furthermore, the electronic structure can be tuned via the modulation period from semimetallic, through zero-gap, to narrow bandgap semiconducting.

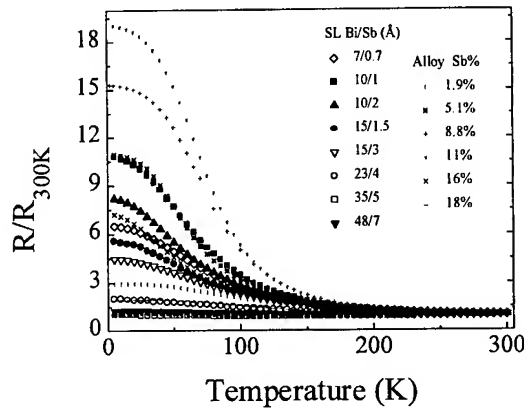


Fig. 61. Temperature dependent electrical resistivities of ordered superlattice alloys.

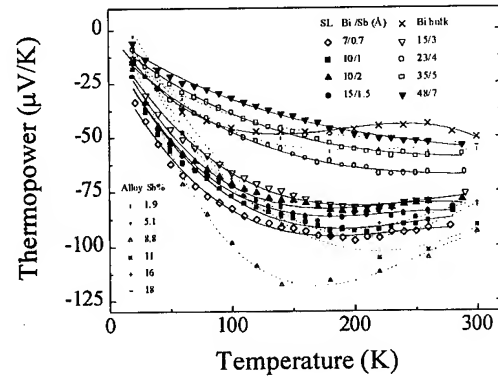


Fig. 62. Thermopower vs. temperature for the ordered superlattice alloys and bulk Bi.

To investigate this phenomenon in greater detail, magnetic-field-dependent Hall and resistivity measurements were carried out on all samples at  $B$ -fields from 0 to 7 Tesla and at 19 different temperatures between 4.2 and 300 K. Quantitative Mobility Spectrum Analysis (QMSA)<sup>32,79,80</sup> was then used to determine the densities and mobilities for both electrons and holes at each temperature. The results are illustrated in Fig. 63 and Table 3 along with earlier data<sup>32</sup> for Bi and  $\text{Bi}_{0.91}\text{Sb}_{0.09}$  films with similar thicknesses. All of the superlattices had similar low-temperature electron mobilities ranging from 7800-19000  $\text{cm}^2/\text{Vs}$ , which are only slightly lower than the corresponding values for Bi and  $\text{Bi}_{0.91}\text{Sb}_{0.09}$ . At 300 K, where phonon scattering dominates, all of the mobilities were nearly identical. Low-temperature hole mobilities were generally in the 2000-5000  $\text{cm}^2/\text{Vs}$  range.

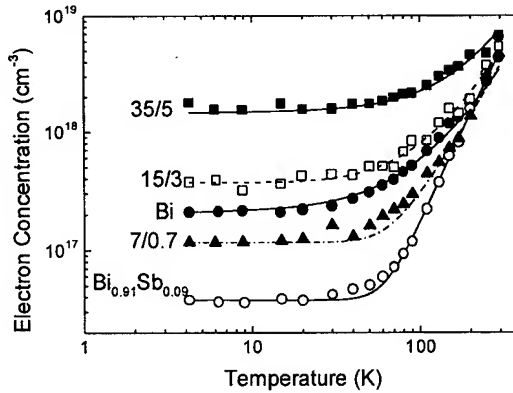


Fig. 63. Temperature-dependent electron concentrations (points) and statistical fits (curves), as determined by a QMSA of field-dependent magneto-transport measurements.

In the low-temperature limit, all of the superlattice samples are either  $n$ -type or intrinsic ( $n \approx p$ ), with electron concentrations in the  $1.1 \times 10^{17}$  to  $1.8 \times 10^{18} \text{ cm}^{-3}$  range. Figure 62 shows that the carrier densities increase with temperature, as additional carriers

are generated thermally. The curves represent fits to a statistical model,<sup>32</sup> which accounts for the anisotropy, nonparabolicity, valley degeneracy, and temperature dependence of the various conduction and valence bands. The net donor concentration was fixed by the experimental values for  $n_0-p_0$  in the low-temperature limit, and the bandgap (either positive or negative) was used as a fitting parameter. The same empirical density-of-states (DOS) effective mass gave good fits to the high-temperature electron densities in all of the superlattice samples, although slightly different DOS masses were employed for Bi and  $\text{Bi}_{0.91}\text{Sb}_{0.09}$ .

Table 3 Selected electronic characteristics derived with the QMSA from the field-dependent magneto-transport measurements. Results are given for Bi, a  $\text{Bi}_{1-x}\text{Sb}_x$  random alloy, and several superlattices;  $n_0$  and  $p_0$  are the low-temperature ( $\leq 15$  K) concentrations of electrons and holes, respectively, and  $\mu_n$  is the low-temperature electron mobility. All samples were either *n*-type or nominally intrinsic.

$L_{\text{Bi}}$ (Å)	$L_{\text{Sb}}$ (Å)	$x_{\text{av}}$	$E_g$ (meV)	$n_0$ (cm <sup>-3</sup> )	$\mu_n$ (cm <sup>2</sup> /Vs)	$p_0$ (cm <sup>-3</sup> )
$\text{Bi}_{0.91}\text{Sb}_{0.09}$		0.09	35	$3.8 \times 10^{16}$	$2.6 \times 10^4$	$\ll n_0$
7	0.7	0.09	5	$1.2 \times 10^{17}$	$1.9 \times 10^4$	$\ll n_0$
10	1	0.09	0	$1.1 \times 10^{17}$	$1.9 \times 10^4$	$\ll n_0$
15	1.5	0.09	-10	$2.2 \times 10^{17}$	$1.9 \times 10^4$	$7.0 \times 10^{16}$
15	3	0.17	-15	$3.7 \times 10^{17}$	$9.7 \times 10^3$	$\ll n_0$
10	2	0.17	-20	$3.8 \times 10^{17}$	$7.8 \times 10^3$	$\ll n_0$
Bi		0	-25	$2.1 \times 10^{17}$	$6.0 \times 10^4$	$\approx n_0$
23	4	0.15	-50	$1.3 \times 10^{18}$	$1.6 \times 10^4$	$\approx n_0$
35	5	0.13	-50	$1.8 \times 10^{18}$	$1.8 \times 10^4$	$\approx n_0$
48	7	0.13	-50	$1.5 \times 10^{18}$	$1.4 \times 10^4$	$\approx n_0$

The bandgaps derived in this manner are listed in Table 3. Because the masses and their temperature dependences are complex and not known precisely (with the possible role of H-valley holes in the superlattices being especially uncertain), and also because the data become less sensitive to the magnitude of the bandgap when it is very small and the nonparabolicity is strong, the accuracy is limited. For example, we obtain -25 meV for the bandgap of Bi, whereas more detailed experimental characterizations generally yield a value closer to -38 meV.<sup>79</sup> However, we expect the relative trends of our derived bandgaps to be meaningful.

Those trends show an unmistakable dependence of the electronic structure on the modulation period of the superlattices. It is apparent from Table 3 that all of the samples with thicker Sb layers (23/4, 35/5, 48/7) have much larger band overlaps than pure Bi. However, decreasing the period at fixed average Sb concentration leads to a progressively smaller overlap and ultimately to a gap. This confirms that the superlattices have a distinct band structure which systematically depends on layer thickness, rather than reverting to the properties of the equivalent random alloy as would

occur if interdiffusion were severe. We are not aware of any simple Kronig-Penny model which will explain these results. Likely supercell band structure calculations are required.

In summary, by alternating thin layers of Bi and Sb in a periodic geometry, atomic scale ordered Bi/Sb superlattices have fabricated. X-ray data have confirmed that even structures with sub-monolayer Sb thicknesses exhibit clear periodicity. By changing the modulation period thickness, the electronic structure was tuned from a semimetal, through zero-gap, to a narrow-gap semiconductor. While long-period samples showed semimetallic behavior, a semimetal-semiconductor transition was observed at short periods. In treating the differences in the geometric and electronic structure between atomic scale ordered superlattices and random alloys of similar average composition, the atomic scale ordered superlattices should be viewed as a new way of engineering material characteristics.

## V. Conclusions

We have grown Bi and BiSb alloy thin films and superlattices on CdTe(111)B over wide range of Sb composition using MBE. The structural properties may be summarized as follows:

1. Bi and Bi-rich BiSb alloy thin films grow in layer-by-layer mode on CdTe(111)B.
2. The crystallinity of BiSb thin films becomes poorer with increasing Sb concentration and improves with epilayer thickness.
3. The out-of-plane lattice constant is consistently smaller than that of the bulk due to the lattice mismatch. This strain may affect the band structure of BiSb alloy thin films grown on CdTe(111)B substrates.
4. The surface of BiSb films is rougher relative to Bi films.
5. By introducing a Te ML on the CdTe(111)A (Cd-terminated) face of Bi/CdTe SLs, the growth mode of Bi was changed from 3D island to layer-by-layer growth. This result, while similar to the use of surface floating surfactants in its ability to improve the growth, is different in that the Te ML remains at the Bi/CdTe(111)A interface.

We have studied the transport properties of MBE-grown-1 $\mu$ m-thick Bi<sub>1-x</sub>Sb<sub>x</sub> alloy thin films on CdTe(111)B over a wide range of Sb concentrations (0<x<0.183). Compared to the bulk alloy system, there are three important conclusions. i) Semiconducting behavior was observed for the 3.5 and 5.1% Sb alloy thin films. ii) The Sb concentration for the maximum TEP and thermal bandgap shifts toward lower Sb concentrations, from 15 % to 9 %. iii) The effective thermal bandgap and TEPs of the alloy thin films grown on CdTe(111) are larger than for bulk alloys. The differences between thin film grown on CdTe(111) and the bulk alloys may be due to strain modifying the electronic band structure. In addition, we have observed that the power factor S<sup>2</sup>/ρ peaks at a significantly higher temperature (250K) relative to that for the bulk alloy, which peaks at (80K). The dependence of the electronic structure on the Bi lattice parameters provides a means of controlling the electronic structure and thermoelectric properties of Bi and BiSb films by strains imposed by film/substrate lattice mismatch. These results suggest that band-engineered Bi-based materials may be useful in thermoelectric devices.

From thermoelectric power measurements on MBE grown Bi thin films and Bi/CdTe superlattices, we observe that the TEP in (400 Å/100 Å)<sub>9</sub> and (800 Å/100 Å)<sub>5</sub> superlattices is enhanced slightly at high temperatures compared to Bi bulk single crystal values. However as the Bi well thickness in the superlattices decreases, the magnitude of the TEP decreases due to unintentional p-type doping, which leads to compensation of the electron contribution and a positive sign for the TEP under some conditions. Thus, by reducing the excess hole concentration in the superlattices we may further increase the TEP value. One option would be to purposely introduce n-type impurities into the CdTe barrier layer so as to modulation dope the Bi, thereby allowing a test of the Gallo *et al.* conjecture. Reduced carrier mobility resulted in low  $S^2\sigma$  values. Consequently, we were unable to confirm the prediction of Hicks *et al.*, but the results are encouraging. All this suggests that practical applications of Bi-based superlattices for thermoelectric cooling devices might indeed be possible.

We have successfully grown Bi/Sb superlattices with different superlattice periods down to sub-monolayer Sb thicknesses on CdTe(111)B substrates using MBE. The structural properties have been investigated using *in-situ* RHEED, XRD and HRTEM. Bi (Sb) grew on Sb (Bi) layer-by-layer epitaxially, as confirmed by the streaked RHEED patterns with clear Kikuchi lines. The superlattices had very sharp interfaces and the superlattice periods did not fluctuate, as verified by the narrow rocking curves for the central and the satellite peaks. No interfacial misfit dislocations were observed in the cross-sectional HRTEM images of the Bi and Sb layers over an area of 0.1  $\mu\text{m}^2$ . Even structures with sub-monolayer Sb thicknesses exhibited clear periodicity, confirmed by the existence of the XRD satellite peaks.

In collaboration with a group at the University of California at Los Angeles, the cross-plane temperature thermal conductivity of a 1  $\mu\text{m}$  thick 50 Å Bi / 50 Å Sb superlattice on CdTe was measured. The thermal conductivity of the superlattice film was a factor 2 lower than the literature value for the Bi<sub>0.5</sub>Sb<sub>0.5</sub> bulk alloy, which we interpret as arising from an increase in phonon scattering from the superlattice interfaces. The electronic structure of superlattices with almost the same average composition could be modified by changing the superlattice period (from several unit cells to sub-unit cell length scales). While long-period samples showed semimetallic behavior, a semimetal-semiconductor transition was observed at short periods. This may open another way to modifying electronic and thermal transport properties such as thermal conductivity and energy band gap by changing the geometric structure. Such structures may have more desirable thermoelectric properties, accompanied by reduced thermal conductivity.

We have performed systematic doping experiments on semiconducting Bi<sub>0.91</sub>Sb<sub>0.09</sub> alloy thin films using the group VI(IV) element Te(Sn) as an donor(acceptor). We have demonstrated that BiSb alloy thin films can be doped with Sn(Te) to densities exceeding  $5 \times 10^{20} \text{ cm}^{-3}$  for n-type and  $1 \times 10^{21} \text{ cm}^{-3}$  for p-type. The thermoelectric power, electrical resistivity, and Hall effect were studied in the range of temperatures 5~300 K. Doping Sn into the BiSb system causes the TEP to change sign (from negative to positive) and the maximum in the TEP can be controlled with the dopant concentration. Increased doping

with either Sn or Te causes the TEP to decrease. Highly Sn and Te-doped samples show degenerate characteristics in the electrical resistivity, TEP and Hall measurement. We observed that the Fermi level of  $\text{Bi}_{0.91}\text{Sb}_{0.09}$  thin films is raised (lowered) with Te (Sn) doping. The Fermi levels for highly doped samples were 0.67 eV and -0.54 eV for Te and Sn doped cases, respectively.

The magnetotransport results were analyzed using a Quantitative Mobility Spectrum Analysis (QMSA) procedure, which derives carrier densities and mobilities for all of the species present. A number of important improvements were recently incorporated into QMSA, which now offers a better overall extraction of information from experimental data sets than any previous technique.

The anisotropy of Bi and BiSb alloy films was studied in order to evaluate their performance as in-plane cooling devices. Rhombohedral Bi and BiSb films were grown on (211)CdTe by MBE. XRD studies showed that Bi films on (211)CdTe grow along the CdTe (111) direction ([00.1] axes, tilted by 19° from the substrate normal). In Seebeck and magneto-Seebeck coefficient measurements in magnetic fields up to  $\pm 0.7$  T, we observed a strong in-plane anisotropy in the Seebeck coefficients due to the anisotropic electronic structure, with values along the direction not perpendicular (with an angle of 71°) to the trigonal axis being higher than those perpendicular to the trigonal axis. We also observed that magneto-Seebeck coefficients for the films grown along the tilted axis are larger than when there is no tilt and the crystal axis is aligned with the magnetic field. These experiments suggest that films grown with the (00.1) axis tilted from the substrate normal show better in-plane thermoelectric properties than the more typical (00.1) films.

In order to obtain high quality Bi films, post annealing just below the melting point of Bi was performed. A 10  $\mu\text{m}$  Bi film grown on CdTe by MBE and subsequently annealed showed a large magnetoresistance ratio, 2700 at 5 K and 5 T, compared with 340 for the unannealed sample. An annealed 10  $\mu\text{m}$  Bi film on mica showed a much larger value of 12000 at 5 K and 5 T. This implies that a post annealing process may be one way to improve the quality of films when the highest possible deposition temperature for epitaxial growth is not compatible with the best transport properties. The large magnetoresistance ratio of annealed bismuth films can be ascribed to a higher mobility relative to that in unannealed samples.

## VI. References

1. S. C. Shin, J. E. Hilliard, and J. B. Ketterson, *J. Vac. Sci. Technol. A* **2**, 296 (1984).
2. S. C. Shin, J. E. Hilliard, and J. B. Ketterson, *Phys. Rev. B* **30**, 4099 (1984).
3. A. DiVenere, X. J. Yi, C. L. Hou, H. C. Wang, J. B. Ketterson, G. K. Wong, and I. K. Sou, *Appl. Phys. Lett.* **62**, 2640 (1993).
4. A. DiVenere, X. J. Yi, C. L. Hou, H. C. Wang, J. Chen, J. B. Ketterson, G. K. Wong, J. R. Meyer, C. A. Hoffman, and F. J. Bartoli, *J. Vac. Sci. Technol. B* **12**, 1136 (1994).
5. C. A. Hoffman, J. R. Meyer, F. J. Bartoli, A. DiVenere, X. J. Yi, C. L. Hou, H. C. Wang, J. B. Ketterson, and G. K. Wong, *Phys. Rev. B* **48**, 1143 (1993); *Phys. Rev. B* **51**, 5535 (1995).
6. X. J. Yi, H. C. Wang, A. DiVenere, C. L. Hou, J. Chen, J. B. Ketterson, and G. K. Wong, *Appl. Phys. Lett.* **64**, 1283 (1994).
7. C. F. Gallo, B. S. Chandrasekhar, and P. H. Sutter, *J. Appl. Phys.* **34**, 144 (1963).
8. L. D. Hicks and M. S. Dresselhaus, *Phys. Rev. B* **47**, 12 727 (1993).
9. L. D. Hicks, T. C. Harman, and M. S. Dresselhaus, *Appl. Phys. Lett.* **63**, 3230 (1993).
10. J. O. Sofo and G. D. Mahan, *Appl. Phys. Lett.* **65**, 2690 (1994).
11. G. D. Mahan and H. B. Lyon, Jr., *J. Appl. Phys.* **76**, 1899 (1994).
12. D. A. Broido and T. L. Reinecke, *Phys. Rev. B* **51**, 13 797 (1995).
13. D. A. Broido and T. L. Reinecke, *Appl. Phys. Lett.* **67**, 100 (1995).
14. P. J. Lin-Chung, and T. L. Reinecke, *Phys. Rev. B* **51**, 13 244 (1995).
15. A. L. Jain, *Phys. Rev.* **114**, 1518 (1959).
16. S. Golin, *Phys. Rev.* **176**, 830 (1968).
17. G. Oelgart, G. Schneider, W. Kraak and R. Herrmann, *Phys. Stat. Sol. (b)* **74**, K75 (1976).
18. W. M. Yim and A. Amith, *Solid-State Electron.* **15**, 1141 (1972).
19. B. Lenoir, M. Cassart, J.-P. Michenaud, H. Scherrer and S. Scherrer, *J. Phys. Chem. Solids* **57**, 89 (1996).
20. D. M. Brown and S. J. Silverman, *Phys. Rev.* **136**, A290 (1964).
21. V. G. Alekseeva, N. F. Zaets, A. A. Kudryashov, and A. B. Ormont, *Sov. Phys. Semicond.* **10**, 1332 (1976).
22. N. B. Brandt and E. A. Svistova, *J. Low Temp. Phys.* **2**, 1 (1970).
23. N. B. Brandt and Ya. G. Ponomarev, *Sov. Phys. JETP* **28**, 635 (1969).
24. N. B. Brandt, S. M. Chudinov, and V. G. Karavaev, *Sov. Phys. JETP* **34**, 368 (1972).
25. N. B. Brandt, Kh. Dittmann and Ya. G. Ponomarev, *Sov. Phys. Solid State* **13**, 2408 (1972).
26. E. E. Mendez, A. Misu, and M. S. Dresselhaus, *Phys. Rev. B* **24**, 639 (1981).
27. M. Lu, R. J. Zieve, A. van Hulst, H. M. Jaeger, T. F. Rosenbaum, and S. Radelaar, *Phys. Rev. B* **53**, 1609 (1996).
28. D. T. Morelli, D. L. Partin and J. Heremans, *Semicon. Sci. Technol.* **5**, S257 (1990).
29. D. M. Brown and S. J. Silverman, *Phys. Rev.* **136**, A290 (1964).

30. J. Antoszewski, D. J. Seymour, L. Faraone, J. R. Meyer, and C. A. Hoffman, *J. Electron. Mater.* **24**, 1255 (1995).

31. J. R. Meyer, C. A. Hoffman, J. Antoszewski, and L. Faraone, *J. Appl. Phys.* **81**, 709 (1997).

32. I. Vurgaftman, J. R. Meyer, C. A. Hoffman, D. Redfern, J. Antoszewski, L. Faraone, and J. R. Lindemuth, *J. Appl. Phys.* **84**, 4966 (1998).

33. S. Cho, A. DiVenere, G. K. Wong, J. B. Ketterson, J. R. Meyer, and C. A. Hoffman, *Proc. of Int. Conf. Thermoelectrics*, Dresden, Germany, p188 (1997).

34. S. Cho, A. DiVenere, G. K. Wong, J. B. Ketterson, J. R. Meyer, and J. I. Hong, *Phys. Rev. B* **59**, 10691 (1999).

35. S. Cho, A. DiVenere, G. K. Wong, J. B. Ketterson, J. R. Meyer, and C. A. Hoffman, *J. Vac. Sci. Technol. A* **17**, 9 (1999).

36. J. A. Venables, G. D. T. Spiller, and M. Hanbucken, *Rep. Prog. Phys.* **47**, 399 (1984).

37. C. H. Choi, R. Ai, and S. A. Barnett, *Phys. Rev. Lett.* **67**, 2826 (1991).

38. G. Wannier, *Phys. Rev.* **52**, 191 (1937).

39. W. S. Boyle and A. D. Brailsford, *Phys. Rev.* **120**, 1943 (1960).

40. G. Busch and H. Schade, "Lectures on Solid State Physics", p290-379, Pergamon Press, New York (1976).

41. I. Ya. Korenblit, M. E. Kusnetsov, and S. S. Shalyt, *Soviet Phys. JETP*, **29**, 4 (1969).

42. B. Shick, A. J. Freeman, and J. B. Ketterson, *Bull. Amer. Phys. Soc.* **43**, 171 (1998).

43. B. S. Chandrasekhar, *J. Phys. Chem. Solids*, **11**, 268 (1959).

44. L. W. Tu, G. K. Wong, and J. B. Ketterson, *Appl. Phys. Lett.* **54**, 1010 (1989).

45. B. Abeles and S. Meiboom, *Phys. Rev.* **101**, 544 (1956).

46. J.-P. Michenaud and J.-P. Issi, *J. Phys. C* **5**, 3061 (1972); I. F. I. Mikhail, O. P. Hansen, and H. Nielsen, *J. Phys. C* **13**, 1697 (1980).

47. T. Yazaki and Y. Abe, *J. Phys. Soc. Japan* **24**, 290 (1968).

48. Yu. I. Ravich and A. V. Rapoport, *Sov. Phys. Solid State* **34**, 960 (1992) [Fiz. Tverd. Tela **34**, 1801 (1992)].

49. J. P. Omaggio, J. R. Meyer, C. A. Hoffman, A. DiVenere, X. J. Yi, C. L. Hou, H. C. Wang, J. B. Ketterson, G. K. Wong, and J. P. Heremans, *Phys. Rev. B* **48**, 11439 (1993).

50. S.Y. Savrasov, *Phys. Rev. B* **54**, 16470 (1996).

51. S. Golin, *Phys. Rev.* **166**, 643 (1968).

52. X. Gonze, J.-P. Michenaud, J.-P. Vigneron, *Phys. Rev. B* **41**, 11827 (1990).

53. Y. Liu and R. Allen, *Phys. Rev. B* **52**, 1566 (1995).

54. G. Jozequel et al., *Phys. Rev. B* **56**, 6620 (1997).

55. K. J. Chang and M. L. Cohen, *Phys. Rev. B* **33**, 7371 (1986).

56. P. Cucka and C. S. Barrett, *Acta Cryst.* **16**, 461 (1962).

57. J. M. Noothoven Van Goor, *Phillips Res. Repts Suppl.* No. 4, 1 (1971).

58. J. Heremans, D. T. Morelli, D. L. Partin, C. H. Olk, C. M. Thrush, and T. A. Perry, *Phys. Rev. B* **38**, 10 280 (1988).

59. P. Jandl and U. Birkholz, *J. Appl. Phys.* **76**, 7351 (1994).

60. C. B. Thomas and H. J. Goldsmid, *J. Phys. C: Solid St. Phys.* **3**, 696 (1970).

61. F. Y. Yang, K. Liu, C. L. Chien, and P. C. Searson, *Phys. Rev. Lett.* **82**, 3328 (1999).
62. F. Y. Yang, K. Liu, K. Hong, D. H. Reich, P. C. Searson, and C. L. Chien, *Science* **284**, 1335 (1999).
63. J. H. Mangez, J. P. Issi, and J. Heremans, *Phys. Rev. B* **14**, 4381 (1976).
64. J. S. Dhillon and D. Shoenberg, *Philos. Trans. R. Soc. London* **248**, 1 (1955).
65. B. Y. Jin, H. K. Wong, G. K. Wong, J. E. Hilliard, J. B. Ketterson, and Y. Eckstein, *Thin Solid Films* **110**, 29 (1983).
66. S. C. Shin, J. E. Hilliard, and J. B. Ketterson, *J. Vac. Sci. Technol. A* **2**, 296 (1984).
67. S. A. Solin, T. Thio, D. R. Hines, J. J. Heremans, *Science* **289**, 1530 (2000).
68. D. L. Partin, J. Heremans, D. T. Morelli, C. M. Thrush, C. H. Olk, and T. A. Perry, *Phys. Rev. B* **38**, 3818 (1988).
69. S. Cho, Y. Kim, A. DiVenere, G. K. L. Wong, J. B. Ketterson, and J. R. Meyer, *Appl. Phys. Lett.* **75**, 1401 (1999).
70. W. M. Huber, S. T. Li, A. Ritzer, D. Bauerle, H. Lengfellner, and W. Prettl, *Appl. Phys. A* **64**, 487 (1997).
71. I. Ya. Korenblit, M. E. Kusnetsov, and S. S. Shalyt, *Soviet Phys. JETP*, **29**, 4 (1969).
72. H. J. Goldsmid, *phys. stat. sol. (a)* **1**, 7 (1970).
73. G. E. Smith and R. Wolfe, *J. Phys. Soc. Japan* **21**, Suppl., 651 (1966).
74. A. Segmuller and A. E. Blakeslee, *J. Appl. Cryst.* **6**, 19 (1973).
75. D. W. Song, G. Chen, S. Cho, Y. Kim, J. B. Ketterson, *Mat. Res. Soc. Symp. Proc.* **626**, Z9.1 (2000).
76. D. G. Cahill, *Rev. Sci. Instrum.*, **61**, 802 (1990).
77. Y. S. Touloukian, "Thermophysical Properties of Matter", IFI/Plenum, New York, NY (1979).
78. G. Chen, S. Q. Zhou, D.-Y. Yao, C. J. Kim, X. Y. Zheng, Z. L. Liu, and K. L. Wang, *Proc. 17<sup>th</sup> Int. Conf. Thermoelectrics*, 1 (1998).
79. I. Vurgaftman, J. R. Meyer, C. A. Hoffman, S. Cho, A. DiVenere, G. K. Wong, and J. B. Ketterson, *Phys: Condens. Matter* **11**, 5157 (1999).
80. I. Vurgaftman, J. R. Meyer, C. A. Hoffman, S. Cho, J. B. Ketterson, L. Faraone, J. Antoszewski and J. R. Lindemuth, *J. Electron. Mat.* **28**, 548 (1999).

## VII. List of Publications

### 1. Journal Articles Submitted or Published

1. "Growth mode modification of Bi on CdTe(111)A using Te monolayer deposition", S. Cho, A. DiVenere, G. K. Wong, J. B. Ketterson, J. R. Meyer and J. I. Hong, Phys. Rev. B **54**, 2324 (1998).
2. "Molecular beam epitaxial growth and structural properties of BiSb alloy thin films on CdTe(111) substrates", S. Cho, A. DiVenere, G. K. Wong, J. B. Ketterson, J. R. Meyer, and C. A. Hoffman, J. Vac. Sci. Technol. A **17**, 9 (1999).
3. "Thermoelectric transport properties of n-doped and p-doped  $\text{Bi}_{0.91}\text{Sb}_{0.09}$  alloy thin films", S. Cho, A. DiVenere, G. K. Wong, J. B. Ketterson, and J. R. Meyer, J. Appl. Phys. **85**, 3655 (1999).
4. "Transport properties of Bi and  $\text{Bi}_{1-x}\text{Sb}_x$  alloy thin films grown on CdTe(111)B", S. Cho, A. DiVenere, G. K. Wong, J. B. Ketterson, and J. R. Meyer, Phys. Rev. B **59**, 10691 (1999).
5. "Quantitative mobility spectrum analysis (QMSA) for Hall characterization of electrons and holes in anisotropic bands", I. Vurgaftman, J. R. Meyer, C. A. Hoffman, S. Cho, J. B. Ketterson, L. Faraone, J. Antoszewski, and J. R. Lindemuth, J. Electron. Mater. **28**, 548-552 (1999).
6. "Thermoelectric and magnetotransport properties of  $\text{Bi}_{1-x}\text{Sb}_x$  thin films and Bi/CdTe superlattices", I. Vurgaftman, J. R. Meyer, C. A. Hoffman, S. Cho, A. DiVenere, G. K. Wong, J. B. Ketterson, J. Phys. - Condens. Mat. **11**, 5157-5167 (1999).
7. "Antisite defects of  $\text{Bi}_2\text{Te}_3$  thin films", S. Cho, Y. Kim, A. DiVenere, G. K. Wong, and J. B. Ketterson, Appl. Phys. Lett. **75**, 1401-1403 (1999).
8. "Bi/Sb superlattices grown by molecular beam epitaxy", S. Cho, Y. Kim, A. DiVenere, G. K. Wong, J. B. Ketterson, J.-I. Hong, J. Vac. Sci. Technol. A **17**, 2987 (1999).
9. "Growth habit of rhombohedral Bi thin films on zinc-blende CdTe substrates with various orientations", Y. Kim, S. Cho, A. DiVenere, G. K. Wong, and J. B. Ketterson, J. Vac. Sci. Technol. A **17**, 3473 (1999).
10. "Electronic structure, phase stability, and semimetal-semiconductor transitions in Bi", A. B. Shick, J. B. Ketterson, D. L. Novikov, and A. J. Freeman, Phys. Rev. B **60**, 15484 (1999).
11. "Anisotropic Seebeck and magneto-Seebeck coefficients in Bi and BiSb alloy thin films", S. Cho, Y. Kim, A. DiVenere, G. K. L. Wong, J. B. Ketterson, and J. R. Meyer, J. Appl. Phys. **88**, 808 (2000).

12. "Composition-dependent layered structure and transport properties in BiTe thin films", Y. Kim, S. Cho, A. DiVenere, G. K. L. Wong, and J. B. Ketterson, Phys. Rev. B. **63**, 155306 (2001).
13. "First-principles electronic structure and its relation to thermoelectric properties of  $\text{Bi}_2\text{Te}_3$ ", S. J. Youn, and A. J. Freeman, Phys. Rev. B. **63**, 085112 (2001).
14. "Large magnetoresistance in post-annealed Bi thin films", by S. Cho, Y. Kim, A. J. Freeman, G. K. Wong, J. B. Ketterson, L. J. Olafsen, I. Vurgaftman, J. R. Meyer, and C. A. Hoffman, submitted to Applied Physics Letters. (4/4/2001)
15. "Bi epitaxy on polar InSb(111)A/B faces", by S. Cho, Y.-H. Um, Y. Kim, G. K. Wong, J. B. Ketterson, and J.-I. Hong, submitted to Journal of Vacuum Science & Technology A. (4/4/2001)
16. "Artificially ordered Bi/Sb superlattice alloys: fabrication and transport properties", by S. Cho, Y. Kim, S. J. Youn, A. DiVenere, G. K. Wong, A. J. Freeman, J. B. Ketterson, L. J. Olafsen, I. Vurgaftman, J. R. Meyer, and C. A. Hoffman, submitted to Physical Review B. (4/4/2001)
17. "Polarity inversion in polar/nonpolar/polar heterostructures", by S. Cho, S.-J. Youn, Y. Kim, A. DiVenere, G. K. L. Wong, A. J. Freeman, and J. B. Ketterson, submitted to Physical Review Letters. (4/4/2001)
18. "Structural and thermoelectric transport properties of  $\text{Sb}_2\text{Te}_3$  thin films grown by molecular beam epitaxy", by Y. Kim, A. DiVenere, G. K. L. Wong, J. B. Ketterson, S. Cho, J. R. Meyer, submitted to Journal of Applied Physics. (5/7/2001)

## 2. Conference Proceedings

1. "Thermoelectric power of Bi and  $\text{Bi}_{1-x}\text{Sb}_x$  alloy thin films and superlattices grown by MBE", S. Cho, A. DiVenere, G. K. Wong, J. B. Ketterson, J. R. Meyer, and C. A. Hoffman, Mat. Res. Soc. Symp. Proc. **478**, 67 (1997).
2. "Observation of a power factor enhancement in MBE-grown  $\text{Bi}_{1-x}\text{Sb}_x$  alloy thin films", S. Cho, A. DiVenere, G. K. Wong, J. B. Ketterson, J. R. Meyer, and C. A. Hoffman, Proc. of Int. Conf. Thermoelectrics, Dresden, Germany, p188 (1997).
3. "Structural and thermoelectric properties of MBE-grown doped and undoped BiSb alloy thin films", S. Cho, A. DiVenere, G. K. Wong, J. B. Ketterson, J. R. Meyer, and C. A. Hoffman, Proc. of Int. Conf. Thermoelectrics, Nagoya, Japan, p284 (1998).
4. " $\text{Bi}_{1-x}\text{Sb}_x$  thin film and superlattice thermoelectrics", S. Cho, A. DiVenere, A. B. Shick, Y. Kim, S. J. Youn, A. J. Freeman, G. K. Wong, J. B. Ketterson, J. R. Meyer and C. A. Hoffman, MRS March Meeting, Boston, 1998. (Mat. Res. Soc. Symp. Proc. **545**, 283 (1999))

5. "MBE growth and thermoelectric properties of  $\text{Bi}_2\text{Te}_3$  thin films", S. Cho, A. DiVenere, G. K. Wong, J. B. Ketterson, and J. R. Meyer, MRS March Meeting, Boston, 1998. (Mat. Res. Soc. Symp. Proc. **545**, 183 (1999))
6. "Thermoelectric and structural properties of  $\text{Bi}_{1-x}\text{Te}_{1+x}$  thin films on  $\text{CdTe}(111)$ ", Y. Kim, S. Cho, A. DiVenere, G. K. Wong, J. B. Ketterson, and J. R. Meyer, MRS March Meeting, Boston, 1998. (Mat. Res. Soc. Symp. Proc. **545**, 177 (1999))
7. "Artificially Ordered BiSb Superlattice Alloy: Growth and Thermoelectric Properties", S. Cho, Y. Kim, A. DiVenere, G. K. Wong, J. B. Ketterson, J. R. Meyer, International Conference on Thermoelectrics, Baltimore, USA, Oct. 29-Sep. 2, 1999.
8. "Growth and Thermoelectric Properties of Artificially Layered  $(\text{BiSb})_2\text{Te}_3$ ", S. Cho, Y. Kim, A. DiVenere, G. K. Wong, J. B. Ketterson, J. R. Meyer, International Conference on Thermoelectrics, Baltimore, USA, Oct. 29-Sep. 2, 1999.
9. "Anisotropic Seebeck and Magneto-Seebeck Coefficients of Bi and BiSb Alloy Thin Films", S. Cho, Y. Kim, A. DiVenere, G. K. Wong, J. B. Ketterson, J. R. Meyer, International Conference on Thermoelectrics, Baltimore, USA, Oct. 29-Sep. 2, 1999.
10. "Control of Antisite Defect Effect of  $\text{Sb}_2\text{Te}_3$  Thin Films", Y. Kim, S. Cho, A. DiVenere, G. K. Wong, J. B. Ketterson, J. R. Meyer, International Conference on Thermoelectrics, Baltimore, USA, Oct. 29-Sep. 2, 1999.
11. "Bi Substitution Effects on  $\text{Sb}_2\text{Te}_3$  Thin Films", Y. Kim, S. Cho, A. DiVenere, G. K. Wong, J. B. Ketterson, J. R. Meyer, International Conference on Thermoelectrics, Baltimore, USA, Oct. 29-Sep. 2, 1999.
12. "Artificially Atomic-Scale Ordered Superlattice Alloys for Thermoelectric Applications", S. Cho, Y. Kim, A. DiVenere, G. K. L. Wong, A. J. Freeman, J. B. Ketterson, L. J. Olafsen, I. Vurgaftman, J. R. Meyer, C. A. Hoffman, G. Chen, MRS Spring Meeting, San Francisco, Apr. 24-27, 2000. (Mat. Res. Soc. Symp. Proc. **626**, Z2.4 (2000))
13. "Thermal Conductivity of Bi/Sb Superlattice", D. W. Song, G. Chen, S. Cho, Y. Kim, J. B. Ketterson, MRS Spring Meeting, San Francisco, Apr. 24-27, 2000. (Mat. Res. Soc. Symp. Proc. **626**, Z9.1 (2000))

### 3. Conference Presentations

1. "Bi and BiSb alloy thin films and superlattices for thermoelectric cooling devices", S. Cho, A. DiVenere, A. B. Shick, S. J. Youn, A. J. Freeman, G.K. Wong, J.B. Ketterson, J. R. Meyer and C.A. Hoffman, DARPA Kick-off Meeting, Pasadena, 1997.

2. "Observation of a power factor enhancement in MBE-grown  $\text{Bi}_{1-x}\text{Sb}_x$  alloy thin films", S. Cho, A. DiVenere, G. K. Wong, J. B. Ketterson, J. R. Meyer, and C. A. Hoffman, Int. Conf. Thermoelectrics, Dresden, Germany, 1997.
3. "Thermoelectric properties of doped BiSb alloy thin films", S. Cho, A. DiVenere, G. K. Wong, J. B. Ketterson, J. R. Meyer and C. A. Hoffman, APS March Meeting, Los Angeles, 1998.
4. "Electron structure and phase stability in Bi and Bi doped with Sb", A.B. Shick, D. L. Novikov, A. J. Freeman, and J. B. Ketterson, APS March Meeting, Los Angeles, 1998.
5. "Structural and thermoelectric properties of MBE-grown doped and undoped BiSb alloy thin films", S. Cho, A. DiVenere, Y. Kim, G. K. Wong, J. B. Ketterson, J. R. Meyer and C. A. Hoffman, International Conference on Thermoelectrics, Nagoya, Japan, May 24-28, 1998.
6. "Structural and thermoelectric properties of MBE-grown  $\text{Bi}_2\text{Te}_3$  thin films", S. Cho, A. DiVenere, Y. Kim, G. K. Wong, J. B. Ketterson, J. R. Meyer and C. A. Hoffman, Electronic Materials Conference, Charlottesville, Virginia, June 24-26, 1998.
7. " $\text{Bi}_{1-x}\text{Sb}_x$  thin film and superlattice thermoelectrics", J. B. Ketterson, S. Cho, A. DiVenere, A. B. Shick, Y. Kim, S. J. Youn, A. J. Freeman, G. K. Wong, J. B. Ketterson, J. R. Meyer and C. A. Hoffman, MRS Fall Meeting, Boston, 1998.
8. "MBE growth and thermoelectric properties of  $\text{Bi}_2\text{Te}_3$  thin films", S. Cho, A. DiVenere, G. K. Wong, J. B. Ketterson, and J. R. Meyer, MRS Fall Meeting, Boston, 1998.
9. "Thermoelectric and structural properties of  $\text{Bi}_{1-x}\text{Te}_{1+x}$  thin films on CdTe(111)", Y. Kim, S. Cho, A. DiVenere, G. K. Wong, J. B. Ketterson, and J. R. Meyer, MRS Fall Meeting, Boston, 1998.
10. "Polarity conversion in CdTe/Bi(Sb)/CdTe heterostructures", S. Cho, A. DiVenere, Y. Kim, G. K. Wong and J. B. Ketterson, APS March Meeting, Atlanta, 1999.
11. "Artificially layered  $(\text{BiSb})_2(\text{TeSe})_3$  thin films: growth and thermoelectric properties", S. Cho, Y. Kim, A. DiVenere, G. K. Wong and J. B. Ketterson, APS March Meeting, Atlanta, 1999.
12. "Artificially Ordered BiSb Superlattice Alloy: Growth and Thermoelectric Properties", S. Cho, Y. Kim, A. DiVenere, G. K. Wong, J. B. Ketterson, J. R. Meyer, International Conference on Thermoelectrics, Baltimore, USA, Oct. 29-Sep. 2, 1999.

2. "Observation of a power factor enhancement in MBE-grown  $\text{Bi}_{1-x}\text{Sb}_x$  alloy thin films", S. Cho, A. DiVenere, G. K. Wong, J. B. Ketterson, J. R. Meyer, and C. A. Hoffman, Int. Conf. Thermoelectrics, Dresden, Germany, 1997.
3. "Thermoelectric properties of doped BiSb alloy thin films", S. Cho, A. DiVenere, G. K. Wong, J. B. Ketterson, J. R. Meyer and C. A. Hoffman, APS March Meeting, Los Angeles, 1998.
4. "Electron structure and phase stability in Bi and Bi doped with Sb", A.B. Shick, D. L. Novikov, A. J. Freeman, and J. B. Ketterson, APS March Meeting, Los Angeles, 1998.
5. "Structural and thermoelectric properties of MBE-grown doped and undoped BiSb alloy thin films", S. Cho, A. DiVenere, Y. Kim, G. K. Wong, J. B. Ketterson, J. R. Meyer and C. A. Hoffman, International Conference on Thermoelectrics, Nagoya, Japan, May 24-28, 1998.
6. "Structural and thermoelectric properties of MBE-grown  $\text{Bi}_2\text{Te}_3$  thin films", S. Cho, A. DiVenere, Y. Kim, G. K. Wong, J. B. Ketterson, J. R. Meyer and C. A. Hoffman, Electronic Materials Conference, Charlottesville, Virginia, June 24-26, 1998.
7. " $\text{Bi}_{1-x}\text{Sb}_x$  thin film and superlattice thermoelectrics", J. B. Ketterson, S. Cho, A. DiVenere, A. B. Shick, Y. Kim, S. J. Youn, A. J. Freeman, G. K. Wong, J. B. Ketterson, J. R. Meyer and C. A. Hoffman, MRS Fall Meeting, Boston, 1998.
8. "MBE growth and thermoelectric properties of  $\text{Bi}_2\text{Te}_3$  thin films", S. Cho, A. DiVenere, G. K. Wong, J. B. Ketterson, and J. R. Meyer, MRS Fall Meeting, Boston, 1998.
9. "Thermoelectric and structural properties of  $\text{Bi}_{1-x}\text{Te}_{1+x}$  thin films on CdTe(111)", Y. Kim, S. Cho, A. DiVenere, G. K. Wong, J. B. Ketterson, and J. R. Meyer, MRS Fall Meeting, Boston, 1998.
10. "Polarity conversion in CdTe/Bi(Sb)/CdTe heterostructures", S. Cho, A. DiVenere, Y. Kim, G. K. Wong and J. B. Ketterson, APS March Meeting, Atlanta, 1999.
11. "Artificially layered  $(\text{BiSb})_2(\text{TeSe})_3$  thin films: growth and thermoelectric properties", S. Cho, Y. Kim, A. DiVenere, G. K. Wong and J. B. Ketterson, APS March Meeting, Atlanta, 1999.
12. "Artificially Ordered BiSb Superlattice Alloy: Growth and Thermoelectric Properties", S. Cho, Y. Kim, A. DiVenere, G. K. Wong, J. B. Ketterson, J. R. Meyer, International Conference on Thermoelectrics, Baltimore, USA, Oct. 29-Sep. 2, 1999.

13. "Growth and Thermoelectric Properties of Artificially Layered  $(\text{BiSb})_2\text{Te}_3$ ", S. Cho, Y. Kim, A. DiVenere, G. K. Wong, J. B. Ketterson, J. R. Meyer, International Conference on Thermoelectrics, Baltimore, USA, Oct. 29-Sep. 2, 1999.
14. "Anisotropic Seebeck and Magneto-Seebeck Coefficients of Bi and BiSb Alloy Thin Films", S. Cho, Y. Kim, A. DiVenere, G. K. Wong, J. B. Ketterson, J. R. Meyer, International Conference on Thermoelectrics, Baltimore, USA, Oct. 29-Sep. 2, 1999.
15. "Control of Antisite Defect Effect of  $\text{Sb}_2\text{Te}_3$  Thin Films", Y. Kim, S. Cho, A. DiVenere, G. K. Wong, J. B. Ketterson, J. R. Meyer, International Conference on Thermoelectrics, Baltimore, USA, Oct. 29-Sep. 2, 1999.
16. "Bi Substitution Effects on  $\text{Sb}_2\text{Te}_3$  Thin Films", Y. Kim, S. Cho, A. DiVenere, G. K. Wong, J. B. Ketterson, J. R. Meyer, International Conference on Thermoelectrics, Baltimore, USA, Oct. 29-Sep. 2, 1999.
17. "Large Magnetoresistance and High Mobilities in Annealed Bi Thin Films", Y. Kim, S. Cho, A. DiVenere, G. K. Wong, A. J. Freeman, J. B. Ketterson, D. W. Stokes, I. Vurgaftman, J. R. Meyer, C. A. Hoffman, APS March Meeting, Minneapolis, Mar. 20-24, 2000.
18. "Artificially Atomic-Scale Ordered Superlattice Alloys for Thermoelectric Applications", Y. Kim, S. Cho, A. DiVenere, G. K. L. Wong, A. J. Freeman, J. B. Ketterson, L. J. Olafsen, I. Vurgaftman, J. R. Meyer, C. A. Hoffman, G. Chen, MRS Spring Meeting, San Francisco, Apr. 24-27, 2000.
19. "A new magnetic semiconductor:  $(\text{Zn},\text{Mn})\text{GeAs}_2$  films", Y. Kim, B. Choi, S. Cho, A. DiVenere, G. K. Wong and J. B. Ketterson, APS March Meeting, Seattle, Mar. 12-16, 2001.

## **VIII. Scientific Personnel**

### **1. Northwestern University**

J. B. Ketterson

A. J. Freeman

G. K. Wong

A. DiVenere

S. Cho

Y. Kim

A. B. Shick

S. J. Youn

Dr. Sunglae Cho earned a Ph.D degree in Dec. 1997 during employed on this project with the thesis title "Molecular Beam Epitaxial Growth and Thermoelectric Transport Properties of Bismuth and Bimuth-Antimony Alloy Thin Films and Quantum Well Superlattices". (Advisor: John B. Ketterson)

Yunki Kim worked employed on this project and will soon earn a Ph.D degree (will graduate in 2001) with the thesis title "Growth and Thermoelectric Transport Properties of Bi-Based Thin Film and Multilayer Structures". (Advisor: John B. Ketterson)

### **2. Naval Research Laboratory**

J. R. Meyer

I. Vurgaftman

L. J. Olafsen

D. W. Stokes

C. A. Hoffman